ÇUKUROVA UNIVERSITY
INSTITUTE OF NATURAL AND APPLIED SCIENCES

Ph. D. THESIS

ALİ KAHRAMAN

INVESTIGATION OF FLOW STRUCTURE FROM A VERTICAL AND HORIZONTAL CYLINDER IN SHALLOW WATER

DEPARTMENT OF MECHANICAL ENGINEERING

ADANA, 2002

ÇUKUROVA ÜNİVERSİTESİ
FEN BİLİMLERİ ENSTİTÜSÜ

INVESTIGATION OF FLOW STRUCTURE FROM A VERTICAL AND HORIZONTAL CYLINDER IN SHALLOW WATER

ALİ KAHRAMAN

DOKTORA TEZİ

MAKİNA MÜHENDİSLİĞİ ANABİLİM DALI

Bu Tez 01./11./2002 Tarihinde Aşağıdaki Jüri Üyeleri Tarafından Oybirliği/~~Oyçokluğu~~ İle Kabul Edilmiştir.

İmza:
Prof. Dr. Beşir ŞAHİN
DANIŞMAN

İmza:
Prof. Dr. Ali ÜNÜVAR
ÜYE

İmza:
Doç. Dr. Şefik BİLİR
ÜYE

İmza:
Doç. Dr. Orhan BÜYÜKALACA
ÜYE

İmza:
Doç. Dr. Recep YURTAL
ÜYE

Bu Tez Enstitümüz Makina Mühendisliği Anabilim Dalında Hazırlanmıştır.

Kod No: 699

Prof. Dr. Fikri AKDENİZ
Enstitü Müdürü

Bu çalışma Çukurova Üniversitesi Bilimsel Araştırma Projeleri tarafından desteklenmiştir.

Proje No: FBE.2001.D45

ABSTRACT

Ph.D. THESIS

INVESTIGATION OF FLOW STRUCTURE FROM A VERTICAL AND HORIZONTAL CYLINDER IN SHALLOW WATER

ALİ KAHRAMAN

DEPARTMENT OF MECHANICAL ENGINEERING
INSTITUTE OF NATURAL AND APPLIED SCIENCES
UNIVERSITY OF ÇUKUROVA

Supervisor : Prof. Dr. Beşir ŞAHİN
Year: 2002, Pages: 144
Jury : Prof. Dr. Ali ÜNÜVAR
: Assoc. Prof. Dr. Şefik BİLİR
: Assoc. Prof. Dr. Orhan BÜYÜKALACA
: Assoc. Prof. Dr. Recep YURTAL

In this study, vortex structure in the wake region of the vertical and horizontal cylinders was investigated in shallow water layer using a technique of high-image-density Digital Particle Image Velocimetry (PIV). The formation of a large-scale Kármán vortex from a vertical cylinder involves upward ejection of fluid through its center which eventually turns into a horizontal vortex that induces significant distortion of the free-surface. Vortex formation from a vertical cylinder in shallow water layer is controlled by placement of narrow transverse strip of roughness elements on the bed (bottom surface). It is demonstrated that even the smallest roughness height clearly attenuates the onset of large-scale, Kármán-like vortex formation in the region close to the base of the cylinder, relative to the case of no roughness. In the second arrangement, the cylinder was submerged horizontally beneath the free-surface of the shallow water. The upper surface of the cylinder was adjusted in order to be coincident with the free-surface. The diameter of the horizontal cylinder was gradually increased in order to determine the values that exhibited major changes in the near-wake patterns. The streamline topology in the very near-wake of each cylinder is a strong function of the cylinder diameter and the Froude number.

Key Words: Wake region, Vortex formation, Shallow water flow, DPIV, Circular cylinder

ÖZ

DOKTORA TEZİ

SIĞ SUYA DİKEY VE YATAY OLARAK YERLEŞTİRİLMİŞ SİLİNDİR ARKASINDA OLUŞAN AYRILMIŞ AKIŞ YAPISININ İNCELENMESİ

ALİ KAHRAMAN

ÇUKUROVA ÜNİVERSİTESİ
FEN BİLİMLERİ ENSTİTÜSÜ
MAKİNA MÜHENDİSLİĞİ ANABİLİM DALI

Danışman : Prof. Dr. Beşir ŞAHİN
Year: 2002, Pages: 144
Jüri : Prof. Dr. Ali ÜNÜVAR
: Doç. Dr. Şefik BİLİR
: Doç. Dr. Orhan BÜYÜKALACA
: Doç. Dr. Recep YURTAL

Bu çalışmada, sığ suya dikey ve yatay olarak yerleştirilmiş silindir arkasında oluşan ayrılmış akış bölgesinin yapısı, Parçacık Görüntülemeli Hız Ölçüm Tekniği kullanılarak araştırılmıştır. Dikey silindir arkasında oluşan geniş ölçekli girdapları akış serbest yüzeye doğru yönlendirmekte ve nihayetinde bu girdaplar yatay girdaplara dönüşerek serbest yüzeyin düzgün yapısını bozmaktadır. Dikey silindir arkasında oluşan girdaplar, kanalın alt yüzeyine yatay olarak yerleştirilmiş farklı yüksekliklerdeki pürüz niteliğindeki engeller tarafından kontrol edilmiştir. En küçük yüksekliğe sahip olan engel dahi silindir arkasında oluşan geniş ölçekli Kármán girdabın şiddetini azaltmaktadır.Çalışmanın ikinci bölümünde, yatay olarak yerleştirilen ve çapları artırılan silindirlerin arkasında oluşan akışın yapısı incelenmiştir. Yatay olarak yerleştirilmiş silindirlerin çapı değiştirilerek ayrılmış akış bölgesinin değişimine olan etkileri gözlenmiştir.

Anahtar Kelimeler: Ayrılmış akış bölgesi, Girdap yapısı, Sığ sularda akış, Parçacık Görüntülemeli Hız Ölçme Tekniği, Silindir.

ACKNOWLEDGEMENTS

The list is endless if I have to thank all the people that made possible this work. My first and sincere thanks goes to my advisor Prof. Dr. Beşir ŞAHİN for his support, guidance and encouragement. He gave me possibility of going to USA and showed me what I thought nobody could really do: that there are no limits on what we can achieve. Thanks, from the bottom of my heart.

I am thankful to Prof Dr.-Ing Tuncay YILMAZ for his encouragement and for allowing me as the Head of the Department to carry out parts of this study at Lehigh University, USA.

I would like to extend my special thank to Prof. Dr. ROCKWELL for sharing his experience and contribution on behalf of Cukurova University for providing the laboratory facilities to do this work.

I am grateful to Assoc. Prof. Dr. Orhan BÜYÜKALACA, Assoc. Prof. Dr. Saadet BÜYÜKALACA and Asist. Prof. Dr. Hüseyin AKILLI for their continues moral support, motivation, friendship and encouragement me to go to USA. Knowing and feeling their support during my Ph.D helped me a lot to my self-confidence.

I must thank Dr. Muammer ÖZGÖREN and Dr. Hüsamettin BULUT for their supports, helps and friendship.

I also want to thank Assoc. Prof. Dr. Naki TÜTÜNCÜ and Asist. Prof. Dr. Ahmet PINARBAŞI for their constructive advice and moral support.

In addition, I would like to thank all the staff of Department of Mechanical Engineering at Cukurova University.

My sincere thanks go to my parent for their patience and trust. I am proud of being the brother of Şerife, İsa and Şeyma and the uncle of Kübranur, Büşranur and Hüzeyme.

At last, but not least, I would like to thank my wife, Fatma, and my new family for their moral support as well as their patience. Finally, I would like to thank my unique baby.

NOMENCLATURE

C_f : Bed (skin) friction coefficient

D : Diameter of cylinder (mm)

D_r : Diameter of roughness element (mm)

Fr : Froude number $\left(Fr = U/\sqrt{gh_w}\right)$

f : Frequency of Kármán vortex formation (Hz)

H : Height of water channel (mm)

h_L : Elevation of laser sheet

h_r : Height of roughness element (mm)

h_w : Height of water level (mm)

L : Distance between roughness element and base of cylinder

L_i : Length scale of the image (pixel)

L_r : Real physical length scale in flow field (mm)

K_z : Vertical eddy diffusion (m^2/sec)

M : Magnification factor ($M=L_i/L_r$)

N : Frame number

P : Island wake parameter $\left(P = \overline{U}h^2/K_zD\right)$

Re_d : Reynolds number based on the diameter of cylinder $\left(Re_d = UD/\nu\right)$

Re_h : Reynolds number based on the height of water level $\left(Re_d = Uh_w/\nu\right)$

Re_δ : Reynolds number based on the boundary layer thickness $\left(Re_d = U\delta/\nu\right)$

s : Space of center-to-center roughness element (mm)

S : Wake stability parameter $\left(S = C_fD/h_w\right)$

St : Strouhal number $\left(St = fD/\overline{U}\right)$

t : Time (sec)

T : Period of Kármán vortex formation (sec)

U : Free stream velocity (maximum velocity) (mm/sec)

$\overline{U}$: Depth-averaged velocity (mm/sec)

u,v : Component of velocity V in x and y axis system (mm/sec)

u_{rms} : Root-mean-square of u velocity component (mm^2/sec^2)

$u'v'$: Reynolds stress correlation (mm^2/sec^2)

u_* : Skin friction velocity (mm/sec)

V : Instantaneous total velocity vector (mm/sec)

$<V>$: Time-averaged total velocity vector (mm/sec)

v_{rms} : Root-mean-square of v velocity component (mm^2/sec^2)

W : Width of water channel (mm)

ω : Instantaneous vorticity (1/sec)

$<\omega>$: Time-averaged vorticity (1/sec)

ω_x : Streamwise vorticity (1/sec)

ω_y : Spanwise vorticity (1/sec)

ψ : Instantaneous streamline

$<\psi>$: Time-averaged streamline

δ : Boundary layer thickness (mm)

δ^* : Displacement thickness of boundary layer (mm)

θ : Momentum thickness of boundary layer (mm)

ν : Kinematic viscosity (mm/sec^2)

κ : von Karman constant (=0.41)

TABLE OF CONTENTS **PAGE**

LIST OF TABLES **PAGE**

LIST OF FIGURES **PAGE**

1. INTRODUCTION

Shallow water flows are defined as the situation where length scales of flow in the horizontal direction are much larger than the water depth (vertical scales). Shallow water flows are subjected of intensive investigations all over the world. Aerial photos of the wake from a grounded oil tanker, as well as the classical wake of an island provide a graphic description of the wake structure in shallow water. For example, the tanker Argo Merchant stranded on the Nantucket Shoals produced large eddies in the wake region which have a size of about 609.6 m, while the depth of at the same location is only about 15.24 m (Figure1.1, Van Dyke (1982)).

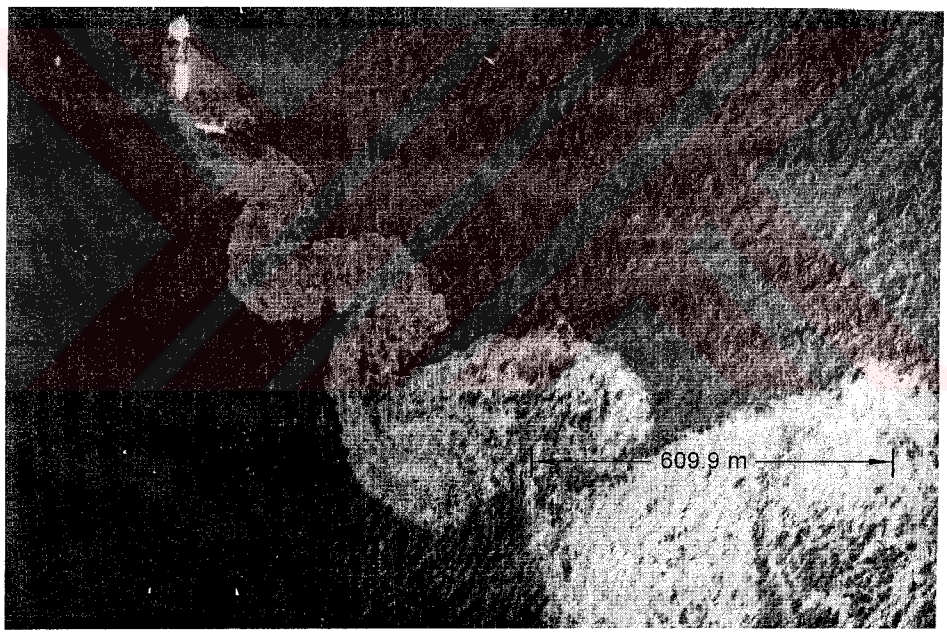

Figure 1.1. Aerial photograph of turbulent motion in wake of Stranded Tanker Argo Merchant on Nantucket Shoals (from an album of fluid motion, 1982).

The shallow water flows have two main characteristics. One of them is the presence of two boundaries in shallow water flow: a free surface and a bottom surface (bed). Both boundaries damp vertical motions and restrict the mean flow to nearly horizontal two-dimensional motion. Therefore, Tukker (1997) considered the shallow water flow as quasi-dimensional flows. Another characteristic of shallow water flows is that the turbulent boundary layer extends through the whole water depth.

The wake regions in shallow water occur in nature and a variety of engineering applications most notably at the merging of two rivers, behind a bridge pier and other types of hydraulic structures, in various types of channels, and at entrances to lakes and reservoirs. Wakes of islands are said to be shallow. Because, the horizontal length scales of the flows are two orders of magnitude larger than their depths. Babarutsi et al. (1989) gave an example for shallow water flows such that cross-stream diameters of the island are 280 m and 560 m, while the water depth in the region around the islands are only two to three meters. Despite their importance, relatively little is known of the detailed flow structure of shallow water vortices. They are important in producing erosion at the bottom surface (bed) of a river or channel, in mixing in a channel configuration.

A convenient way of disposing industrial and municipal wastes is to discharge them into the natural water bodies. But, the disposed wastes usually have a detrimental impact on both human an aquatic ecosystem. For example, the downstream water quality in a river would depend on the hydrodynamics of transport and mixing of the wastes. Similarly, an increase in the temperature of a river due to heated water discharge may decrease its assimilative capacities for oxygen demanding wastes like sewage effluents (Fischer et al., 1979). As a result, some of the past studies have been carried out to understand the characteristics of these environmentally important flow fields in detail. In many of the flows reported in literature, the primary focus has been on velocity measurements. Interestingly, many of the flow fields encountered in the environment can be classified as shallow.

Recent works, both experimental and computational have revealed some exciting new information about the nature of this flow including intricate three dimensional structures that emerge just prior to the onset of turbulence in the wake. It's a model for flow around bridges, buildings, and many other non-aerodynamic objects. Flow separation from obstacle walls results in strong shear layers, along which turbulence production terms are large. The high turbulence levels increase diffusion and enhance entrainment by the shear layer of low momentum reverse flow in the near-wake, which strongly affects the local pressure gradients and increases mixing. In the far wake, the streamwise vortices, such as the extensions of the

horseshoe vortex, cause rapidly changing spanwise gradients, which enhance heat, mass, and momentum transfer. Momentum in turbulent flows is regarded as a significant fundamental process in a wide variety of technological applications including heat and mass transfer, combustion optimization, and chemical processes.

A great many measurements have been carried out for the bluff body wake, including Strouhal number, coefficients of lift and drag, base pressure, separation points, surface shear stress, wake velocity measurements such as mean and fluctuating velocity profiles and Reynolds stresses and estimates of the length and width of the "vortex formation" region.

Vortices also occur in shallow water in a variety of engineering applications. They are important in producing erosion at the bed of a river or channel, in mixing of pollutants, and in inducing resonant motions of a free-surface in a channel configuration. Despite their importance, relatively little is known of the detailed flow structure of shallow water vortices.

Chen and Jirka (1995) reported that viscosity and hence the Reynolds number becomes the primary factor to control the flow pattern in bluff body wake flows. A kaleidoscope of flow patterns in deep water flow i.e. unbounded flow are categorized by Chen and Jirka (1995) over viewing the classification done by Morkovin (1964), Leinhard (1966) and Gerrard (1978): a regime of unseparated flow for $Re_d<5$; a fixed vortex pair in the wake for $5\text{-}15< Re_d<40$; and "incipient von Kármán range" for $40<Re_d<90$; the pure von Kármán vortex street range for $90<Re_d<150$; a transition range to turbulence in the wake for $150<Re_d<300$; and a fully turbulent wake for $Re_d>300$ (Reynolds number based on the diameter of the bluff body). In shallow water either vortex shedding or stable wake could be observed for wake Reynolds number values from 10^4 (in the experiments) to 10^7 (in nature).

In the event that the bluff body wake develops in shallow water, both the bottom friction and kinematical restriction in the vertical direction will dramatically change the wake behavior. The bottom friction generates small-scale, three-dimensional turbulent motions (limited by water depth), which act as an energy sink for the horizontal large-scale transverse motions through the existence of the bottom shear stress. The stabilizing influence of the bottom friction tends to suppress the

self-excited disturbances in the form of horizontal quasi two-dimensional vortex structures.

Bluff body wakes are complex in shallow water flow; for example, interactions of three shear layers occur at the same time. These are boundary layer, a separating free shear layer and wake. In this study, vortex structure in the wake region behind the vertical and horizontal cylinders was investigated in shallow water layer using a technique of high-image-density particle image velocimetry (PIV). Vortex formation from a vertical cylinder in shallow water layer was controlled by the placement of narrow transverse strip of roughness elements on the bed (bottom surface). Here, brief information is given about objective of the present work. The outline of the thesis will be presented in detail in Section 2.3.

2. LITERATURE SURVEY

2.1. Bluff Body Wakes in Deep Flow

One of the classical problems in fluid mechanics is the determination of the flow field around a bluff body. Vortex shedding from bluff bodies at moderate Reynolds numbers has been a topic of interest among fluid dynamics researchers for a long time. These interests stem from the underlying importance of flow separation in problems of engineering interest and the complex nature of the separation characteristics from a body of rather simple geometry. Careful experiments and theoretical developments in the last decade have yielded an excellent insight into the nature of the flow dynamics in the near wake of a bluff body.

Although the present work is aimed to look through the nature of wake flow around a circular cylinder in shallow water, it is also necessary and useful to go through a wake flow of a wide range of Reynolds number in deep flow in the literature. So that one can understand the nature of vortex characteristics in a large scale. A brief review of a selected papers related near wake region behind bluff body in deep flow are presented below.

The wake generator used in many of the earlier studies has been the circular cylinder placed normal to the flow. The last hundred years most of the researchers have investigated the flow structure behind a circular cylinder in deep water flows.

There are many important reviews in literature regarding structure of wake region downstream of the circular cylinder. For example, one of them is a recent review of Roshko (1993) which covers fundamental aspect of bluff body flows with a powerful theoretical discussion regarding the near wake recirculation region. Some of the previous work about the wake vortex dynamics were discussed in rather more detail in recent review of Williamson (1996).

A central feature of the quasi-two-dimensional structure of the near wake over the range of Reynolds number of interest in the literature are existence of two predominant length scales. The first corresponds to classical Kármán vortex formation from the cylinder and the second corresponds to the small-scale vortices in the separating shear layer having their origin in Kelvin-Helmholtz instability.

2.1.1. Kelvin-Helmholtz Vortices

At a sufficiently high value of Reynolds number, so-called "transition waves" appear in the shear layer separating from the surface of cylinder. These waves are detectable in the region of the wake extending from the separation point on the body to the first appearance of the large-scale Kármán vortex. When the value of Reynolds number is sufficiently high, then these transition waves take the form of train of Kelvin-Helmholtz vorties shown in Figure 2.1.1. In the bluff body community, these small-scale vortices are often referred to as Bloor-Gerrard vortices. The onset of "transition waves" is expected to be a strong function of the disturbance level of the free stream, in view of the fact that they arise from a convective-type instability, as described by Ho and Huerre (1984). Bloor (1964) detected the small-scale vorticies for the range of Reynolds number Re>1300, but, Ünal and Rockwell (1988) first noted these vorticies at Re_d=1900. Wu et al. (1994b) discussed the possible influence of background disturbance levels and observe these waves over the range of Reynolds numbers $1000 \leq Re \leq 3000$.

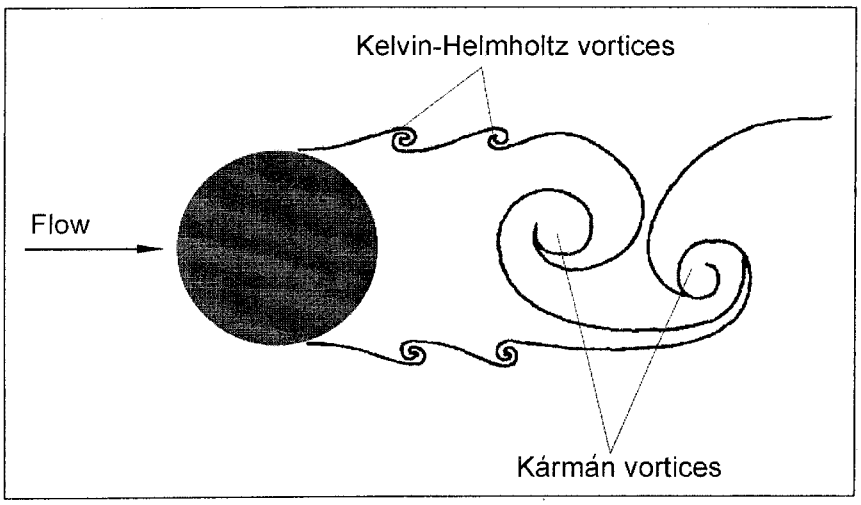

Figure 2.1.1. The Kelvin-Helmholtz (secondary) vortices and the Kármán vortices from circular cylinder.

Gerrard (1978) focused on the transition waves over the lower range of Reynolds numbers extending from $350 \leq Re \leq 2000$. Experiments were performed in

a towing tank and visualization was accomplished by observing dye washed from the rear of the cylinder. The transition waves first appeared as undulations in the filament lines springing from the separation points. Gerrard (1978) suggested that the two sets of waves are coupled, but the coupling does not seem to arise from the antisymmetry of the street of large-scale Kármán vortices formed in the downstream region. It should also be noted that these waves are observed to be relatively two-dimensional, i.e there is little spanwise phase variation along the length of the cylinder.

Wei and Smith (1986) addressed such waves, manifested in the form of discrete Kelvin-Helmholtz vortices, over the range of Reynolds number extending from Re_d=1,200 to 11,000 using both hydrogen-bubble flow visualization and hot-wire anemometry. They pointed out that the Kelvin-Helmholtz or "secondary" vortices detected in the near wake of the cylinder are identical to the transition waves reported by Bloor (1964), because both phenomena occur immediately downstream of the separation point and appear to have similar unsteady characteristics. They described the origin of the Kelvin-Helmholtz or secondary vortices as instability of the free shear layer separating from the surface of the cylinder.

Ünal and Rockwell (1988) examined the separated shear layer over the range of Reynolds number $440 \leq Re_d \leq 5{,}040$ using combinations of hydrogen-bubble and dye injection visualization, along with hot-film measurements. They observed the onset of the Kelvin-Helmholtz vortices only for Re_d>1,900. The onset and increased prevalence of the Kelvin-Helmholtz vortices are associated with a decrease of the formation length of the large-scale Kármán vortices.

2.1.2. Relation Between Kelvin-Helmholtz and Kármán Vortices

Kelvin-Helmholtz vortices in the shear layer are an essential feature of the transition from a laminar to turbulent state. As a consequence of this transition process, the first Kármán vortex formed from the cylinder at Re_d=5,000 is essentially turbulent. Kármán vortecies from circular cylinder is shown in Figure 2.1. Bloor (1964) addresses the three-dimensional aspects of this transition process using point velocity measurements obtained from hot-wire anemometry. She observed that the

region of transition to turbulence moves upstream towards the cylinder with increasing Reynolds number.

Gerrard (1978) asserts that there is an interaction between the formation of the large-scale Kármán vorticies and transition in the transition waves in the Reynolds number range from 350 to 2,000. His flow visualization photos show that in some cases the transition wave and the roll-up occur in such a fashion that the antisymmetrical formation of the large-scale Kármán vortices is not altered. On the other hand, other photos suggest that the symmetrical formation of the transition waves (i.e., Kelvin-Helmholtz vortices) can actually inhibit the onset of the Kármán vortices.

Flow visualization of Ünal and Rockwell (1988) suggest that the vortices in the shear layer formed a frill on the large-scale Kármán vortex. Hot-film measurements showed no evidence of successive coalescence of the Kelvin-Helmholtz vortices, which would be indicated by appearance of a pronounce subharmonic in the spectrum of the velocity fluctuations. It was, however, observed that as the number of the small-scale vortices increased with increasing Reynolds number, the magnitude of the velocity fluctuation in the shear layer increases as well. This increased fluctuation level may responsible for a type of collective coalescence of the small-scale vortices during formation of the large-scale vortex. It was also noted that the magnitude of the fluctuating kinetic energy at the large-scale Kármán frequency dominates the small-scale frequency.

Roshko (1993) recently suggested that as the Reynolds number increases, each separating shear layer becomes thinner and its instability characteristics change. Correspondingly, there is also an alteration of the Reynolds stress development in each of the separating shear layers. This Reynolds stress variation may play an important role in the near-wake dynamics (Chyu, 1995).

Chyu (1995) investigated the near-wake structure from a circular cylinder using high image density particle image velocimetry (PIV). He pursued both the qausi-two dimensional and three-dimensional flow structure, with the primary intent of determining the structure and development of small-scale vorticity concentrations in the near wake and their interrelationship to the development of the large-scale

Kármán vortices. He concluded that the small-scale vortices have their origin in the convective-type Kelvin-Helmholtz instability in the separating shear layer, which is highly susceptible to external disturbances. In fact, the small-scale Kelvin-Helmholtz vortices are absent at Reynolds numbers as high as Re_d=5000. When these Kelvin-Helmholtz vortices do form, they feed into the large-scale Kármán vortices, in other words, the Kármán vortices are agglomerations of the Kelvin-Helmholtz vortices. He demonstrated that the location of the onset of the Kelvin-Helmholtz vortices, as well as their phase with respect to each other in the shear layer from the bottom and top surfaces of the cylinder, have large influence on the structure an orientation of the Kármán vortices.

2.1.3. Flow Structures in the Wake Region of Different Shaped of Bluff Bodies

Most of researchers have chosen circular cylinder and sphere as bluff body. The popularity of circular cylinder and sphere are attributable to their geometric simplicity, frequent engineering applications and the ease of fabrication of the experimental models. However, from the aesthetic and practical considerations point of view, cylinders with triangular, trapezoidal and polygonal cross-sections are used in engineering. That is the reason to look into wake flow structure downstream of these geometries.

Lou et al. (1994) experimentally investigated the effects of the afterbody shape and the angle of attack (α) on the structure of the flow past a prismatic body. They selected four cylinders with four different cross-sectional shapes, which are a square, two trapeziums and a triangle in their experimental work. They measured the variation of the mean normal force coefficient (C_N) axial force coefficient (C_A) and the Strouhal number (St) with angle of attack (α) in wind tunnel. They also measured vortex street parameters (longitudinal vortex spacing (a), lateral vortex spacing (b), base pressure coefficient and velocity of vortices). Lou et al. (1994) found the angle of attack that corresponds to maximum value of normal force coefficient was the angle of reattachment (α_{re} angle of attack when flow reattachment begins). The

values of α_{re} for square, trapezoidals and triangular cylinders were found to be 12°, 20°, 24° and 32°, respectively. Lou et al. (1994) reported that when the after body shape changes from square to triangle, which is the same as saying when the solid boundary constraint imposes by the sides of the prismatic body onto the inwards curving separated shear layers is reduced, the separated shear layers are able to approach each other and interact more quickly, resulting in a more rapid vortex shedding rate and hence a higher Strouhal number. They found that when the sides of the cylinder are further away from the separated shear layers, a larger angle of attack is needed before one of the separated shear layers would reattach onto the trailing corner of one side. Lou et al. (1994) stated that the wake is narrowest at the reattachment angle of attack for all four shapes. The net effect of increasing α from 0° is an increase in vortex formation length (l_f) when l_f is increased; associated changes in base pressure coefficient (C_{pb}) and axial force coefficient (C_A) also take place. The above continues until the reattachment angle of attack (α_{re}) is reached.

Torii et al. (1998) investigated unsteady laminar fluid transport phenomena over a two-dimensional single diamond-shaped in cross flow. Emphasis was placed on the effects of the Reynolds number and angle of the diamond shape (θ) an the flow pattern. The main parameters for their study are Reynolds number Re=10,400, and diamond angles θ=30°, θ=60°, and θ=90°. They reported that the affect on the flow pattern behind the diamond-shaped island is minor if the Reynolds number is extremely low (Re=10). They observed that for the angles of θ=30° and 60° having Re=50, a pair of vorticies yielded at the rear zone of diamond-shaped island and the flow seemed to be almost stable. In contrast, the disturbance in the velocity vectors behind the diamond cylinder, for θ=90° and Re=50 becomes unstable due to the regular migration of vortices, although the migration give only a slight disturbance to the main flow. Troii et al. (1998) observed that when the Strouhal number for θ=60° and 90° is increased linearly with Reynolds number, whose slopes are in accord with that for a circular cylinder, although the predicted value is smaller than in the wide range of the Reynolds number. In contrast, the Strouhal number for the θ=30° slope is extremely small. Finally, they found the following results; i) very regular vortex

patterns are formed behind the diamond-shaped island and are intensified with an increase in the Reynolds number, ii) have affect on the flow pattern at the rear zone of the diamond-shape island, iii) Struohal number is dependent on Re and θ, and iv) the lower Strouhal number occurs at $\theta=30^{o}$.

Havel and Martinuzzi (1998) investigated the flow around two in line surface-mounted cubes in a thin boundary layer for different obstacle spacing using Laser Doppler Anemometer (LDV) for Reynolds number of $2.2x10^{4}$ based on approach velocity and cube height experimentally. They calculated the mean vector field, Reynolds stress and vortex shedding frequency from the measured velocity. Havel and Martinuzzi (1998) found that the flow separates at the leading edges of the upstream obstacle. They reported for spacings S/H<1.4 (S/H is defined as ratio of obstacle spacing to cube height), the flow reattaches on the roof of the downstream obstacle. For intermediate spacings (1.4<S/H<3.5), the separated shear layer impinges on the leading edge of the downstream cube. Entrainment of fluid from the sides into the inter-cube gap is significant, resulting in notable curvature of the lateral shear layer and increases turbulence levels. For large spacing, the flow reattaches upstream of the second cube leading to the formation of a second horseshoe vortex system.

Hoyt and Sellin (1995) used a new flow-visualization technique to study separated flows around circular, elliptical, and square cylinders at Reynolds number up to $3x10^{4}$. It was stated that there seemed to be very little data on the wakes of non-circular cylinder. The low drag associated with ellipse oriented with major axis aligned with the flow; while the large wake and consequently high drag occurs when the major axis is normal to the flow. Flow past a square cylinder does not develop an organized vortex wake until quite far downstream, where alternating vortices appear. When the square cylinder is rotated 45^{o}, however, a strong pattern of alternating vortices appears.

An experimental investigation of turbulent flow around surface-mounted pyramid in a thin boundary layer was performed by El-Ghusin et al. (1998). They investigated for three different, square-based surface-mounted pyramids placed in a thin boundary layer at a Reynolds number, $Re=3.3x10^{4}$, based on the pyramid height,

h, and the on-coming free-stream flow velocity, U_∞. They tested three pyramids of tip (apex) angles $\xi=45^o$, 60^o and 90^o for four angles of attack which are $\alpha=0^o$ (one face normal to flow), $\alpha=22.5^o$, $\alpha=35^o$ and $\alpha=45^o$. Oil film and smoke visualization were used to document flow behavior as a function of pyramid apex angle (ξ) and angle of attack (α). Laser Doppler and Hot-Wire Anemometry techniques were used to measure the mean velocity field and vortex shedding frequency. El-Ghusin et al. (1998) observed that the reattachment point, in the wake region, moves from 1.62±0.08h, downstream of the pyramid apex, for $\alpha=0^o$ to 2.3±0.07h, 2.56±0.10h and 2.62±0.10h for $\alpha=22.5^o$, 35^o and 45^o, respectively. They found the reason for behavior is that as the angle of attack increases, the angle at which the shear layer separates at the tip decreased. As a result of smaller streamline curvature, the pressure gradient is smaller so that the back-pressure is higher for larger streamline curvature. Suction is greater for smaller streamline curvature, resulting in shorter separation lengths. The reattachment point is located at approximately the same location (1.65h and 1.62h) downstream of the pyramid center for cases of $\xi=60^o$, $\alpha=0^o$ and $\xi=90^o$, $\alpha=0^o$. They stated that the angle of the separating streamline is not strongly attached by but depends strongly. According to El-Ghusin et al. (1998), when the obstacle is placed normal to flow ($\alpha=0^o$), the upstream flow filed was similar to that found for rectangular obstacles. The flow along the pyramid sides, however, exhibits pairs of braided vortex pairs similar to those found delta wings.

Karatekin et al. (1998) performed an experimental investigation on steady and unsteady near-wake characteristics of a sphere-cone bluff body in incompressible flow as a function of incidence angle for Reynolds number of 10^4. They studied on the near-wake region of the body between 0 and 180 degree of angles of incidence in the symmetry plane. They reported that at $\alpha=0^o$ the flow separates at a shoulder of spherical part and the wake have a closure location at approximately x/D=1.8 downstream of the bluff body. The appearance of the two counter rotating vortices in the near-wake is result of light sheet intersecting the vortex ring along the wake's center plane. As the model incidence increases the wake area decreases while the saddle point moves to the lower side of the wake. At the

same time a gradual squeezing of the lower portion of recirculation zone occurs. They found that the wake area reaches a minimum at $\alpha=80^{o}$ in which the saddle point location is on the upper side at a distance of x/D=1.0 from the apex. A further increase in the wake area moves the saddle point back to the lower side, squeezing again the lower recirculation zone. The separation points moves back on the shoulder of spherical part with increasing the incidence further enlarging the wake region. Finally the enlargement of the wake area reaches to the maximum value at $\alpha=180^{o}$.

2.2. Shallow Water Vortices

Free-shear flows lead to vortex generation in shallow water, whereby the characteristic diameter of the vortex is larger than the water depth. This class of vortices occurs in a wide variety of hydraulic, environmental and geophysical flows, including flows in the following categories: flow channels having spanwise variations of either depth or bed friction coefficient; the merging of two rivers; the entrance to a harbor; a sudden expansion of a channel geometry; discharge into a river or lake, and an evacuation region of a coastal lagoon. In addition, flow past large obstacles, such as islands, stranded oil tankers, and large-scale bridge piers can also generate vortices. The onset and development of shallow water vortex systems strongly influences the diffusion of pollutants, thermal mixing, and the erosion of the bed (bottom surface) regimes. In recent years, considerable insight has been provided into the onset and development of shallow water vortices generated in basic classes of shear flows which are mixing layers, wakes, and jets.

2.2.1 Basic Parameters in Shallow Water Flow

In shallow flows, bed friction effects become very important and are quantified in terms of a friction length scale, which is usually defined as the ratio of the depth of flow to bed friction coefficient (C_f). Obviously, the bed friction effects are expected to be minimized in deep flows. For example, the wake region of a bluff body is quite distinct in a deep flow with the formation of well-known Kármán

vortex street, while in a corresponding shallow flow, the wake is stabilized due to friction effects and the vortex street is innihilated (Balachandar et al., 1999).

Chu et al. (1991) proposed a bed friction parameter as a relative measure of stabilizing effect of bed friction and destabilizing effect of transverse shear. Based on an order of magnitude argument, Ingram and Chu (1987) proposed a wake stability parameter as;

$$S = C_f D/h_w \tag{2.1}$$

Here, D denotes the width or diameter of a bluff body and h_w is water depth. The bed friction coefficient C_f was evaluated using the following formula recommended by the A.S.C.E. (Carter et al., 1963):

$$\frac{1}{\sqrt{C_f}} = -4\log\left(\frac{1.25}{Re\sqrt{C_f}}\right) \tag{2.2}$$

in which the Reynolds number given as $Re = 4Uh_w/\nu$ where, U is averaged velocity in sallow water layer. Osaka et al. (1998) proposed an alternative bed friction coefficient derived from a one-seventh-power law for smooth turbulent boundary layer as:

$$C_f = 0.02\,Re_\delta^{-1/6} \tag{2.3}$$

The present C_f values for smooth surface are consistently higher than the low turbulence correlation. In this consideration, Reynolds number is based on boundary layer thickness.

Wolanski et al. (1984) derived an alternative classification for shallow water wakes in the form of the island wake parameter P that is;

$$P = \frac{\bar{U}h^2}{K_z D} \tag{2.4}$$

where $\overline{U}$ is averaged velocity in shallow water layer, K_z is a vertical eddy diffusion coefficient, d is the diameter of the bluff body. The two wake parameter S and P share an inverse relationship where $S \sim (C_f)^{1/2}/P$. As stated by Ingram and Chu (1987), since C_f does not vary substantially from one situation to another the two methods of classification are very similar.

Another important parameter for shallow water flow is Froude number. Froude number is ratio of the inertia force to the force of gravity. Froude number is given as;

$$Fr = \frac{\overline{U}}{\sqrt{gh_w}} \tag{2.5}$$

Here, $\overline{U}$ is averaged velocity in shallow water layer, h_w is the water depth.

2.2.2 Turbulent Mixing Layer and Jets in Shallow Water Layer

Alavian and Chu (1985) investigated the shallow turbulent flow over a compound channel and addressed the stability characteristics of the shear flow; in addition, they experimentally determined the mean velocity distribution and turbulent viscosity coefficient. Gerhard (1986) and Chen and Jirka (1998) and investigated the linear stability of a shallow turbulent mixing layer. Chu and Babarutsi (1988) considered the case of a shallow mixing layer and determined the critical value of the bed friction number for the instability.

Experimental investigation of shallow recirculating flows were conducted by Babarutsi et al. (1989) to study the bed-friction influence in the recirculating zone of a shallow open-channel flow. They concluded that the bed-friction causes reduction in both the length of the recirculating zone and the recirculating flow. The bed-friction generates small-scale turbulence while reducing the effectiveness of the transverse shear. The small-scale turbulence, which has a length scale of the water depth, is generated by bed-friction. In general, bed-friction generates the small-scale turbulent motion and stabilizes the large-scale transverse motions.

Chu et al. (1991) investigated the generation of transverse shear in a shallow open channel flow by either spanwise variations of water depth or bed friction coefficient, and determined the critical value of the bed friction number for the shallow mixing layer.

Babarutsi and Chu (1991) attached a wire mesh to the open channel bed to increase the bed roughness and promote the bed-friction influence on the recirculating flows of a sudden open-channel flow expansion. The diameter of wire was 0.5 mm, and the spacing 5.8 mm. The purpose of their work was to collect concentration data in circulating flows that are under strong bed-friction influence. The mixing layer in the recirculating flow reduces with the increase of the small-scale turbulence and exerts a stabilizing influence on the large-scale turbulence. The mixing layer plays a dominant role in the recirculating flow. The large-scale turbulent motion responsible for the transverse mixing in the recirculating flows is confined to move between the free surface and the channel bed. In the case of small water depth, the large-scale motion is two-dimensional.

Pollutant and waste heat disposal often takes the form of a plane jet discharging into such shallow water layers, which was denoted by Chen and Jirka (1991) in their work as a shallow water jet. In their experimental study, the field distributions of instantaneous concentration were measured by a laser induced fluorescence (LIF) system. The following major results were obtained: (i) All concentration properties of the shallow jet are in scale with the water depth h rather than the slot width, (ii) the concentration half-width grows linearly but faster than for the unbounded case, and (iii) the turbulent properties show a lack of self-preservation with increasing distance; a high degree of fluctuation greatly exceeding that of the unbounded case, and a spectral behavior indicative of two dimensional turbulence.

A study of Tukker (1997) focused on a shallow mixing layer in a confluence of two parallel turbulent streams. The mean velocity difference across the mixing layer gradually decreases while the flow moves further downstream. This effect is attributed to the interaction between the bottom friction and the non-uniform flow. Tukker (1997) pointed out that the bottom shear stress working on the fast stream is larger than the one working on the slow stream due to the difference in the mean

velocity, the fast stream is decelerated and the slow stream is accelerated. Further more, the bottom friction has a stabilizing influence on the Kelvin-Helmholtz instability resulting in a suppression of the growth rate of large-scale instabilities and consequently in a suppression of the spreading rate. Tukker (1997) went on stating that the bottom shear stresses are responsible for a direct transfer of kinetic energy from the large-scale eddies to the small-scale bottom induced turbulence.

The large quasi two-dimensional turbulence structures emerge in a shallow water layer was studied experimentally using LDA by Uijttewaal and Tukker (1998). Velocity profiles and turbulence intensities were measured in the first two meters downstream of the splitter plate. It was concluded in their study that the initial growth rate of the shallow mixing layer was similar to that of a deep water mixing layer.

Chen and Jirka (1999) studied the instability characteristic of free turbulent shear flows, such as mixing layers and jets in shallow water flow. In their study, the governing shallow water instability equation and the numerical solution procedure were presented. They stated that two major parameter, a bed-friction parameter (S) and Reynolds number control the flow behavior. In addition, the width can have secondary influences. They presented the results as stability diagrams for the separate and joint effects of viscosity and bed-friction, respectively.

Altai et al. (1999) investigated the numerical simulations of the planer starting jets. They used a two-length-scale turbulence model to study the effect friction on 2D turbulence in shallow open-channel flow. They compared their simulation results with the experimental results that existed in the open literature. The turbulence energies were divided into large and small scales and calculated by separated models. Finally, Altai et al. (1999) obtained the friction effects on the 2D large-scale turbulence model. Their main findings are; i) to maintain the large-scale turbulence in the shallow shear flow, and ii) the production of turbulence energy by the transverse shear must be greater than the dissipation of the energy by friction.

Uijttewaal and Booji (2000) analyzed the development of two shallow mixing layers with different water depths experimentally by means of LDA. Their results show that bottom friction plays an important role in the growth of mixing layer width

and in strength and dimensions of the large quasi two-dimensional turbulence structures therein.

2.2.3. Wake Region Behind Bluff Body in Shallow Water Flow

Considerable research efforts have been made to improve the physical understanding of two-dimensional turbulent wakes. Many of these studies have been conducted in wind tunnels and water channel where the flow is considered deep and the aspect ratio is high. However, many wake flows encountered in nature and in engineering practice are shallow. In recent past, considerable attention has been directed towards the understanding of the characteristics of shallow wakes.

Wolanski et al. (1984) investigated wakes flow behind Island in shallow coastal waters. They chosen Rattray Island where located northeast Australia to observe wake characteristics behind island. Rattary Island is 1.5 km long, 30 m wide and lies in well-mixed water approximately 25 m deep. Their results show that the length of the wake in the lee of the island, as documented by aerial photographs and satellite imagine, appears to equal that of wake behind a flat in two-dimensional flow at Reynolds number of 10. The further difference between the two dimensional wake behind a bluff body and the flow observed behind Rattary Island is that measured currents in the recirculation region are of the same magnitude as the currents approaching the island. In contrast, the velocity in the recirculation region of two-dimensional bluff body is much smaller, less than 1% that of the free-stream velocity (Keller and Niewstadt, 1973). These differences suggest that the wake recirculation is governed by dynamics other than low Reynolds number, two-dimensional wake flow.

Pattiaratchi et al. (1986) studied on island wakes and headland eddies in shallow coastal waters. Island wakes and headland eddies were identified from spaceborne and airborne remotely sensed imagery in the visible wavelengths. They gave some useful information for wakes formed behind an obstacle at various Reynolds numbers and formed behind an island for various island wake parameter defined by Wolanski et al (1984). The information concerning wake description are given in tables 2.2.1. and 2.2.2.

Table 2.2.1. Description of characteristics of wake formed behind an island, for various island wake parameters, P (Pattiaratchi et al. 1986).

Island wake parameter, P	Wake description
P<<1	Friction dominates, hence quasi-potential flow exits within the wake
P=0-1	Stable wake
P>1	Instabilities occur in the wake
P>>1	Friction is neglible; hence wake is similar to that formed at high Reynolds numbers (i.e., eddy shedding)

Table 2.2.2. Wake formed behind an obstacle at various Reynolds numbers (Pattiaratchi et al. 1986).

Reynolds Number	Wake description
$Re \leq 0.5$	Fluid attached to object (inertial forces negligible)
$2 \leq Re \leq 30$	Two standing eddies, rotating in opposite direction with the main streamlines coming together behind the object
$30 < Re \leq 40$	Unstable wake such that, when Re=34 there is asymmetry in vortices
$40 < Re < 70$	Periodic oscillation of the wake
$60 \leq Re \leq 70$	Shedding of standing eddies behind the object

Shear flows on the effect of bottom (bed) friction around island were studied by Ingram and Chu (1987). The island wake depends on the stability of the shear layers developed along the two sides of island. Ingram and Chu (1987) observed two basic patterns of wake flow around the islands (i) a clear water wake bubble of low turbulence and low sediment concentration. They stated that the turbulent motions in the bay consist of two distinct length scales. The large-scale vortex motions are created by the transverse shear. The small-scale motions, created by bottom shear and limited by water depth, are not visible because of their small length scale when compared to the resolution of the photographs. They made laboratory demonstration of bottom friction influence on turbulent wake in shallow water using shallow water table. A wake stability parameter S was found for wake classification and for correlation of field and laboratory data. Their results showed that vortex street wakes were observed in nine out of 27 events when the wake stability parameter was less

than critical value. This result has consistent with the laboratory and numerical simulation.

The formation of Kármán vortex streets was studied by Schär et al. (1993) within the framework of single-layer shallow water dynamics and in the absence of surface friction and background rotation. Their studies have two parts. In the first part of the study, steady numerical solutions for flow past circular topography were obtained by imposing symmetry condition that essentially suppressed vortex shedding. In the second part, this symmetry condition was relaxed in order to study the transition into the vortex shedding regime. Schär et al. (1993) used finite-difference numerical simulations to derive the most unstable global normal mode of instability of the evolution to finite amplitude of the most unstable global normal mode lead to the break-up of the steady wake into an oscillating Kármán vortex street. The frequency of eddy shedding in their numerical simulations agreed well with that from observations of eddies behind mountainous island.

The influence of bottom friction on mountain induced flows was investigated by Grubišic et al. (1995). They studied the role of bottom friction in creating and dissipating vorticity, as well as its influence on the stability of mountain wakes. In order to understand eddy shedding behind islands and to be able to predict whether an island wake will be steady and unsteady, they studied the stability of mountain wakes in the presence of bottom friction. Their results indicated that the bottom friction has a strong impact on the mean flow characteristics, reducing the width and strength of the velocity deficit region in the wake as well as the wake length. The region absolute instability in the wake was found to coincide approximately with the region of reverse flow in the symmetric wake. For moderate and large values of friction, the convective growth rates were found to be negative in the far downstream part of the wake region as well. There was good agreement between the presence of the region of absolute instability predicted by linear stability analysis and eddy shedding development in full domain numerical simulations. It was concluded that increasing friction (or mountain radius) stabilizes the wake, first near the obstacle by preventing classical eddy shedding, and later by eliminating the remaining unsteadiness from leeward end of the wake.

Chen and Jirka (1995) performed experimental studies on the shallow two-dimensional turbulent wake flows on the large water table. The flow was turbulent throughout the experiments. Wake Reynolds number and ambient Reynolds number were $10^4 \leq Re_d \leq 10^7$ and $Re_h > 1500$ respectively. They inserted different type of blunt bodies in shallow water layer. Namely, cylinders, flat solid plate, porous plates were placed transversely to the ambient flow. It was concluded from the experimental result that the shallow near-wake characteristics of plane wakes were found to consist of three regions: (i) the vortex street type with an oscillating vortex shedding mechanism, (ii) the unsteady bubble wake type with flow instabilities growing downstream of a recirculating bubble attached to the body, and (iii) the steady bubble wake type with an attached bubble followed by a turbulent wake that contains no growing instabilities. Figure 2.2.1 shows these flow patterns, three vortex shedding, unsteady bubble and steady bubble. S represents the wake stability parameter.

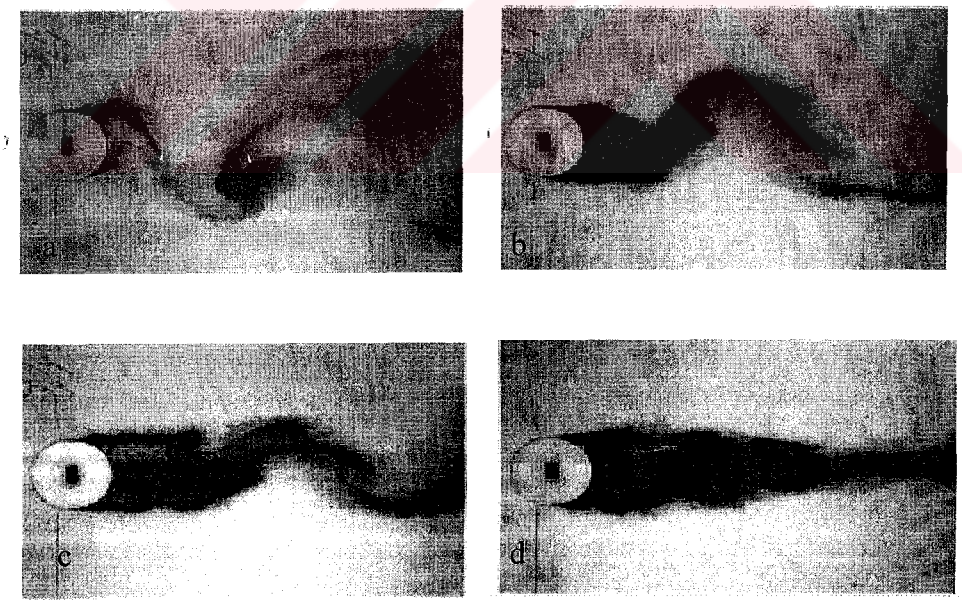

Figure 2.2.1. Schematic flow patterns of a shallow near wake produced by a D=62 cm cylinder (adapted from Chen and Jirka 1995) a) Vortex street pattern, S=0.19, Re_h=5,900; b) unsteady bubble wake, S=0.27, Re_h=3,810; c) unsteady bubble wake with weaker downstream instabilities, S=0.34, Re_h=2,600, and d) steady bubble wake, S=0.53, Re_h=1,800. Reynolds number is based on water depth.

A series of experiments were performed by Lhoyd and Stansby (1997) in order to investigate the recirculating shallow water flow in the wakes of conical model islands with gently sloping sides. Four islands were used with side shapes ranging from 8.0 to 33.1 degrees. For small values of the wake stability parameter, for example $S<0.2$, the island wakes were characterized well-organized vortex shedding systems. The island side slope has small effect on the wakes produced. With slope angles varying from 8.0 to 33.1 degrees, the basic mechanism generating the wake was found to be the same.

Chen and Jirka (1997) showed that in shallow turbulent wake flows, for example and island wake, the flow pattern were experimentally found to be depended mainly on a shallow wake parameter, $S=C_fD/h$, in which C_f is bed friction coefficient, D is the diameter of the cylinder, and h is the water depth. They determined the boundary between absolute and convective instabilities in the near-wake and, furthermore, the condition for which a transformation from a convectively unstable to a convectively stable wake can occur.

Balachandar et al. (1999) developed a theoretical model to predict the spread of wake in shallow flows. They investigated the effects of flow depth and plate width on the spread of the wake. Based on the analytical development and from flow visualization, a critical value of the wake stability parameter was proposed. It was found that for a wake stability parameter greater than this critical value, the conventional Kármán vortex street was annihilated. Based on the results of this study, shallow flows were re-classified as shallow-shallow wakes and deep-shallow wakes. Deep-shallow wakes are those for which a continuous Kármán vortex street was observed, and the flows have characteristics similar to typical two-dimensional wakes generated in wind tunnels. On the other hand, in shallow-shallow wakes, the Kármán vortex street is either annihilated or intermittent. However, in this study, velocity measurements were not made and the nature of the upstream flow boundary layer was not sufficiently known.

Balachandar et al. (2000) investigated characteristics of shallow turbulent near wakes at low Reynolds numbers. Reynolds number based on the test body width was maintained nearly constant ($\approx$4,000). Velocity and concentration in the near

region of shallow turbulent wakes was measured using a LDA and a video-imaging technique. A 40 mm wide flat plate placed normal to the flow was used as wake generator. It was concluded the wake stability parameter pointed out earlier was not quite approximate to characterize the relative effects of transverse and bed friction. In their study, a new definition as a transverse parameter was proposed to characterize wake stability. It was reported that the wake velocity defect data collapse fairly onto a single curve and are independent of the measurement location and depth of flow. The wake half-width data based on the concentration profiles show a higher spread compared with the velocity data.

Tachie and Balachandar (2001) investigated behaviour of shallow turbulent wakes generated on smooth and rough surfaces. They used a flat plate as the wake generator in which placed normal to the flow. The wakes were generated on two types of surfaces: i) a hydraulically smooth surface (brass channel bottom) and ii) a rough surface created using wire mesh. The mesh was made of a 0.6 mm diameter wire with 7.0 mm centreline spacing. The wire was 1.8 m long and 0.45 m wide and was fixed to the channel bottom by means of a double-sided tape. They measured mean and turbulence intensity to understand in shallow wakes generated on smooth and rough surfaces. Using the local minimum and maximum velocity at any axial location to define velocity scale, the velocity profiles across the wake generated on both smooth and rough surfaces collapsed onto a single curve. Their study indicates that for $x/d \leq 5.0$ (d is plate width), the width of the wake increases from the wake generator with increasing axial distance, attains a maximum value at about $x/d=2.0$ and decreases to a minimum value at $x/d=5.0$. It was found that at similar Re_d the spread rate of the wake on a rough surface is significantly lower than observed for a smooth surface due to a stronger bed friction effect.

Balachandar and Tachie (2001) investigated the interaction between the boundary layer on horizontal floor of a shallow open channel flow and the wake of thin flat plate mounted vertically on the floor of channel. They used LDA to measure velocity. Measurements were obtained upstream and downstream of a smooth flat plate wake generator. They used plate with two aspect ratios. Their results showed that the profiles in the near wake region is quite distorted and the recovery of

boundary layer to the upstream condition is slow. They stated that the inner region appeared to develop more quickly than the outer region of boundary layer. When compared with the approaching flow, the streamwise turbulence intensity values increase in the near-wake region followed by a gradual but slow decrease with increasing axial distance.

2.2.4. Turbulent Boundary Layers in Shallow Open Channel

Since turbulent boundary layer plays a very important role in shallow water, many researcher have studied on extensive experiments and analysis of turbulent boundary layers. For example, the estimation of mixing of pollutants in water bodies and sediment transport rates in open channels will be directly influenced by the nature of the turbulent boundary layer.

One should recall that researchers working in closed conduits and pipe flows have carried out extensive experiments and analysis of turbulent boundary layers. Starting with Keulegan's (1938) suggestion, a significant part of this analysis has been essentially borrowed and used in open channel flows, which assumes that there is no Froude number effect. A number of experimental and a few analytical open channel flow investigations have been carried out. The textbook by Nezu and Nakagawa (1993) has come to be accepted as the standard reference for turbulent boundary layers in open channel flow and provides an important collection of data and results. It is presently well understood that the boundary layer characteristics are a function of the momentum thickness Reynolds number. For example, Nezu and Rodi (1986) identified and increasing fullness in the velocity profile with increasing Re_θ and an increasing turbulence intensity with increasing Re_θ. Froude number is generally assumed to have no effect on the friction characteristics of open channel turbulent boundary layers (1988). This agrees with Keulegan's (1938) suggestion that pipe flow formulations could probably be adopted in open channel flow.

Froude number directly relates to the speed of a surface disturbance since, increasing the Froude number causes the surface disturbance to increase (Henderson, 1966). This is particularly important in shallow open channel flows due to the proximity of the boundary layer wake region to the free surface.

Kırkgöz and Ardıçlıoğlu (1997) used a wide variety of water depths in conjunction with a wide variety of velocities. Their experimental results led to an empirical equation in which the dimensionless length of the flow developing zone, L/h, linearly depends on Re/Fr. The correlation between the dimensionless length of the developing zone with Reynolds number and Froude number may be approximated as L/h=76-0.0001xRe/Fr. In this study, this expression will be bared in mind in order to specify the test chamber correctly.

Balachandar and Ramanchandar (1999) presented the results of an experimental investigation of turbulent boundary layers in shallow open channel flows at low Reynolds numbers. They used LDA to measure the velocity of flow. The study was aimed at extending the database toward lower of Reynolds number. They presented primarily concerned with the longitudinal mean velocity, turbulent velocity fluctuations, boundary layer shape parameter and skin friction coefficient for Reynolds number (Re_θ) based on the momentum thickness ranging from 180 and 440. In this range, the results of their investigation in shallow open channel flow indicate a lack of dependence of the von Kármán constant κ on Reynolds number. The extent to which the mean velocity data overlaps with the log-law decreases with decreasing Re_θ. The variation of the strength of the wake with Re_θ is different from the trend proposed earlier by Coles (1956).

Tachie et al. (2000) investigated the effect of roughness on the structure of turbulent boundary layer in open channels. This study was carried out using LDA in shallow flows for three different types of rough surface, as well as a hydraulically smooth surface. The flow Reynolds number based on the boundary layer momentum thickness ranged from 1,400 to 4,000. They observed that the wake parameter varies significantly with the type of surface roughness in contradiction to the "wall similarity" hypothesis. They concluded that wall roughness also lead to higher turbulence levels in the outer region as well as the effect of channel turbulence on the main flow indicates a strong interaction, which must be accounted for in turbulence models.

Balachandar et al. (2001) studied on the characteristics of turbulent boundary layers developing on smooth flat plate in an open channel flow at moderately high

Froude numbers ($0.25 < Fr < 1.1$) and low momentum thickness Reynolds number ($800 < Re_\theta < 2{,}900$). Their study was carried out using a single component using LDA system in open channel flow turbulent boundary layers. They found the following general conclusions: i) For the range of Re_θ studied, the skin friction coefficient values are higher than that noticed in conical zero pressure-gradient flows. The skin friction coefficient shows a decreasing trend with increasing momentum thickness Reynolds number. The skin friction coefficient is not dependent on the Froude number. ii) The log-law is also found to be applicable for range of momentum thickness Reynolds numbers and Froude number ($800 < Re_\theta < 2{,}900$, $0.25 < Fr < 1.1$) studied. The extent of the log-law applicability increased with increasing momentum thickness Reynolds number. The von Kármán constant $\kappa=0.41$ is found to be valid for the open channel flow smooth plate data. iii) The turbulence intensity peak increases for increasing Froude number, at the same momentum thickness Reynolds numbers. At the higher Froude number, a Reynolds number trend is visible in the velocity defect profiles, with the higher Re_θ data deviating further from the curve suggested by Nezu and Nagakawa (1993).

2.3. Outline of Present Study

2.3.1. Overview of Unresolved

The investigation of the flow behind bluff body has been and will continue to be a challenge to the sciences of fluid mechanics in the future. Despite the fact that the wake of a bluff body does not easily admit analytical approaches, it is exceedingly rich in flow phenomena. There has been a surge of experimental discoveries concerning, several aspects of bluff body wakes, but particularly three-dimensional aspects.

Previous investigations have provided valuable features of vortex structures using Laser Doppler Anemometry. This type of instrumentations is restricted to a single point. So, it is not possible to study wake-flow region or a variety of complex features of vortex structures in a plane. There are numbers of point which are directly

pertinent to the present investigation, remain unclarified. The use of the Particle Image Velocimetry (PIV) technique is very attractive in modern fluid mechanics, because it helps to understand unsteady flow phenomena by scanning technique over a certain area of flow field. The measurement of the overall flow field properties, such as instantaneous velocity, vorticity and turbulence intensity are one of most challenging problems. Coherent structures in shear flows or wake flows are extremely unsteady. So, in this type of flow both spatial and temporal information of the entire flow field are required in order to capture instantaneous flow fields and thus to allow the detection spatial structures in unsteady flows quantitatively, which is not possible with other experimental techniques. For this type of flow measurements, Particle Image Velocimetry (PIV) is extremely convenient. This technique has ability to achieve higher accuracy, higher spatial and temporal resolution, and larger observation areas and volumes of experimental data (Raffel et al., 1998).

For the wake behavior behind bluff body in shallow water flow the following issues are unresolved:

(1) The instantaneous flow structure due to the coexisting qausi-two-dimensional vortex structure and small-scale turbulence caused by bottom friction, in terms of velocity and vorticity distribution, is not understood.

(2) The instantaneous patterns of streamline topology near the bed, and manner that they evolve from one form to another during an oscillation cycle of the vortex formation, is not known. Moreover, the relationship between the topology near the bed surface and at elevations above it is unknown. The possibility of defining common topological features, including a specific point that is generic to the flow topology in horizontal planes at various elevations above the bed surface has not been addressed. If such a critical point can be identified, it would serve as a reference for relating other critical points and features of the topology at various elevations in the shallow water layer.

(3) The relation between instantaneous streamline topology and patterns of vorticity has been pursued for a shallow water layer. In particular, this

relationship near the bed, in horizontal planes above the bed, is unknown. For example, consistent occurrence of a critical point, such as a saddle point, in relation to definable displacement and deformation of the vorticity layers from the cylinder, would be important indicator.

(4) The time-averaged streamline topology near the bed, which is consequence of the succession of instantaneous states over oscillation cycle, has not been pursued. This surface topology may exhibit a generic form.

(5) Patterns of averaged vorticity, Reynolds stress, and root-mean-square velocity fluctuations near the surface, in relation to those in horizontal planes above the bed have not been defined.

(6) The effect of controlled shear-layer vortices on the structure of the near-wake of a vertical cylinder in shallow water has not been explored yet.

(7) The effect of approach flow on the instability of the shallow water wake has not been adequately understood yet.

(8) The sensitivity of shallow water wake structure to Reynolds number is unclarified. Both Reynolds number, Re_h, based on water depth, and wake Reynolds number, Re_D, based on diameter of bluff body, are important, but their relative role has not been clarified yet.

(9) The wake structure of horizontal cylinder in shallow water has not been investigated in detail.

2.3.2. Summary of Significant Parameters

In this study, the wake structures behind a vertical and horizontal cylinder are investigated in shallow water flow using a technique of high-image-density Digital Particle Image Velocimetry (DPIV). A circular cylinder having diameter of 50.8 mm was used as the bluff body in this study. The cylinder was located normal to flow in shallow water channel. Water depth h was kept 25.4 mm in all experiments. The value of Reynolds number $Re=U_{max}h_w/\nu=4,498$, where h is water depth, U is free-stream velocity and ν is the kinematic viscosity. The corresponding Reynolds

number based on cylinder diameter is Re_D=8,996. Furthermore, in order to promote development of turbulence in the shallow layer, a trip was placed at the inlet of the test section. It consisted of a cylinder of diameter 1.57 mm wound with a helical wire of diameter 0.90 mm. The pitch of the helical winding was 1.5 mm. Following several preliminary experiments, this method of trip was found to be particularly effective. The values of displacement δ^* and momentum thickness θ are 4.08 and 3.11 mm respectively, giving dimensionless values of $\delta^*/\delta = 0.17$ and $\theta/\delta = 0.13$ respectively.

In section 2 of this study, the strip of roughness, which produces localized disturbances near the bed, was positioned at a distance of L downstream of the base of the cylinder to control near-wake flow region. Extensive preliminary experiments were performed with the aim of determining the most effective value of L/D that yielded significant changes in the near-wake region. It was found that L/D = 0.5 was most effective, and these results are reported herein. The roughness elements had a diameter D_r = 6.4 mm, a center-to-center spacing s = 12.7 mm, and heights h_r = 1.6, 3.2, and 6.4 mm. The dimensionless heights h_r normalized with respect to the thickness δ and momentum thickness θ of the boundary layer were $h_r/\delta = 0.07$, 0.13, and 0.27; and $h_r/\theta = 0.51$, 1.02, and 2.04 respectively.

In deep flow of open channel, flow past a cylinder beneath gives rise to fundamental classes of near-wake structure that are distinctly different from the wake of a completely submerged cylinder. In section 3, it was aimed to characterize the possible states of the wake when the horizontal cylinders having diameters of 19.05 mm, 12.7 mm and 6.35 mm were submerged in the shallow water layer such that their upper surface were coincident with the free-surface. The depth of shallow water height h_w was kept constant. On the other hand, the diameter of cylinder was varied in order to observe the possible existence and orientation of jet-like flow that emerges beneath the bottom surface of the cylinder.

2.3.3. Objective of Present Investigation

- Shallow water vortices are generated in either a large-scale, free-surface

water channel or in a specially designed water tank; both of these systems allow various values of water depth. The objective is to generate well-defined vortices having a characteristic diameter of the same order as, or larger than, the depth of the water. Preliminary experiments allow determination of the most effective means of generation of these vortex systems. The objectives of the present work are briefly summarized below.

- Qualitative flow visualization is employed during the initial scope of experiments in order to determine the overall nature of the complex flow patterns for different configurations of models. The physics of complex flow patterns that give rise to unsteady loading with the eventual intent of implementing control schemes is analyzed.
- Digitally based high-image-density particle image velocimetry is employed to determine the instantaneous and averaged structure of the shallow water vortices. In doing so, it is essential to consider two orthogonal planes of laser sheet visualization. Horizontal planes will allow characterization of the global, quasi-two-dimensional structure of the vortex system at various elevations above the bottom of the channel. Vertical laser sheets allow characterization of side view and end view, in order to emphasize the coherent, three-dimensional motions that eventually alter the quasi-two-dimensional structure of the vortex systems.
- The sequence of images obtained from these techniques of particle image velocimetry will be extensively analyzed using post-processing techniques. Various types of averages of the images, considered together with selected instantaneous images, provide new, fundamental insight into shallow water vortex systems, and the manner in which they influence the bed (bottom surface). As the experimental program unfolds, it may be desirable to employ complementary measurement techniques to characterize the vortex structure and/or the loading on the body that generates the shallow water vortex system.
- The previous studies on wakes generated by objects have dealt with studying the frequency of vortex shedding, drag coefficient, base pressure, location of

flow separation points, organisation of the vortex structures and the wake spread rate. In the present investigation, it is possible to extend the experimental observation further in order to gain further insight into the mechanism that gives rise to the instantaneous patterns of vorticity concentrations. The uses of video imaging procedures have removed many of the limitations associated with conventional instrumentation. One of effective way of studying concentration distribution and the structure of wake flow motion is to introduce dye into the flow and capture video images of the visual flow field. This process is characterised using a sequence of dye images taken with a high-resolution digital camera.

- Instantaneous values of vorticity and velocity vectors will be obtained through numbers of image from cinema sequences. Patterns of instantaneous vorticity and distributions of velocity vectors reveal features of the instantaneous flow structure behind bluff bodies in shallow water layer. Finally it can be stated that the present study also has the following main objectives:

  i) Investigating the vortex formation and structure in the near-wake of the horizontal and vertical cylinder at various elevations of water depth in shallow water and the effect of shallowness on the structure of wake region behind cylinders.

  ii) Observing the relation between instantaneous streamlines topology and patterns of vorticity for a shallow water layer, in particular, this relationship near the bed and in horizontal planes above the bed. For example, consistent occurrence of a critical point, such as saddle point, in relation to definable displacement and deformation of the vorticity layer from bluff body, would be an important indicator.

  iii) Defining the patterns of averaged vorticity, Reynolds stress, and the root-mean-square velocity fluctuation near the bed surface of the water channel in relation to those in horizontal planes above the bed.

iv) Controlling of vortex formation from bluff body in shallow water by the placement of a narrow transverse strip of roughness elements on the bottom surface of the water channel.

2.3.4. Outline of Dissertation

Introduction part introduces briefly the practical and importance of the present work.

Literature survey part summarizes the wake region structure both in deep water and shallow water flow. Unresolved issues, which are deducted from previous investigations and objectives for the present study, are given.

Material and Method part describes the details of the experimental system and measurement techniques. Particularly, the details of Digital Image Velocimetry (DPIV) and image processing used in the present study are given.

Result and discussion part of present study is divided into three parts.

i) The first part reports wake structure behind a vertical cylinder and the effect of shallowness on the near-wake region in the shallow water flow is given in section 4.1.

ii) The control of vortex formation from a vertical cylinder in shallow water by the placement of a narrow transverse strip of roughness elements on the bed of the water channel is reported in section 4.2.

iii) Flow structure from the horizontal cylinder piercing a shallow water layer is reported in section 4.3.

Finally conclusions and recommendations part summarizes the main findings of the present work and provides recommendations for further investigations as a future work.

3. MATERIAL AND METHOD

3.1. Measurement Techniques

3.1.1. Particle-Imaging Techniques

One of the most challenging problems in fluid mechanics is the measurement of the overall flow field properties, such as the velocity, vorticity, and pressure fields. Local measurements of the velocity field (i.e., individual points) are now measured using Hot-Wire (HW) and Laser Doppler Velocimetry (LDV). However, many flow fields such as coherent structures in shear flows or wake flows, are highly unsteady. HW or LDV data of such flows are difficult to interpret, as both spatial and temporal information of the entire flow field are required, and these methods are commonly limited to simultaneous measurement at only a few spatial locations. Hence, a whole field velocity measurement technique is valuable in the characterization of these flow fields. Some of these techniques are; Tomographic interferometry (Hessenlink, 1988), Laser-speckle velocimetry, Particle-tracking velocimetry (Miles et al., (1989), Particle Image velocimetry for velocity fields (Arian, 1991; Rockwell et al., 1993) and Digital Particle Image velocimetry (Willert, 1991; Westerweel, 1997).

The experimental set-up of PIV system typically consists of several subsystems. In most applications tracer particles have to be added to the flow. These particles have to be illuminated in a plane of the flow at least twice within a short time interval. The light scattered by the particles has to be recorded either on single or on a sequence of frames. The displacement of the particle images between the light pulses has to be determined through evaluation of the PIV recordings. In order to be able to handle the great amount of data which can be collected employing the PIV technique, sophisticated post-processing is required. Figure 3.1.1 briefly explains a typical set up for PIV recording. Small tracer particles are added to the flow. A plane (light sheet) within the flow is illuminated twice by means of a laser (the time delay between pulses depending on the mean flow velocity and the magnification at imaging). It is assumed that the tracer particles move with local velocity between the two illuminations. The light scattered by the tracer particles is

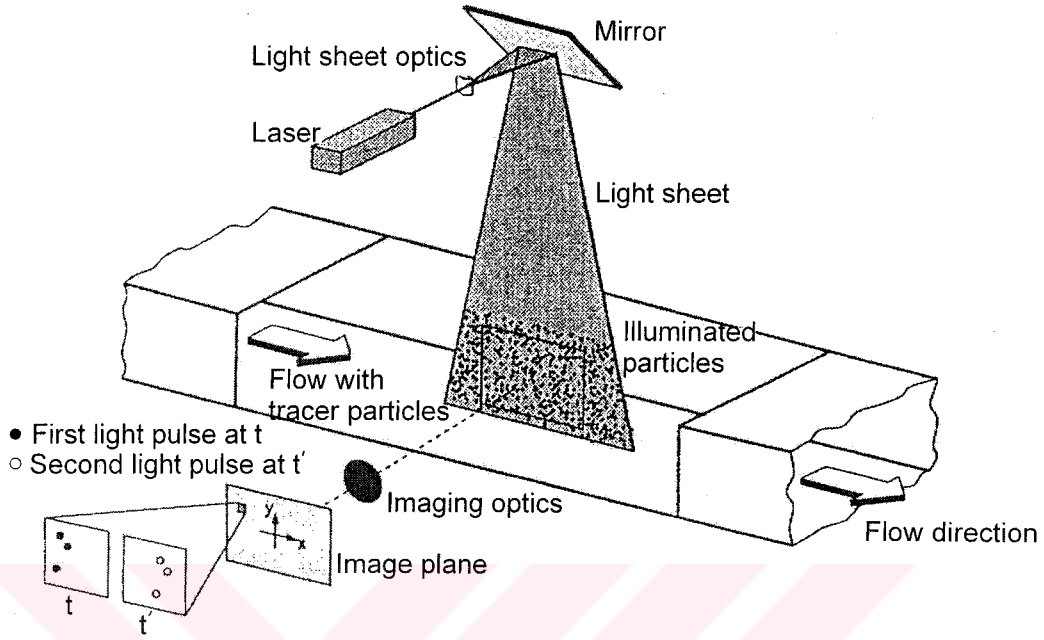

Figure 3.1.1. A typical experimental set-up for PIV technique.

recorded via a high quality lens either on a single photographical negative or on two separate frames on a special cross correlation CCD camera. After development the photographical PIV recording is digitized by means of a scanner. The output of the CDD camera is stored in real time in the memory of a computer directly. As the resolution and image format of CDD camera is several orders of magnitude lower than that of a photographic medium, digitization cannot be ignored.

For evaluation, the digital PIV recording is divided in small subareas called interrogation areas (windows). The local displacement vector for the images of the tracers particle of the first and second illumination is determined for each interrogation area by means methods (auto- and cross-correlation explained in section 3.1.2). It is assumed that all particles within one interrogation area have moved homogenously between the two illuminations. The projection of the vector of the local velocity into the plane of the light sheet (2-compoanent velocity vector) is calculated taking into account the time delay between the two illuminations and the magnification at imaging.

The process of interrogation is repeated for all interrogation areas of the PIV recording. With CDD cameras it is possible to capture more than 100 PIV recordings per minute. The evaluation of one camera PIV recording with 3600 instantaneous velocity vectors (depending on the size of the recording and of the interrogation area) is of order of a few seconds with standard computers. If even faster availability of the data is required for on line monitoring of the flow, dedicated hardware processors are commercially available which perform evaluations of similar quality within fractions of a second.

3.1.2. Correlation Process

Particle Image Velocimetry processing basically determines the distance that the particles have moved in the time between laser illuminations in photographic based or laser pulses in digital PIV. The most common methods to determine this distance are particle tracking or correlation. Here, correlation method which can be auto-correlation, one-frame cross-correlation and two-frame cross-correlation will be explained briefly. The differences in these correlation techniques are the image window areas for the first and second images. In the auto-correlation, the same image window is used for both first and second image window. In the one-frame cross-correlation, the second image window is offset in the flow direction from the first image on the same window. The processing of the one-frame cross-correlation depends on the amount of overlap between the first and second image windows. In two-frame cross-correlation, the first image window located on the first frame and the second image window is located on the second frame. Both interrogation windows in time delay image have the same coordinate.

The correlation field shows the dominant distance between each particle and every other particle within the interrogation spot. The maximum intensity spot, which represent the correlation of each particle image with itself, is located in the center. A second peak, called the positive displacement peak that correspond to the dominant particle spacing. The auto-correlation function is symmetrical so that each displacement peak has a peak of equal size in the opposite direction. One peak represents the distance between the first and second particle images forward velocity,

the other is distance between the second and first particle images in the reverse velocity. If there are no negative velocities in the flow, then the correct peak is easily identified. If there are flow reversals in the flow field, image shifting by means of an oscillating bias mirror is used to resolve the directional ambiguity in based the photographic PIV.

One can explain mathematical approach for auto-correlation by considering an interrogation window of a doubly exposed photographic image frame with uniform particle displacements. The ensemble of the particle image doublets is represented by the function D(x,y)

$$D(x,y) = I(x,y) + I(x+\Delta x, y+\Delta y) \tag{3.1}$$

where $I(x,y)$ and $I(x+\Delta x, y+\Delta y)$ represent the images of the particles recorded during the first and second exposure, and $\bar{s}(\Delta x, \Delta y)$ is the average particle displacement. For the sake of simplicity, it is assumed that all the particle images have a corresponding pair, i.e; purely two-dimensional motion, and that the size of the region being interrogated is large when compared with the particle displacement. Equation (3.1) is written in the following form

$$D(x,y) = I(x,y) \otimes [\delta(x,y) + \delta(x+\Delta x, y+\Delta y)] \tag{3.2}$$

Where δ (x,y) is Dirac delta function centered at $\bar{x}(x,y)$ and ⊗ is the convolution operator. Fourier analysis provides us with a convenient means to obtain the auto-correlation function. Two Fourier transformations are required. The Fourier transform of D(x,y) is represent by $F\{D(x,y)\} = D^*(\omega_x, \omega_y)$, where F is the Fourier transform operator, ω_x, ω_y are the spatial frequencies along the x and y directions respectively

$$D^*(\omega_x, \omega_y) = I^*(\omega_x, \omega_y)\left[1 + e^{-2\pi j(\Delta x \omega_x + \Delta y \omega_y)}\right] \tag{3.3}$$

where $I^*(\omega_x,\omega_y)$ represents the Fourier transform of the collection of particle image. The spectrum is obtained by multiplication of Equation (3.3) with its conjugate, resulting in

$$\left|D^*\left(\omega_x,\omega_y\right)\right|^2 = 2\left|I^*\left(\omega_x,\omega_y\right)\right|^2\left(1+\cos\left[2\pi\left(\Delta x\omega_x+\Delta y\omega_y\right)\right]\right) \tag{3.4}$$

where $\left|I^*\left(\omega_x,\omega_y\right)\right|^2$ represent the spectrum of the collection of particle image at random location. Spectrum of strong self-correlation peak locates at $\bar{s}(0,0)$. In addition to the self-correlation peak, there are two strong symmetrical displacement peaks, positive displacement peak located $\bar{s}(\Delta x,\Delta y)$ and negative displacement peak located $\bar{s}(-\Delta x,-\Delta y)$. There are number of noise peaks resulting from random overlap of particle image as well. The strength of the displacement correlation peaks is proportional to the number of exposed particle pairs in the interrogation window. After determination of the average particle displacement, one can calculate the velocity components by dividing the displacement with the exposure time.

In the cross-correlation mode of operation, the technique requires that each image produced by the two illumination pulses be stored in separate frames. The distance and direction traveled by the tracer particles is then unambiguously determined by performing the cross correlation between the two small and corresponding regions of the image frame acquired in quick succession. Consider the two small regions corresponding to the first and second exposure, respectively

$$D_1(x,y) = I(x,y) \tag{3.5}$$

and

$$D(x,y) = I(x+\Delta x, y+\Delta y) = I(x,y)\otimes\left[\delta(x+\Delta x, y+\Delta y)\right] \tag{3.6}$$

The cross correlation may also be obtained using Fourier transform operator. However, three Fourier transforms are required. First, the transform of $D_1(x,y)$ and $D_2(x,y)$ are evaluated

$$F\{D_1(x,y)\} = I^*(x,y) \tag{3.7}$$

and

$$F\{D_2(x,y)\} = I^*(x,y)\left(e^{-2\pi j(\Delta x\omega_x + \Delta y\omega_y)}\right) \tag{3.8}$$

The cross-correlation function, G (x,y), is obtained by evaluating the Fourier transform of the product $F\{D_1(x,y)\}.F\{D_2(x,y)\}$,

$$F\{D_1(x,y)\}.F\{D_2(x,y)\} = I^*(x,y)^2.\left(e^{-2\pi j(\Delta x\omega_x + \Delta y\omega_y)}\right) \tag{3.9}$$

and

$$G(x,y) = \iint I^{*2} e^{-2\pi j(\Delta x\omega_x + \Delta y\omega_y)} e^{-2\pi j(\Delta x\omega_x + \Delta y\omega_y)} d\omega_x d\omega y \tag{3.9}$$

resulting in

$$G(x,y) = F\{I^{*2}\} \otimes [\delta(\Delta x, \Delta y)] \tag{3.10}$$

The cross correlation G(x,y) is thus a function centered at (Δx, Δy), the average displacement coordinates. In contrast with the auto-correlation, there is only one correlation peak, with much larger signal amplitude. The main advantages of the cross-correlation approach over the auto-correlation are: i) the displacement is obtained without any directional ambiguity, and ii) the correlation peak signal carries

more signal strength, and thus is more immune to noise. The main disadvantages of the cross-correlation approach are that i) the computation is more expensive in time, as three two-dimensional Fourier transforms are required instead of two for the auto-correlation, and ii) the image acquisition system (camera) must cope with the necessity of acquiring two image frames in quick succession in synchronization with the laser illumination pulses and register the frame position with respect to the flow with absolute precision. In this study, cross-correlation technique was used to determine the distance when particles move in the period of a specified time of two laser illuminations.

3.1.3. Seeding, Illumination and Exposure

3.1.3.1. Seeding

Although the principle of PIV is based on the direct determination of two fundamental dimensions of the velocity which are length and time, this technique initially measures the velocity of particles. Therefore, properties of the particles have to be checked in order to avoid significant discrepancies between fluid and particle motion.

These particles must be small enough to track the flow accurately, yet large enough to scatter sufficient light for the camera in order to be detected. Ideally, particles should also be neutrally buoyant in the fluid that is they should have approximately the same density as the fluid itself.

In general, most of the seeding considerations in LDA also apply to PIV. Durst et al. (1981) state the following desired properties of seeding particles:

- Able to follow the flow
- Good light scatterers
- Conveniently generated
- Cheap
- Non-toxic, non-corrosive, non-abrasive
- Non-volatile, or slow to evaporate
- Chemically inactive

- Clean

In general the motion of particles suspended in a fluid is affected by

- particle shape
- particle size
- relative density of particle and fluid
- concentration of particles in the fluid
- body forces

The shape of the seeding particles affect the drag exerted on the particle the surrounding fluid, and the size of the particles along with their relative density influence their response to velocity changes of the surrounding fluid.

The concentration of particles affects particle motion through interaction between different particles. In practice, the concentrations used are normally so low, that the particles on the average are separated from each other by the particle-diameters, and so particle interaction can usually be neglected.

The choice of seeding depends on a number of parameters. Primarily the seeding material should be chosen considering the flow that is to be measured, and the illumination system available. In general seeding particles should be chosen as large as possible in order to scatter the most light, but the particle size is limited, since too large particles will not track the flow properly. In general the maximum allowable particle size decrease with increasing flow velocity, turbulence and velocity gradients.

It should be aware that the camera images of seeding particles should have a diameter of at least 2 pixels, preferably 3 pixels or more. This will allow the system to estimate particle positions and displacements to subpixel accuracy, effectively increasing the resolution of the technique.

Finally it should be considered how the flow is seeded. Water flows are often implemented using water in a closed circuit, and here commercial seeding particles can be used.

3.1.3.2. Illumination and Exposure

In the PIV technique, the light scattered by seeding particles moving in the flow field provides a signal when it is recorded on a digital camera. Both the initial and final positions of the seeding particles are to be captured so the displacement between them can be measured. Thus the PIV illumination method should fulfill the following basic criteria:

- The light budget should be sufficiently high to ensure the intensity of scattered light from the seeding particles is such that images of them can be recorded on the PIV camera, above the optical noise level of the system.
- The duration of the light pulse should be such that the particle does not move significantly during its exposure to the light-pulse.
- The time between successive light pulses should be such that the flow field does not move significantly.
- The location and dimensions of the measurement plane should be well-defined.

In PIV, the Neodym-YAG laser (Nd:YAG) is most commonly used as a pulsed laser. This laser system, Nd:YAG, is the most important solid-state laser for PIV in which the beam is generated by Nd^{3+} ions. Nd^{3+} ion can be incorporated into various host materials. For laser applications, YAG crystals (yttrium-aluminum-garnet) are commonly used. Nd:YAG lasers have a high amplification and good mechanical and thermal properties. A flash lamp and a YAG crystal are placed at the two origins of a mirrored elliptical cavity to maximize the energy transfer from the flash lamp to the crystal. The flash lamp excites the cavity for a short time and the excess heat build-up is thermally dissipated by cooling water before the next pulse of the flash lamp.

The most optimal method of achieving two pulses for PIV with variable time interval is to use a dedicated PIV-laser with two lasing cavities. This allows a large freedom in selecting the time interval between pulses and the beam energy in each

pulse remain the same no matter what the time between pulses. Figure 3.1.2. shows the schematic double-cavity PIV laser.

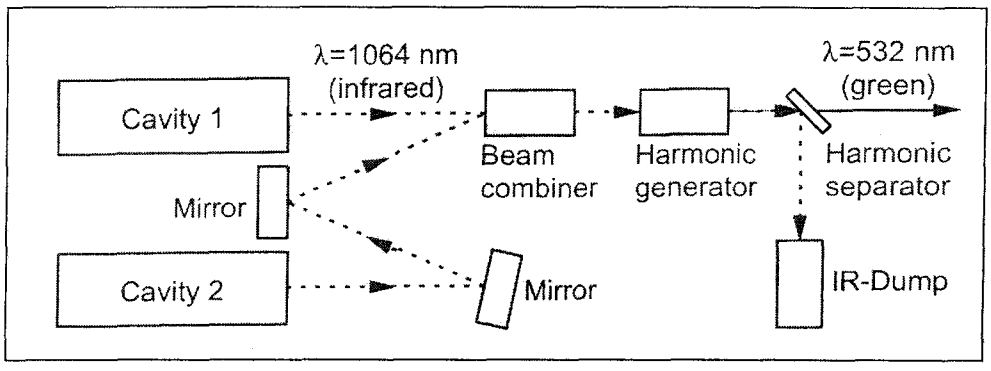

Figure 3.1.2. Double-cavity Nd:YAG laser

Additional optics is inserted so that the beam paths from the cavities can be combined along the same optical path, and furthermore a harmonic generator and a harmonic separator is used to bring the light into the visible spectrum.

The Nd:YAG lasers emit light with a wavelength of 1064 nm which is in the infra-red. For PIV purposes, this wavelength is very useful since most cameras are not sensitive to it. Generally cameras are more sensitive to the blue-green spectrum, and furthermore, there are many practical difficulties when attempting to align a beam path it cannot be seen, particularly when the laser power is classified hazard. Therefore, for PIV, Q-switched YAG lasers are also frequency-doubled. That is, the wavelength of the laser pulse is halved to 532 nm (the light's frequency doubles) by a device called a second harmonic generator. Harmonic generators are not efficient and so a need to dump the residual infra-red before allowing the pulsing beam to leave the laser. This is done by optical component called a harmonic separator.

In order to improve the beam profile which is sometimes very poor, even if it specified to be 80 % Gaussian in the near and 95 % in the far field. Two laser systems of the same manufacturer often have different beam properties depending on the laser rod properties, and the alignment of the laser. Since a good beam profile is absolutely essential for PIV, it must be specified not only in the near and in the far field but also in the mid-field in a distance of 2-10 m from laser. The description of the beam intensity distribution should not only be based on a good fit to a Gaussian

distribution, but also on the minimum and maximum energy in order to ensure a hole-free intensity distribution without hot spots (Raffel et al., 1998).

In figure 3.1.3 (Raffel et al., 1998), the intensity profiles versus the light sheet thickness measured at four different distances from the laser are shown. The peak value of the distribution was adjusted close to full scale for each position (1.8 m, 3.3 m, 4.3 m, 5.8 m). It can be seen that the thickness of the light sheet increases slowly with the distance from laser. A small side peak is visible at every position but seems to vanish at 5.8 meters. The fluctuations in the distribution are minimized at position three (4.3 m). When assessing these light sheet profiles it has to be taken into account that the loss of correlation during the evaluation of PIV recordings is mainly influenced by the light sheet intensity distribution at recording. The light energy contained in the side peak will be lost in most situations, because a very small flow component in the lateral direction would displace from bright towards dark areas and would therefore lead to only one illumination of the tracer particles. For flow fields without any significant out-of-plane velocity component the light sheet can be focused more precisely and a better, more Gaussian-like, intensity profile can be obtained in the out-of-plane direction. However, even in those cases the intensity profile versus the light sheet height strongly depends on the laser beam properties. If data is lost some regions of the observation area due to insufficient illumination, the result of the whole measurement may become questionable.

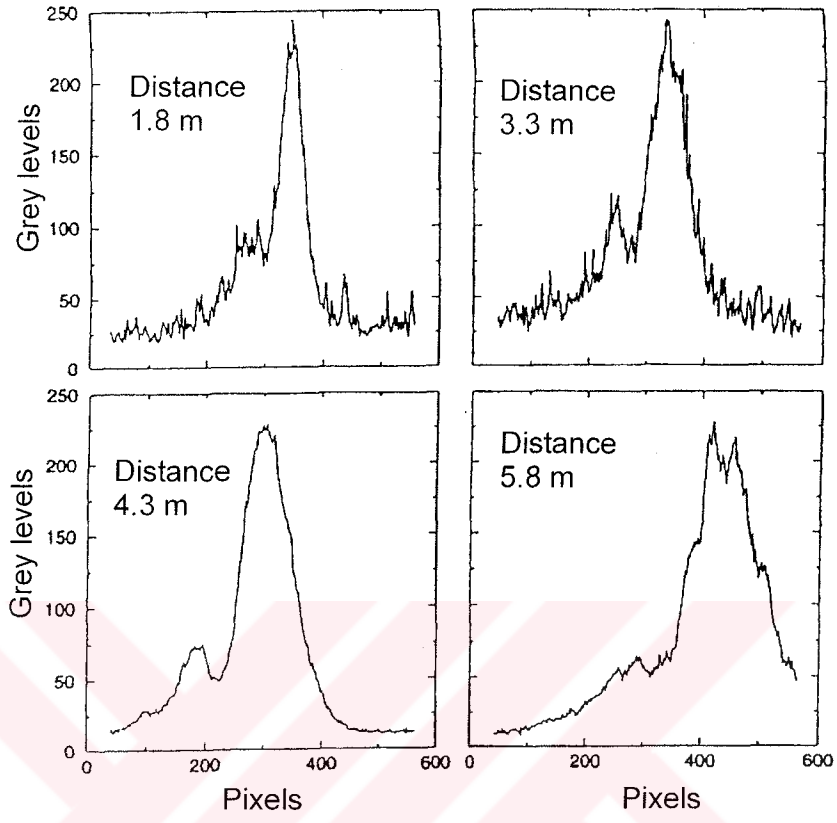

Figure 3.1.3. Evolution of the light sheet profile with increasing distance from the laser (from Raffel et al., 1998).

3.2. Experimental Arrangement

3.2.1. Water Channel System

Experiments were carried out in a recirculating free-surface water channel located in the Fluid Mechanics Laboratory at Lehigh University, U.S.A., shown in Figure 3.2.1. The water channel test section was constructed of transparent plexiglass with upstream and downstream PVC reservoirs, which have a cross-section of 610 mm x 610 mm and a length of 4,318 mm. The main section is preceded by a large contraction having an inlet width of 1,829 mm; the corresponding contraction ratio is therefore 3:1. A honeycomb–screen system is located at the entrance of the contraction in order to minimize the free-stream turbulence, which is typically less than 0.1%. The water flow speed was controlled by an axial flow pump, which provides reliable test flow speeds. During the course of all experiments the water was

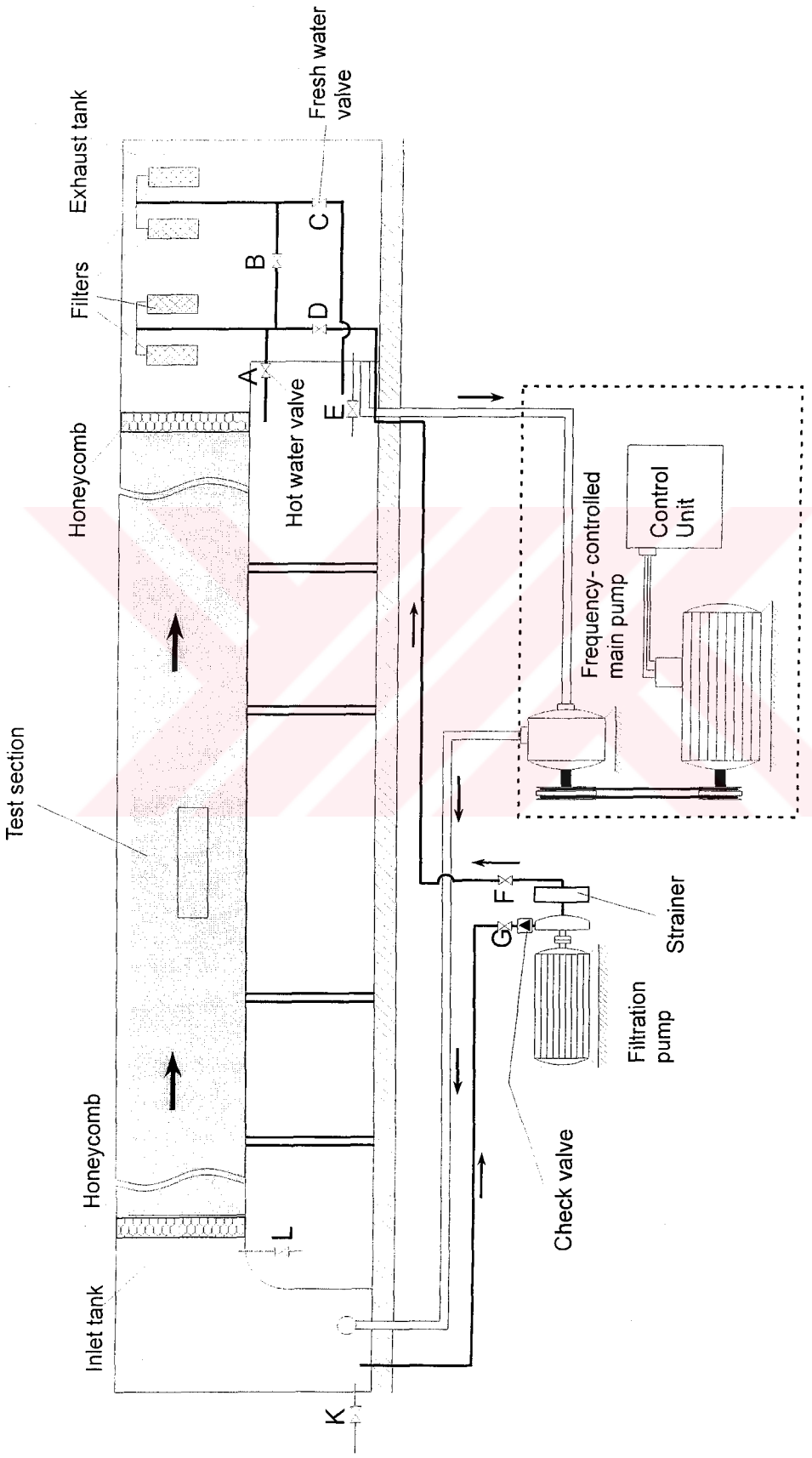

Figure 3.2.1. Schematic of the water channel.

maintained at a height of 25.4 mm. The free-stream velocity was U=177.8 mm/sec and Reynolds number based on water depth was Re=4,498.

3.2.2. Experimental Model

An overview of the experimental system is given in Figure 3.2.2 and Figure 3.2.3. In section 1, a vertical cylinder pierced the free-surface. The cylinder having diameter of 50.8 mm was positioned at a distance of 2,845 mm for from the leading-edge of the test section in order to allow development of a fully-turbulent boundary layer, according to the criteria of Kırkgöz and Ardıçlıoğlu (1997). In order to promote development of turbulence in the shallow layer, a trip was placed at the inlet of the test section. It consisted of two cylinders of diameter 1.57 mm wound with a helical wire of diameter 0.90 mm. The pitch of the helical winding was 1.55 mm. After performing several preliminary experiments, this method of trip was found to be particularly effective.

As indicated in Figure 3.2.2, a strip of roughness, which produces a localized disturbances at the bed, was positioned at a distance of L downstream of the base of the cylinder. The roughness elements had a diameter D_r =6.4 mm, a center-to-center spacing S=12.7 mm, and heights h_r= 1.6, 3.2, and 6.4 mm respectively. The dimensionless heights h_r normalized by the depth h_w of the water layer were h_r/h_w=0.062, 0.125 and 0.25 respectively.

The orientations of the laser sheet and camera systems for vertical cylinder are given in Figure 3.2.2. The flow was illuminated with a double-pulsed system consisting of two Nd:YAG pulsed lasers (532 nm), which operated nominally at 120 mJ per pulse. The optimal thickness of the laser sheet in the field of view was generated by combination of spherical and cylindrical lenses. The thickness of the sheet was approximately 1.5 mm. The spreading angle of the laser sheet is indicated in Figure 3.2.2. The sheet was located at various distances of h_L above the bed (bottom surface) of the test section.

Figure 3.2.3 shows the orientations of the laser sheet and camera system for horizontal cylinder. A horizontal cylinder of diameter D was located at a distance of 2,845 mm downstream of the channel inlet. Three different cylinder diameters

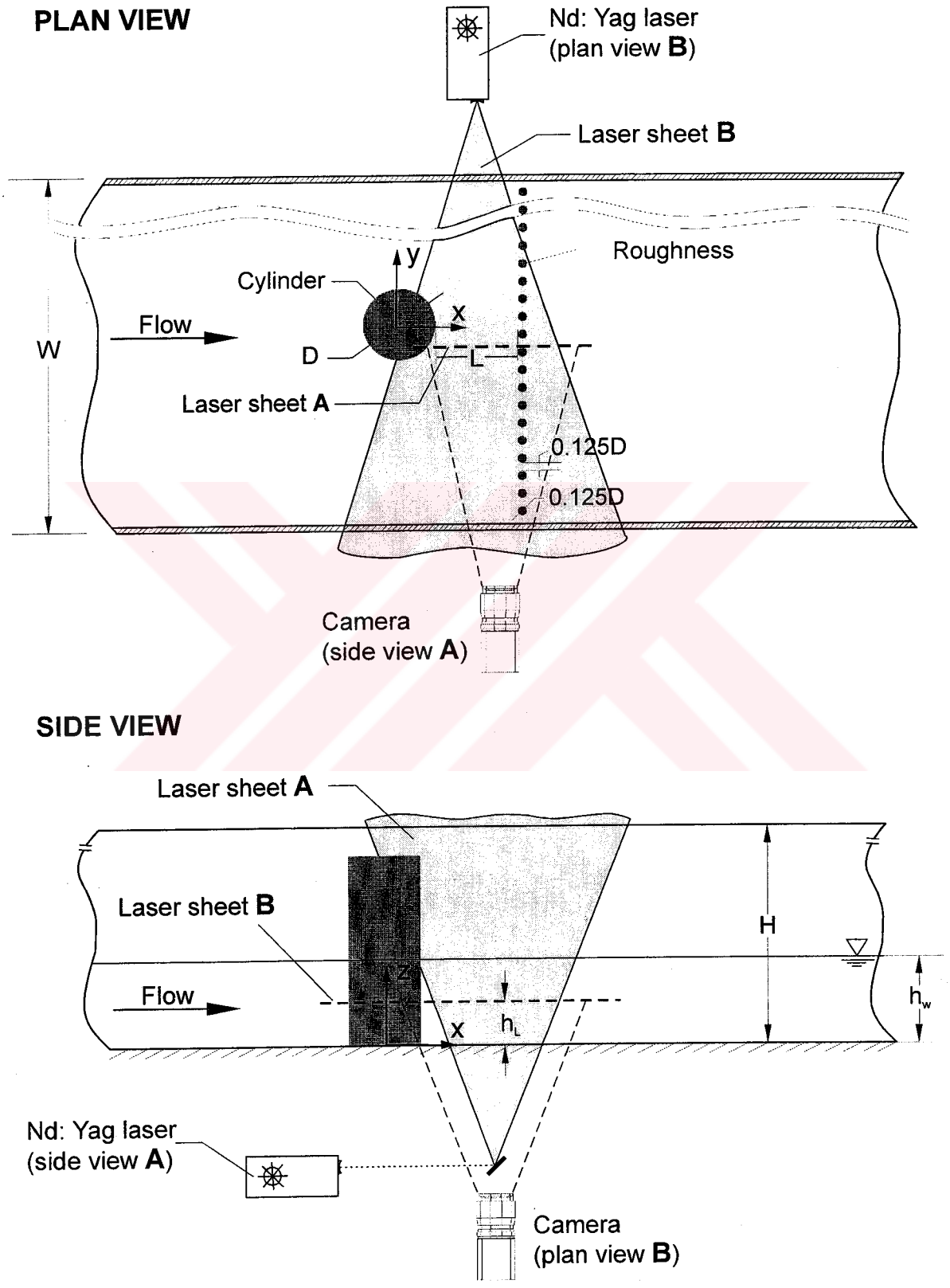

Figure 3.2.2. Overview of a vertical cylinder in shallow water, location of roughness elements, and deployment of laser sheet at various elevations above the bed.

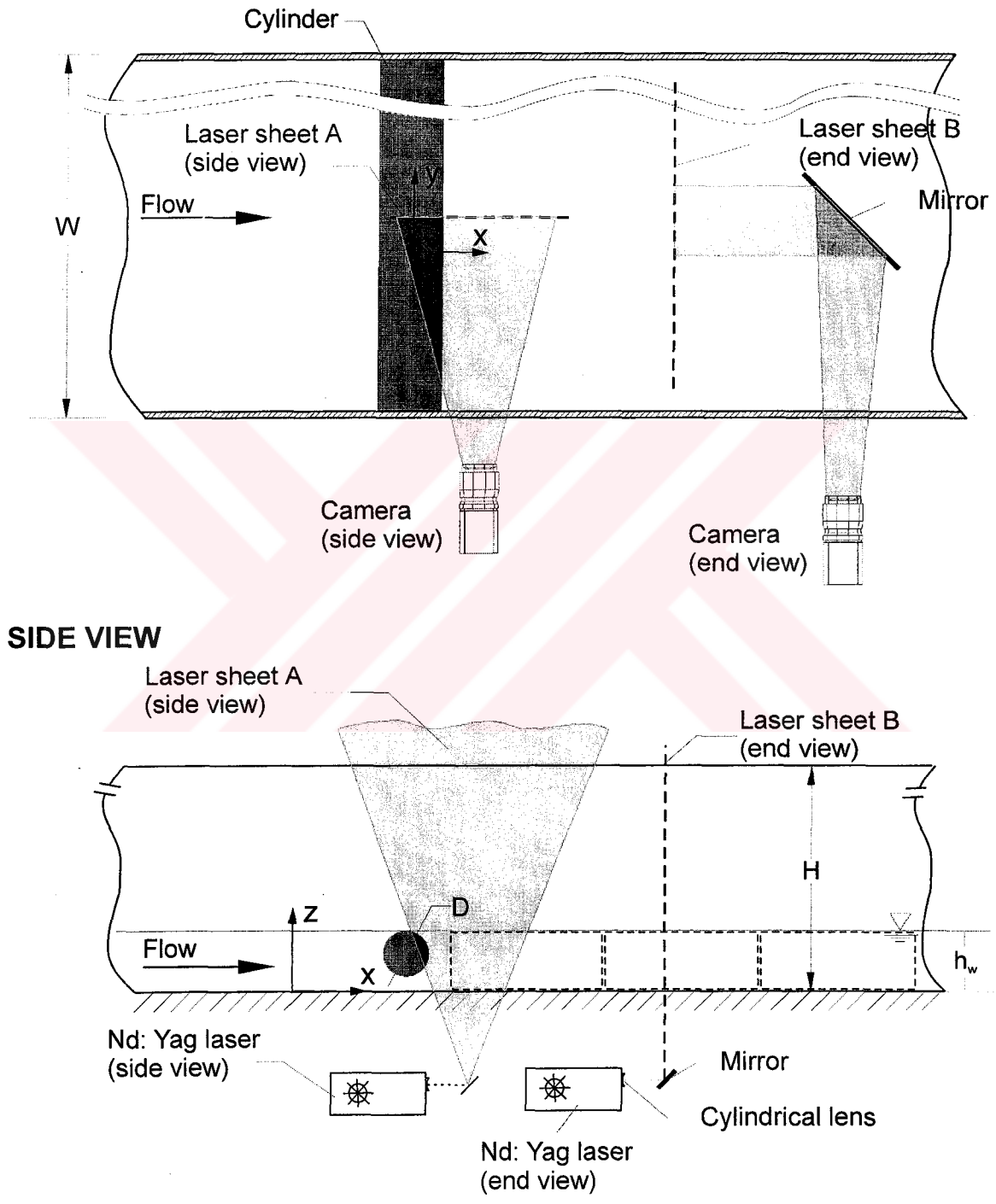

Figure 3.2.3. Overview of a horizontal cylinder in shallow water, and deployment of laser sheet.

D=19.05 mm, 12.70 mm and 6.35 mm were employed. Since the water depth was maintained constant at 25.5 mm, the values of diamensionless diameter were D/h_w=075, 0.50 and 0.25 respectively. The corresponding values of Reynolds numbers based on the cylinder diameter were Re=3,373.6, 2,249.1 and 1,124.6 respectively. Furthermore, it is possible to define a Froude number based on the cylinder diameter D according to $Fr = U_{max}/\sqrt{gD}$ =0.41, 0.50 and 0.71. The value of Froude number based on water depth h_w was $Fr = U_{max}/\sqrt{gh_w}$ =0.36.

During the course of the experiments with horizontal cylinder, images were acquired over different fields of view which were indicated in the schematic of Figure 3.2.3. This approach was necessary in order to attain sufficient spatial resolution. Images acquired in each of these fields of view were averaged, and by splicing them together, it is possible to define this flow structure over a relatively long streamwise distance of the shallow water layer.

3.3. Image Acquisition

Schematic of DPIV system used in this study is shown in Figure 3.3.1. This laser system illuminated 14.6 micron, metallic-coated hollow plastic spheres, which were essentially neutrally buoyant. The flow was seeded throughout the entire shallow water layer prior to performing each experiment. Two Nd:YAG pulsed lasers (532 nm) and the light sheet optics were used to illuminate the test section. The light sheet optics included the cylindrical and spherical lenses. The cylindrical lens is used to diverge the laser beam. The spherical lens controlled the light sheet thickness. Patterns of particle images were acquired by a Model 630046 PIVCAM 10-30 charge-coupled device (CDD) camera. The camera was placed at right angles to the light sheet. The camera was equipped with a 55 mm lens. PIVCAM 10-30 has an Asynchronous Double Exposure mode that allows a frame straddle pair of images to be captured less than in 300 μs after an external trigger signal. The digital images were analyzed using INSIGHT software of TSI. A Frame Grabber in the computer read the camera image from the CDD camera and stores it as a digital image in the RAM of the computer. The digital image of the flow processed by the INSIGHT

software. The synchronizer was used to trigger the laser and the camera with the correct sequence and timing.

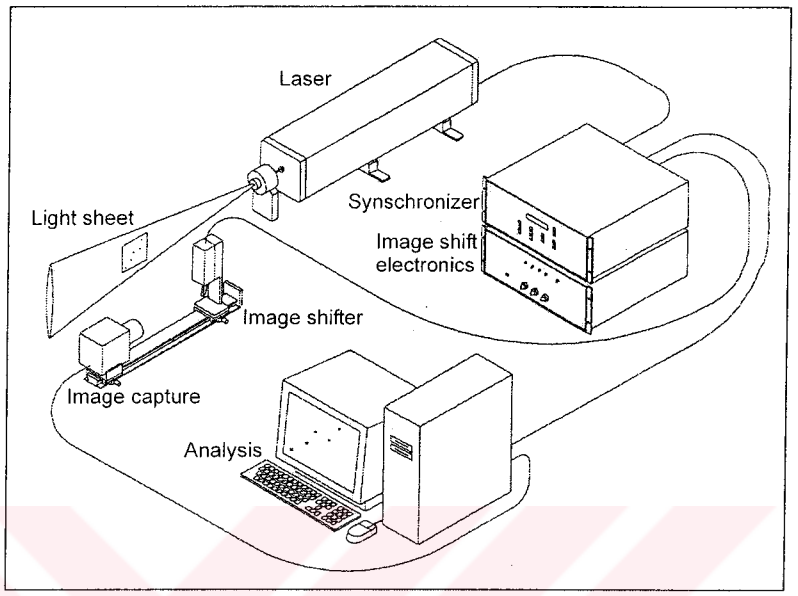

Figure 3.3.1. Typical digital particle imagine system

3.4. Image Post-Processing

General procedure for the image processing is presented in Figure 3.4.1. Images were received from a CDD camera that has a resolution of 1000 pixels x 1016 pixels at a rate of 15 frames per second. The time delay changes from 2 ms and 3 ms between frames. Digital image was analyzed using INSIGHT software. The image was recorded on a CDD array. A Frame Grabber in the computer read the camera image from the CDD camera and stored it as the digital image file format (TIFF) (Figure 3.4.2.) in the RAM. This digital image was processed and analyzed using the INSIGHT software. During each continuous run, a total of 136 images were taken. In order to determine the velocity field, a cross-correlation technique, with a 16x16 interrogation window, was employed, with an overlap of 50 %. The magnification factor of lens was 1:11.3. The magnification factor $M=L_i/L_r$, where L_i is the length scale of the image on the camera and L_r is the real physical length scale of the scene. The camera images are divided into rectangular regions called interrogation areas or interrogation windows, and for each of these interrogation windows the image from the first and the second pulse of the light sheet are

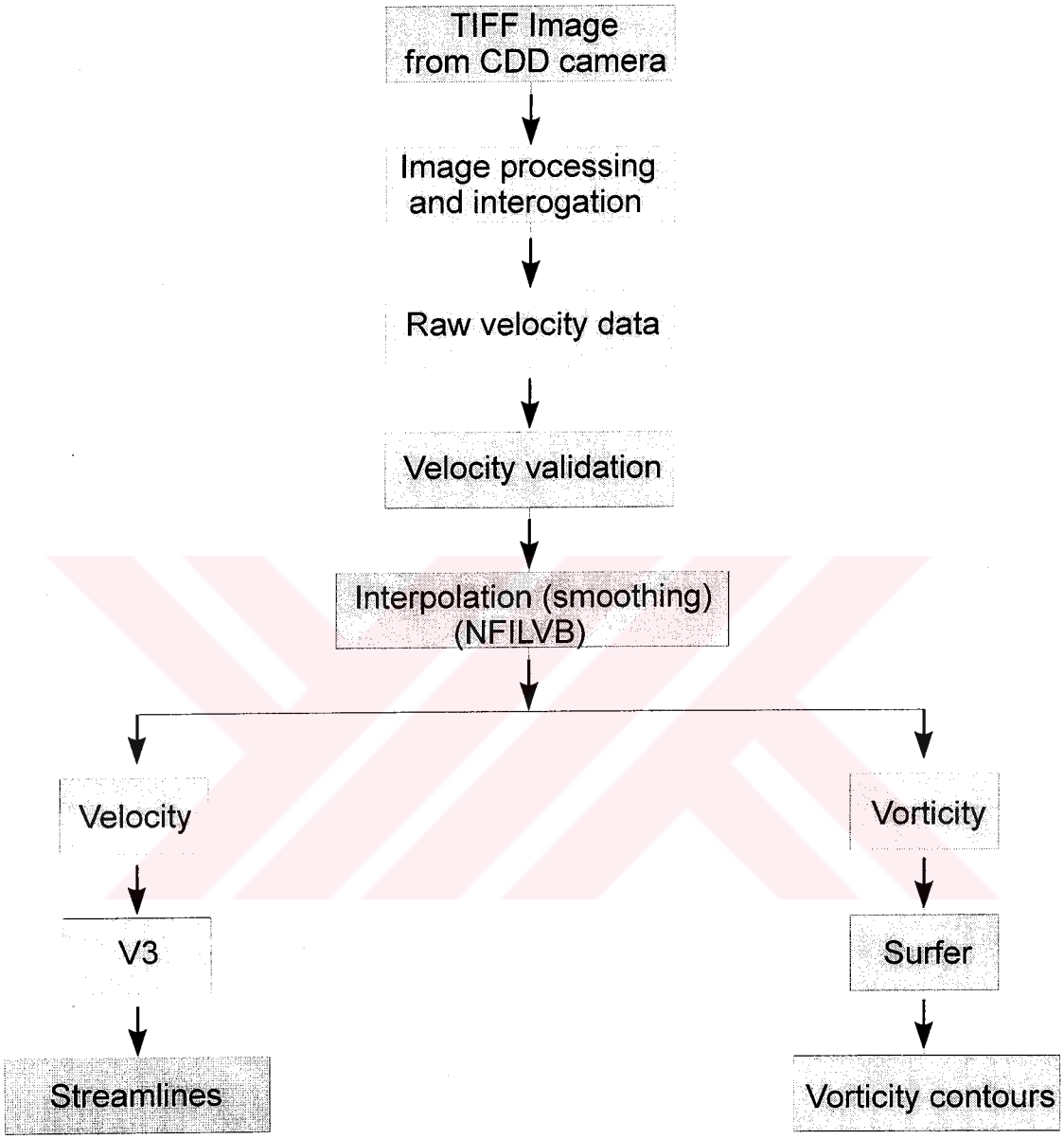

Figure 3.4.1. General procedure for image processing.

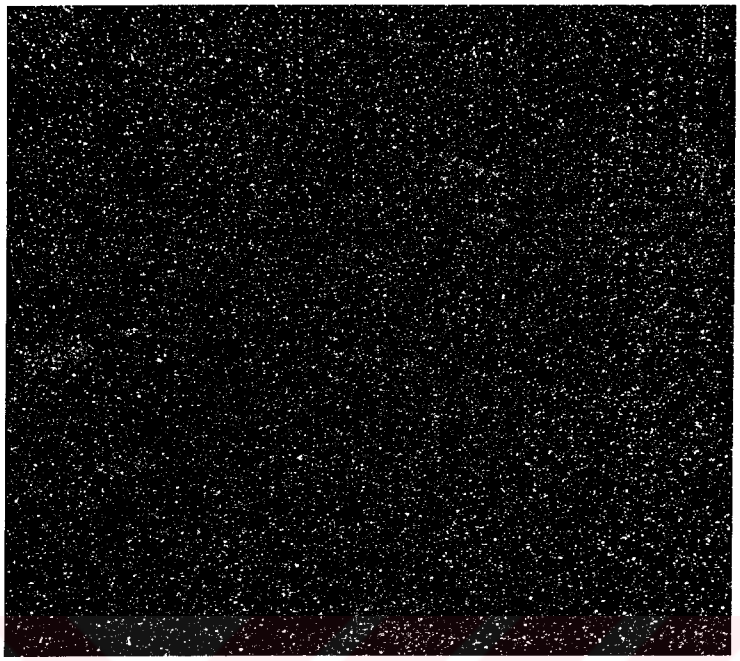

(a)

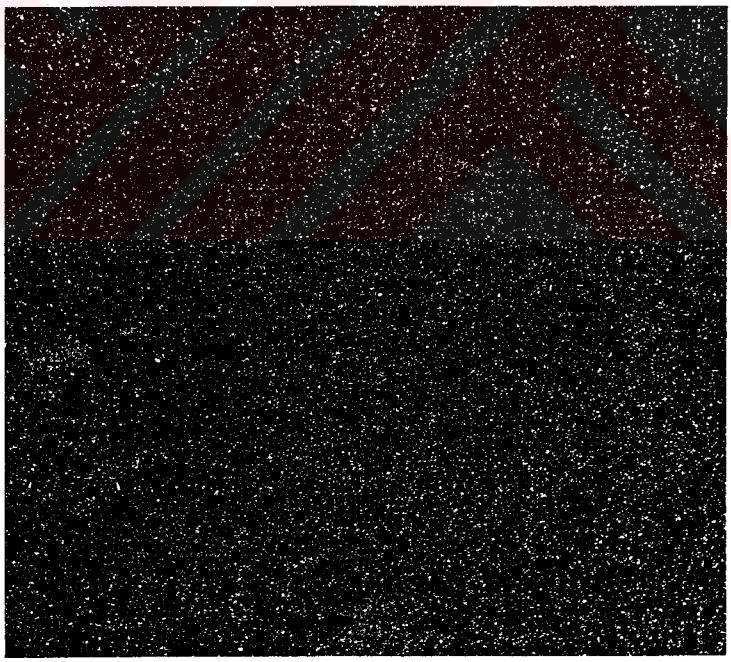

(b)

Figure 3.4.2. Excerpt from cinema sequence showing digital image file format (TIFF). Time interval between image (a) and (b) is 0.06 6sec.

correlated to produce an average particle displacement vector. The correlation method used in this study was given in Section 3.1.2. The overall field of view was 88.5 mm x 89.9 mm, and the total numbers of velocity vectors were 3,782. The interrogation window size was 1.4 mm by 1.4 mm in the plane of the laser sheet. The high-image-density criterion was well exceeded by ensuring that a minimum of 100 particles appeared within the interrogation window in a single frame.

The resulting vector field obtained from INSIGHT software and the corresponding boundaries of objects were then viewed using in-house program V3 (Robinson, 1992) to determine incorrect vectors from interrogation. These types of vectors can result when an incorrect particle correlation is made near boundaries or within shadow regions, when the particle images are too widely spaced for interrogation window side specified, or the power of laser sheet is poor (Jefferies, 1996 and Çetiner, 1998).

Vector validation software called CLEANVEC was used to remove incorrect vectors. This software is available from University of Illinois Urbana-Champign Laboratory of Turbulent and Complex Flows. The software CLEANVEC contains four statistical filters designed for incorrect vector removal:

- Absolute Range Filter
- RMS Tolerance Filter
- Magnitude Difference Filter
- Quality Filter.

Three of these four filters were used for the purposes of the eliminating incorrect vectors. Here, the Quality Filter requires a correlated data which are supposed to be done by interrogation program and this data was not provided by this software.

In the Absolute Range Filter, all u and v velocity components that lie outside of a given range were removed. With this filtering method, one can identify a moving reference frame in order to save real vectors that are numerically specified and eliminated incorrect vectors on the main frame. Although very trivial, this filter might be very useful in removing the most tedious incorrect vectors, and hence improves the performance of the other filtering tools.

The RMS Tolerance Filter removes incorrect vectors those lay outside of a given range. This filter must be applied to a velocity field in a reference frame moving with the mean velocity components in both directions, since it is involved with the fluctuating components only.

Finally, the Magnitude Difference tool removes unnecessary vectors based on the difference in magnitude between a vector and its neighborhood median. This is the local-median test defined by Westerweel (1994). This filter is the most effective among the available filters, as indicated by Westerweel (1994). However, it should be handled carefully, because it may lead to an excessive vector removal in a certain type of flows.

After the process of removing incorrect vectors, the in-house program NFILVB (Lin, 1994) interpolate between the vectors and the areas where incorrect vectors were removed using a bilinear least-square fit technique. And also, NFILVB utilizes the image magnification factor M in order to convert interrogated displacement to velocity magnitude on the scale of the actual flow field.

The interpolated and scaled velocity field was also smoothed by Gaussian weighted averaging technique based on the work of Landreth and Andrian (1989) in which a smoothing parameter of 1.3 was used.

Finally, the vorticity was calculated by circulation method. The velocity and vorticity data were set to zero in the region containing the bluff body following the smoothing process and vorticity calculation. The contours of constant vorticity were constructed using a spline fit technique with a tension factor of 0.1 for smoothing process. The sampled-averaged velocity field information was obtained using the in-house program NWENSAV2 (Lin, 1996) and, hence, patterns of mean-square velocity and vorticity fluctuations were also calculated.

3.4.1. Time-Averaging of PIV Images

Time-averaging of PIV images were performed using following formulation.

Time-averaged horizontal component of velocity:

$$\langle u \rangle = \frac{1}{N} \sum_{n=1}^{N} u_n(x,y) \tag{3.11}$$

Time-averaged transverse component of velocity:

$$\langle v \rangle = \frac{1}{N} \sum_{n=1}^{N} v_n(x,y) \tag{3.12}$$

Time-averaged vorticity:

$$\langle \omega \rangle = \frac{1}{N} \sum_{n=1}^{N} \omega_n(x,y) \tag{3.13}$$

Root-mean-square of u component fluctuation:

$$u_{rms} = \left\{ \frac{1}{N} \sum_{n=1}^{N} \left[u_n(x,y) - \langle u(x,y) \rangle \right]^2 \right\}^{1/2} \tag{3.14}$$

Root-mean-square of v component fluctuation:

$$v_{rms} = \left\{ \frac{1}{N} \sum_{n=1}^{N} \left[v_n(x,y) - \langle v(x,y) \rangle \right]^2 \right\}^{1/2} \tag{3.15}$$

Averaged value of Reynolds stress correlation:

$$\langle u'v' \rangle = \frac{1}{N} \sum_{n=1}^{N} \left[u_n(x,y) - \langle u(x,y) \rangle \right] \left[v_n(x,y) - \langle v(x,y) \rangle \right] \tag{3.16}$$

Where N is the total number of instantaneous images used for the time-averaged values and n refers to the instantaneous images.

3.4.2. Phase-Averaging of PIV Images

In addition to time-averaging, phase-averaging of images were pursued. The phase-reference to be employed depends on the type of experiment. In cases, where a periodic signal is recorded along with the PIV images, it is possible to employ this signal as phase-reference, provided that the timing of PIV images is known. In this study where such a signal is not available, it is necessary to make use of the PIV images themselves and search for characteristic motion representing the phase-oscillations.

The equations employed for phase-averaging are directly analogous to those employed for time-averaging, except the average was performed for the total number of M images at a given phase ϕ, as described in the foregoing.

Phase-averaged horizontal component of velocity:

$$\langle u \rangle_p = \frac{1}{M} \sum_{m=1}^{M} u_m(x,y) \tag{3.17}$$

Phase-averaged transverse component of velocity:

$$\langle v \rangle_p = \frac{1}{M} \sum_{m=1}^{M} v_m(x,y) \tag{3.18}$$

Phase-averaged transverse component of vorticity:

$$\langle \omega \rangle_p = \frac{1}{M} \sum_{m=1}^{M} \omega_m(x,y) \tag{3.19}$$

Where M is total number of instantaneous images used for the phase-averaged values and m refers to the instantaneous images.

4. RESULTS AND DISCUSSIONS

4.1. Vortex Formation from a Vertical Cylinder in Shallow Water Flow

4.1.1. Turbulent Boundary Layer

One of the characteristics of shallow water flows is that the turbulent boundary layer extends through the whole water depth. Therefore, in order to promote development of turbulence in the shallow layer, a trip was placed at the inlet of the test section. This trip consists of two cylinders of diameter 1.57 mm wound with a helical wire of diameter 0.90 mm. The pitch of the helical winding was 1.5 mm. The distance between two cylinders wound with a helical wire is 50.8 mm. After performing several preliminary experiments, this method of trip was found to be particularly effective in the development turbulence. For similar consideration, Balachandar et al. (2000) used a trip which was made of sand particles having diameter of 1.0 mm and glued on the bottom of channel as a 25 mm strip spanning the entire width of the flume. They located the trip 1.75 m upstream of bluff body.

A total of 136 PIV images were used to calculate the time-averaged velocity. The resultant distribution of time-averaged velocity at the location of the cylinder, but in its absence, agreed well with measurements of Kırkgöz and Ardıçlıoğlu (1997), Klebanoff (1955), excerpted from Schlichting (1979), Purtell et al. (1981) and Johansen and Smith (1983). These results are presented in Figure 4.1.1.

The values of displacement δ^* and momentum thickness θ of the boundary layer are calculated as 4.08 and 3.11 mm respectively which corresponds to the dimensionless values of $\delta^*/\delta=0.17$ and $\theta/\delta= 0.13$ respectively. Here, δ is the boundary layer thickness, defined by the location where $U=0.99U_{max}$. For the present study, the boundary layer shape factor $H= \delta^*/\theta$ is 1.31 which fits to the known value given in the open literatures as $1.2<H<1.4$ for turbulent flow. The Reynolds number based on momentum thickness was 550.2.

Present experiments are required to be carried out in fully developed flow region. So, initially a certain number of experiments were conducted to prove that fully developed flow exists in the test chamber. Time-averaged velocity results taken

from the literature shown in Figure 4.1.1, which are the local mean velocity distributions of fully developed deep and shallow open channel flows. As seen in Figure 4.1.1, the present PIV results are in well agreement with LDA measurements. From accuracy point of view this measurement of velocity distribution in fully developed turbulent boundary layer indicates that the PIV has a high rate of accuracy in velocity measurements.

Figure 4.1.2 shows the mean velocity distribution in inner region of turbulent boundary layer. The velocity distribution in the viscous sublayer admitted linear. In the fully turbulent boundary layer of inner region, the logarithmic velocity distribution of von Kármán (1930), Prandtl (1932), known as the law of the wall, is universally accepted formula,

$$\frac{u}{u_*} = A \ln \frac{u_* z}{\nu} + B \tag{4.1}$$

where $A = 1/\kappa$, κ is the von Kármán constant, B is a constant number. The value of B depends on the nature of the wall surface. u_* is the shear velocity. The von Kármán constant is 0.41 and the value of B is 5.5 for hydraulically smooth pipe flow and Keulegan (1938) assumed that the same value can be used for smooth open channel flow as well. Kırkgöz (1989) confirmed these results. However, various investigators have obtained different values for A and B. The value of A has a range of variation between 2.43 (Nezu and Rodi, 1986) and 2.5 (Steffler et al., 1985). The value of B has range between 4.9 (Klebanoff, 1955) and 7 (Townsend, 1956). In all of the law of the wall distributions, the experimental data fit a linear relationship in the viscous sublayer of developing and fully developed flow. When $\frac{u_* z}{\nu} \leq 10$ the velocity distribution can be presented as (Kırkgöz and Ardıçlıoğlu, 1997);

$$\frac{u}{u_*} = \frac{u_* z}{\nu} \tag{4.2}$$

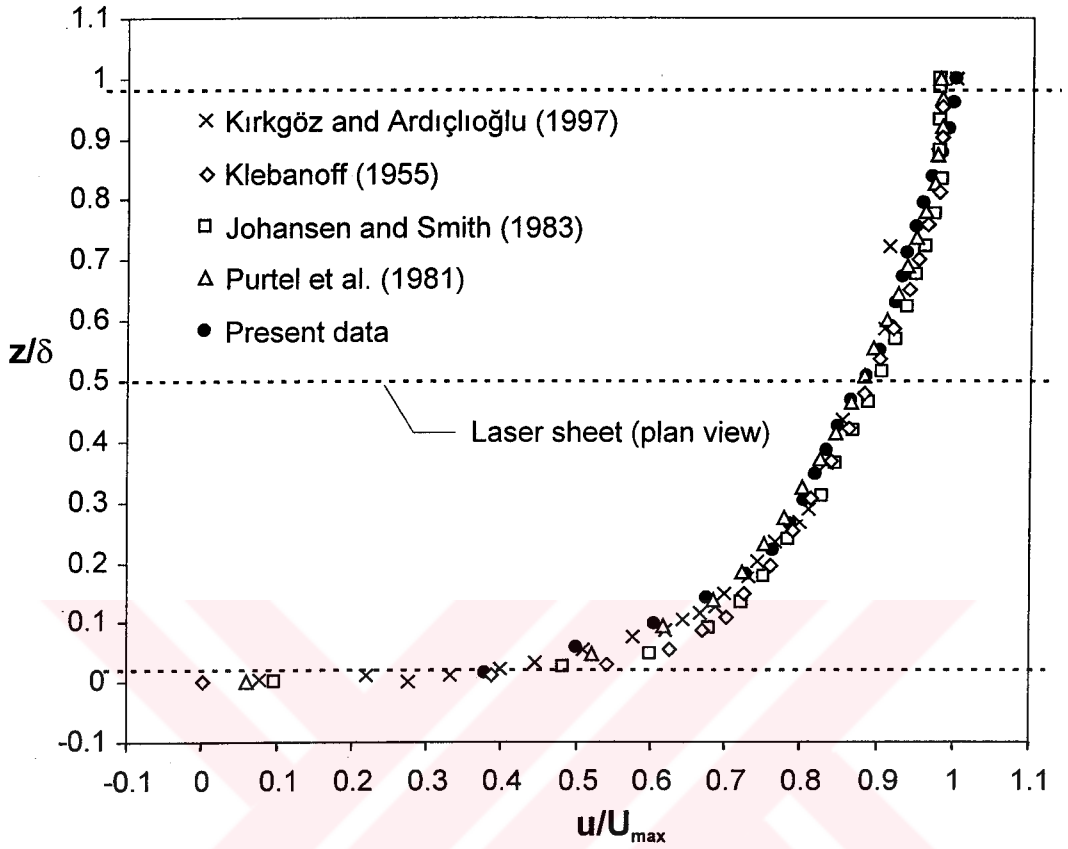

Figure 4.1.1. Velocity distributions for fully developed turbulent boundary layer.

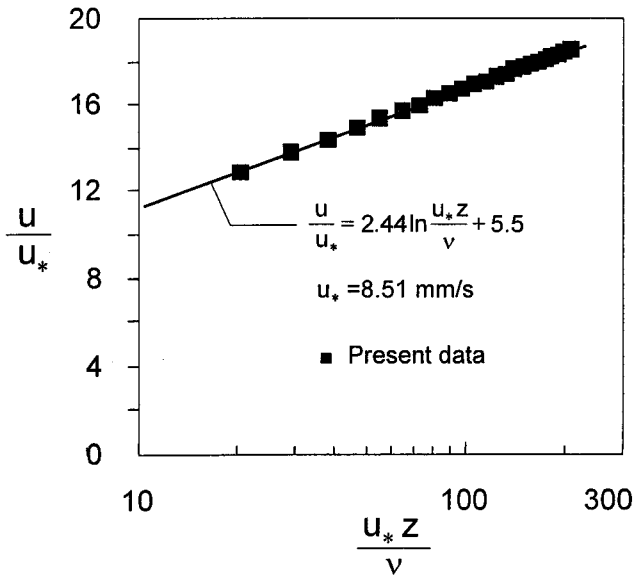

Figure 4.1.2. Mean velocity distributions in the inner region of turbulent boundary layer.

The experimental results of local mean velocity obtained in this study is agreed well with Equation 4.1.

It can be concluded that the presently used experimental technique which is Particle Image Velocimetry has a high accuracy for such kind of experiment. The water channel and the test chamber are well adjusted to have fully developed turbulent boundary layer.

4.1.2. Flow Structure Upstream of a Vertical Cylinder

The flow structure upstream of the vertical circular cylinder near the bed and midplane elevations, h_L/h_w=0.04 and 0.5, is presented in Figure 4.1.3 by patterns of averaged vorticity $<\omega>$, Reynolds stress $<u'v'>/U^2$, and streamlines $<\psi>$ topology. At both elevation, the patterns of vorticity are remarkably similar, whereas the Reynolds stress shows significant values only near the bed, apparently due to the fluctuations associated with the horseshoe (or necklace) vortex in that region. At the upper and lower right corners of the image (h_L/h_w=0.04), Reynolds stress patterns of opposite sign are evident. They are located exterior to the region of shear layer separation from the surface of the cylinder.

The pattern of streamlines near the bed shows a saddle point that is displaced upstream from the surface of the cylinder, again associated with the necklace vortex, whereas at the midplane, the pattern is representative of that of a quasi-two-dimensional flow.

All of the patterns in Figure 4.1.3 are due to formation of a necklace, or horseshoe, vortex that forms at the junction of the vertical cylinder with bottom surface (bed) of the shallow water layer. Seal et al. (1997) and Praisner et al. (2000) show different, complementary representations of the details of flow pattern over vertical, rather than horizontal, planes at the junction, i.e., vertical orientations of the laser sheet, and for a substantially deeper water layer, in comparison with the shallow water layer described herein. Their patterns are consistent with those shown in Figure 4.1.3. Both indicate separation of boundary layer upstream of the cylinder, which is associated with the onset of formation of the horseshoe vortex.

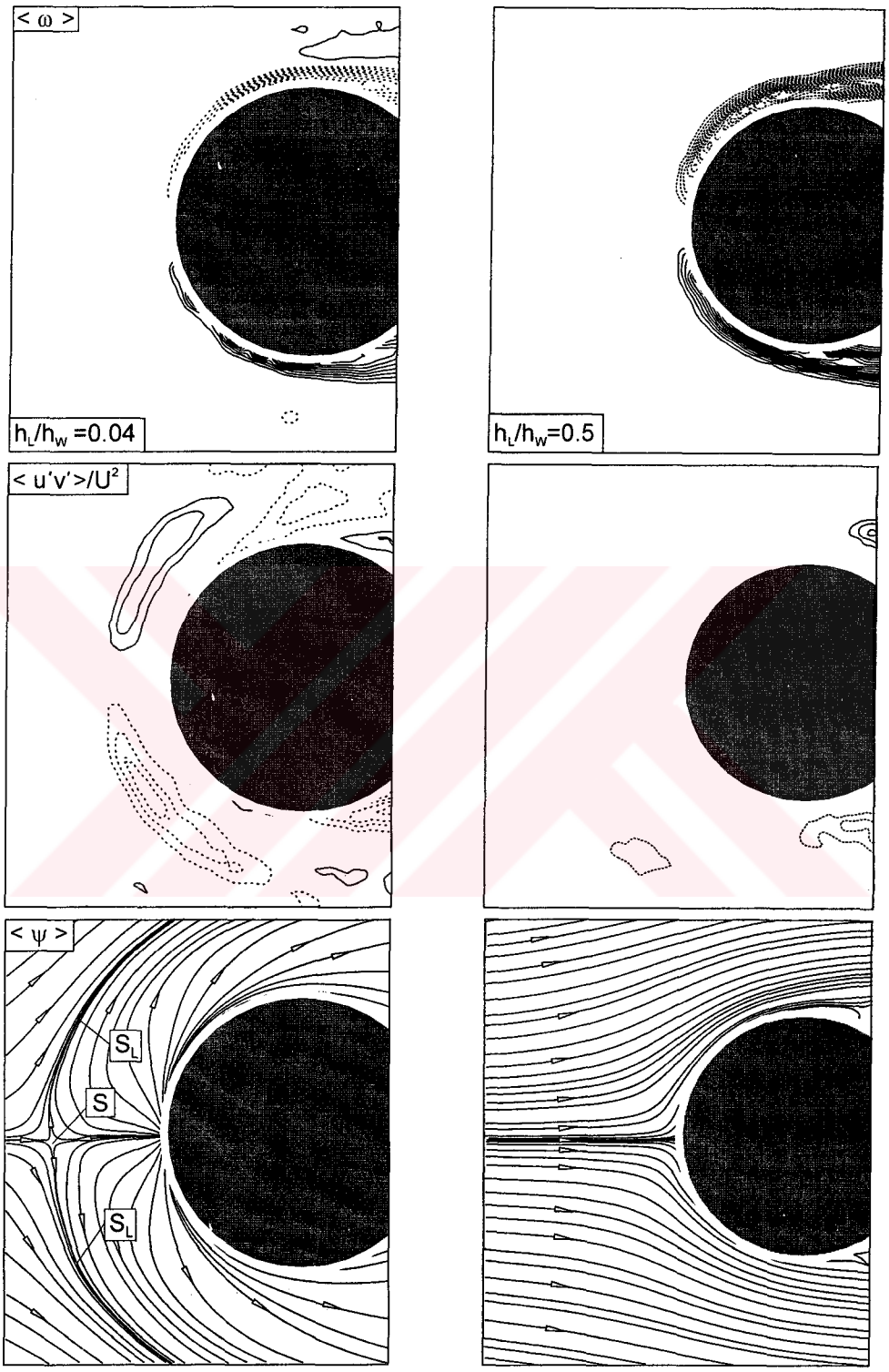

Figure 4.1.3. Time-averaged flow structure at the midplane h_L/h_w = 0.5 and near the bed h_L/h_w = 0.04 due to interaction of the inflow with the vertical cylinder. Patterns of time-averaged vorticity, Reynolds stress and streamlines are illustrated. Minimum and incremental values of vorticity are ω_{min} = ±6 sec^{-1} and = 4 sec^{-1}. Minimum and incremental values of normalized Reynolds stress are $[<u'v'>/U^2]_{min}$ = ± 0.005 and $\Delta[<u'v'>/U^2]$ = 0.005.

The incoming flow separates in front of the cylinder along a primary separation line (S_L) passing through the saddle point (S) indicated in Figure 4.1.3. But, an attachment node does not occur in front of the cylinder as it is described by Delery (2001). Flow between separation line (S_L) and surface of the cylinder rolls up to create horseshoe vortex surrounding the cylinder as shown in Figure 4.1.3. The saddle point (S) and separation line (S_L) moves further towards the cylinder when the midplane of the time-averaged flow structure moves further away from the surface of the bottom of the channel. For example, at the horizontal midplane of the flow structure the saddle point (S) and separation line (S_L) disappear completely in front of the cylinder as seen of the midplane h_L/h_w=0.5 image of Figure 4.1.3. Seal and Smith (1999) stated that the three-dimensional interaction of turbulent vortical structures exist in the vicinity of channel bed upstream of the cylinder when vortices move into closer proximity to the bottom surface of the channel, an interaction of the vortices with the surface fluid develops, culminating in the generation of focused, localized eruptions of surface fluid.

4.1.3. Visualized Flow Structure in Shallow Water Layer

To gain further detail of the process of vortex formation between the bottom surface of the channel and the free-surface, dye visualization was used. The sketch in Figure 4.1.4 shows the flow organization on the bed surface. Side views of patterns of three-dimensional vortex formation in the near-wake region demonstrated in Figure 4.1.4a for the value of dimensionless water depth h_w/D=0.5. Here, the schematic plane view of Figure 4.1.4c shows the location of dye injection, which was in the vicinity of the base of the cylinder. Through eye observation, it was observed that dye rapidly spreaded along the bottom surface of the test section and a vortex formed as seen in Figure 4.1.4a. The surface fluid at the base of the cylinder illustrates that the rapid development of eruptions create counterclockwise vortices in close proximity to the surface. There is a strong vortex-surface fluid interaction process. Similar flow characteristics in the base of the cylinder are also obtained by a measurement PIV shown in Figure 4.1.4b. Side-view visualization of horizontal

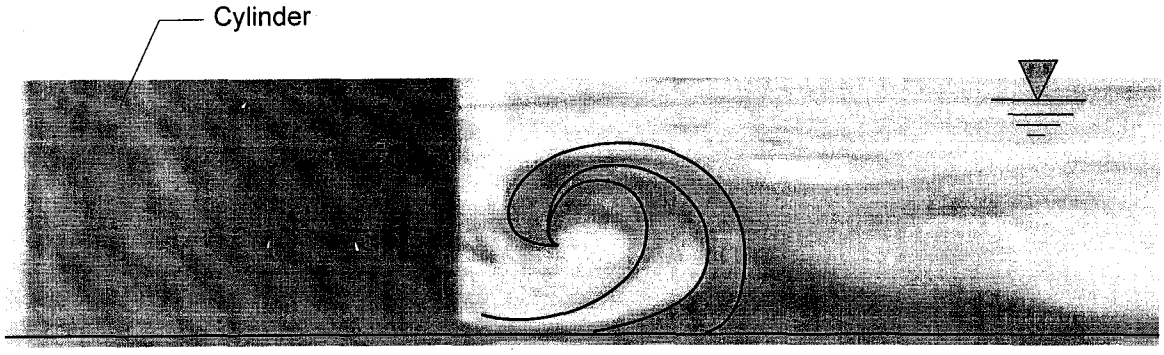

(a)

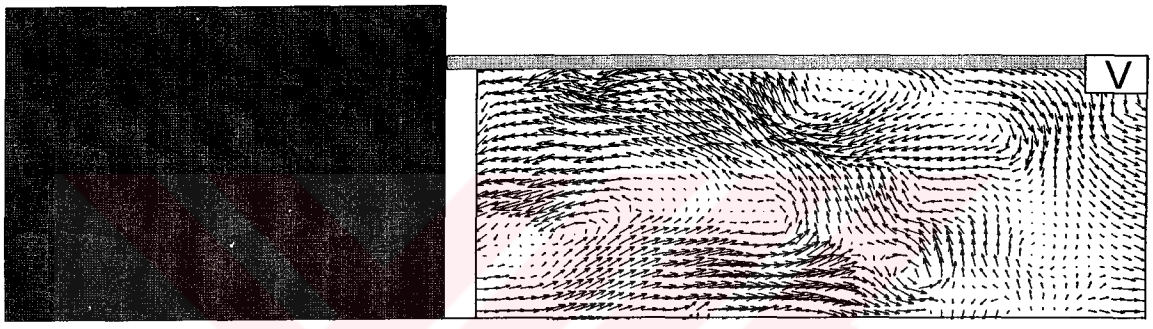

(b)

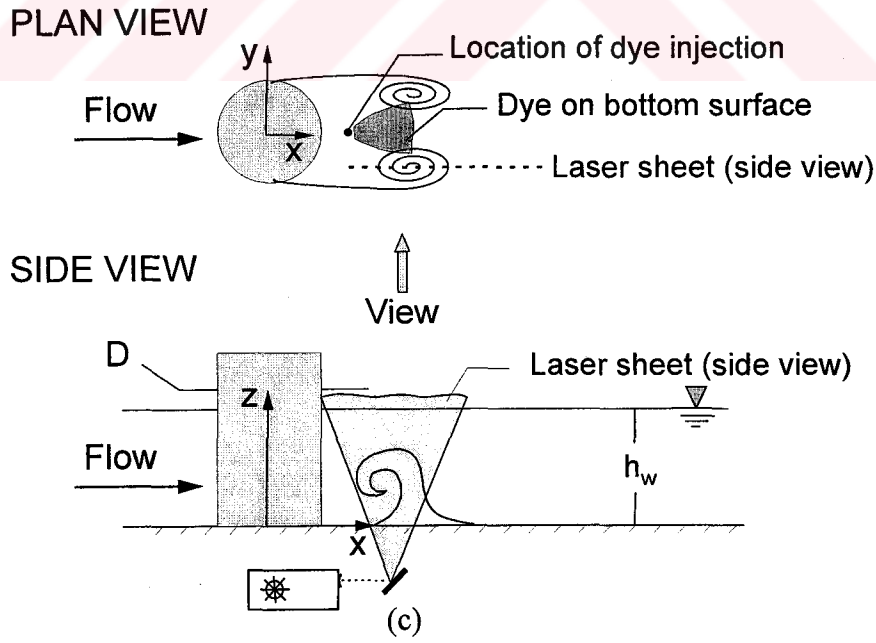

(c)

Figure 4.1.4. Side views of patterns of three-dimensional vortex formation in the near-wake region, which are obtained by spreading visualization marker on the bed (bottom surface) and instantaneous velocity vectors.

vortices indicates that injected dye from the bed rolls up towards the cylinder in three-dimensional manner. This horizontally oriented vortex eventually grows and becomes relatively close the free-surface.

Finally, this vortex moves away in the direction of mean flow. The visualization shown in the work of Seal and Smith (1999) demonstrate how turbulent-like eruptive behavior can result from the three-dimensional interaction and deformation of intertwining vortices, suggesting a possible mechanism for similar behavior in fully turbulent flow. Vortex deformation and interaction may play a role in the process of turbulence regeneration.

4.1.4. Time-averaged Flow Structure

4.1.4.1. Averaged surface topology near the bed

Time-averaged velocity field obtained by averaging instantaneous images of velocity and the corresponding time-averaged patterns of streamline topology are presented in top image (i) of Figure 4.1.5. As indicated, two saddle points designated as S_1 and S_2, and as well as two foci, F_1 and F_2, are evident. Separation line S_L runs through the saddle point S_2.

Perry and Chong (1986) calculated the three-dimensional patterns for laminar separation bubbles on missile shaped bodies inclined at angle-of attack. This exterior flow is distinctly different from the present case of the near-wake of the cylinder. In the present shallow water flow, there is strong reverse flow along its axis of symmetries at all elevations above the bottom surface as shown in image (iv) of Figure 4.1.5. As seen in Figure 4.1.5, the surface topologies of Perry and Chong (1986) is extremely similar to the present topology. The magnitudes of the vectors exterior to the bubble-like region that the saddle points S_1 and S_2 as well as foci F_1 and F_2 are substantially larger than those within the bubble obtained by Perry and Chong (1986). Significant reverse velocities in the backward direction occur in the region between the saddle points S_1 and S_2. The averaged streamline pattern on a vertical plane that approximately intersects the focus F_1 and F_2 is parallel to the plane of symmetry of the cylinder is shown in the image (iv) of Figure 4.1.5. This

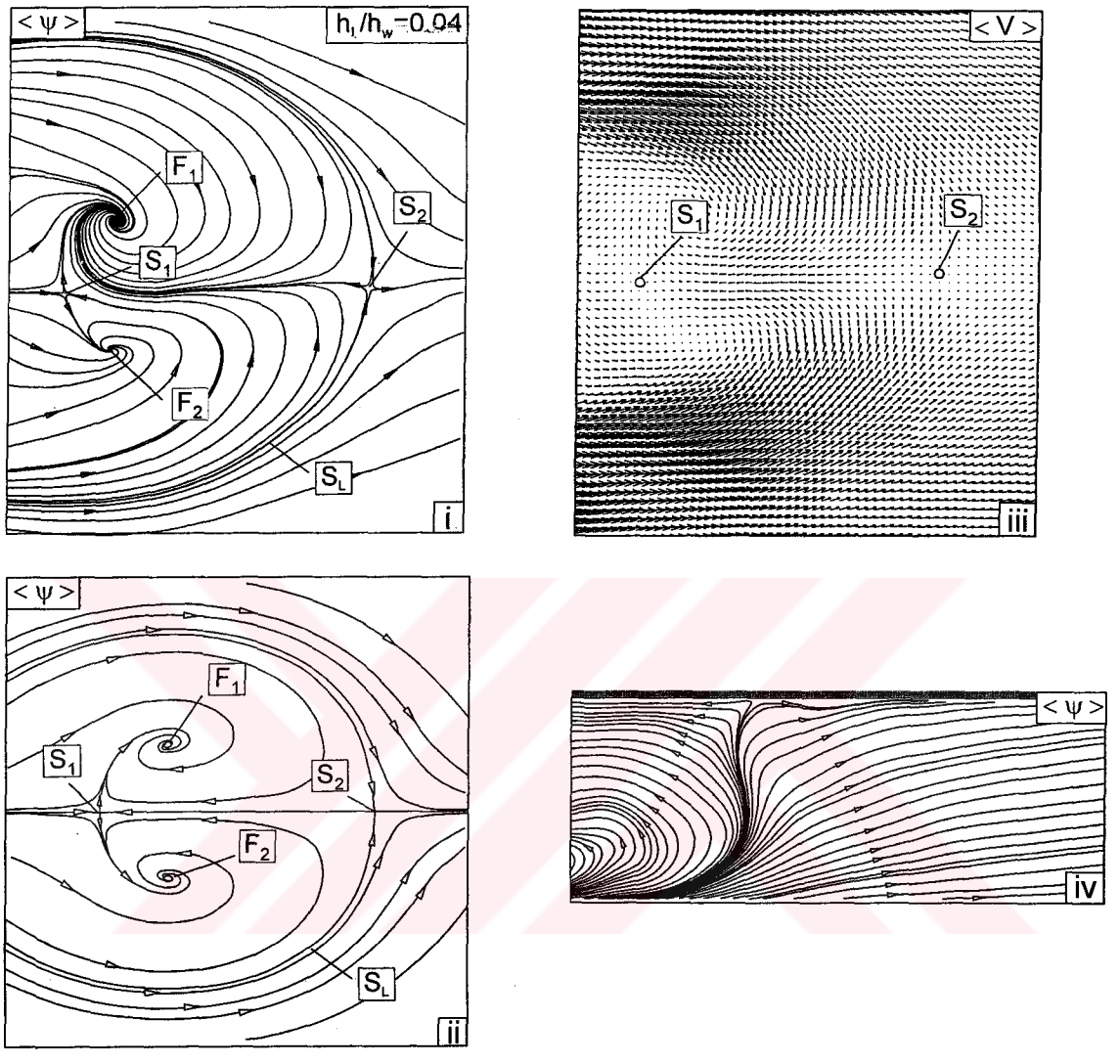

Figure 4.1.5. Time-averaged patterns at the bed surface represented by: (i) averaged streamline pattern of present investigation; and (ii) calculated pattern for laminar separation bubble (Perry and Chong, 1986); (iii) averaged velocity field near the bed of present investigation; (iv) the time-averaged streamline pattern in a vertical plane passing through the center of the foci F_2 of the surface topology of the present investigation.

streamline pattern indicates that a strong reversing motion of fluid causes spanwise vortex formation expanded between bed surface and free-surface, which is compatible with the dye visualization of Figure 4.1.4.

4.1.4.2. Averaged topology as a function of elevation above the bed

The flow projected in different plan views reveals as general wake-flow behaviour. Averaged topology as a function of elevation above the bed surface in terms of patterns of time-averaged streamline in close region of the bed, midplane and free-surface elevations are shown in Figure 4.1.6. Two main vortices are formed by rolling up of the separated flow region emanating from the separation line. The topological interpretation given in image of Figure 4.1.6 is duplicated since the topological features very close to the base of the cylinder reveals that a nodal pattern of streamlines centered at the plane of symmetry formed in the vicinity of the bed surface at h_L/h_W=0.04 presented in Figure 4.1.6. This nodal pattern happen in between three saddle points. Whereas, at the midplane and free-surface elevation i.e. h_L/h_W=0.5 and 0.94 highly ordered nodes and saddle points along the base of the cylinder do not occur. In general, a separated region exists behind the cylinder with separation surfaces starting from each side of the cylinder, causing two foci F_1 and F_2 behind the cylinder and over the entire plane of the image, only one clearly-defined saddle point occurs. This saddle point corresponds to S_2 defined in Figure 4.1.5. The foci associated with outward-spiraling streamlines are unstable. The size of the separation bubbles is bigger above the bed surface elevation comparing to the next elevation.

Tachie et al. (2000) introduced that surface roughness is not only widely encountered in industrial flow applications such as flow over turbine blades or flow through duct systems, but it becomes critically important in environmental flows, where surface roughness is dominant. For this reason, the friction characteristics of boundary layers have been taken the attentions of researchers extensively in past years. Ingram and Chu (1987) pointed out that the stability of the wake bubble depends on the stability of the shear layers along the two sides of the wake bubble.

The shear layer is stable at a low Reynolds number of about 10. As Reynolds number increases, the shear layers become less stable, and oscillation begins. The interaction of the two unstable shear layers is the cause of the formation of the well-known Kármán vortex street. In conclusion, the oscillation is the result of active interaction between the shear layers developed along the two sides of the wake bubble. The oscillation of the wake bubble is suppressed if the shear layers are stabilized by bottom friction. The present results shown in Figure 4.1.6 indicate that the average flow characteristics are the function of the elevation above the bed surface. The separating streamline, which is the boundary between trough-flow and the wake flow region, is clearly seen from the distribution of streamlines. The boundary between wake and core flow region is of intense shear. Flow is entrained into the edge of the wake in the mixing region giving rise to a circulatory motion with the separated flow.

4.1.4.3. Averaged vorticity and Reynolds stress at various elevation above the bed

Averaged vorticity and Reynolds stress a various elevations starting in close region of the bed surface are shown in Figure 4.1.7. Concerning contours of constant vorticity at the elevation h_L/h_W=0.04, the transverse spatial extent of each layer remains relatively narrow, and it is rapidly drawn to the plane of symmetry of the base region. On the other hand, at midplane elevation h_L/h_W=0.5 and free-surface h_L/h_W=0.94 each layer is widely distributed in the lateral direction and also the central region of each layer is not deflected towards the plane of symmetry. Primary vortices with an opposite sign occupy a symmetrical position as shown in the plane view images of Figure 4.1.7. A similar type of information was revealed by Akıllı and Rockwell (2002) through their shallow water experiment of similar type. It is clearly defined at midplane and free-surface elevation a secondary separation occurs leading to a pairs of secondary vortices. Delery (2001) states that it is often difficult to obtain a clear visualization of the secondary vortices and their swirl velocity is much smaller than that of the primary vortices.

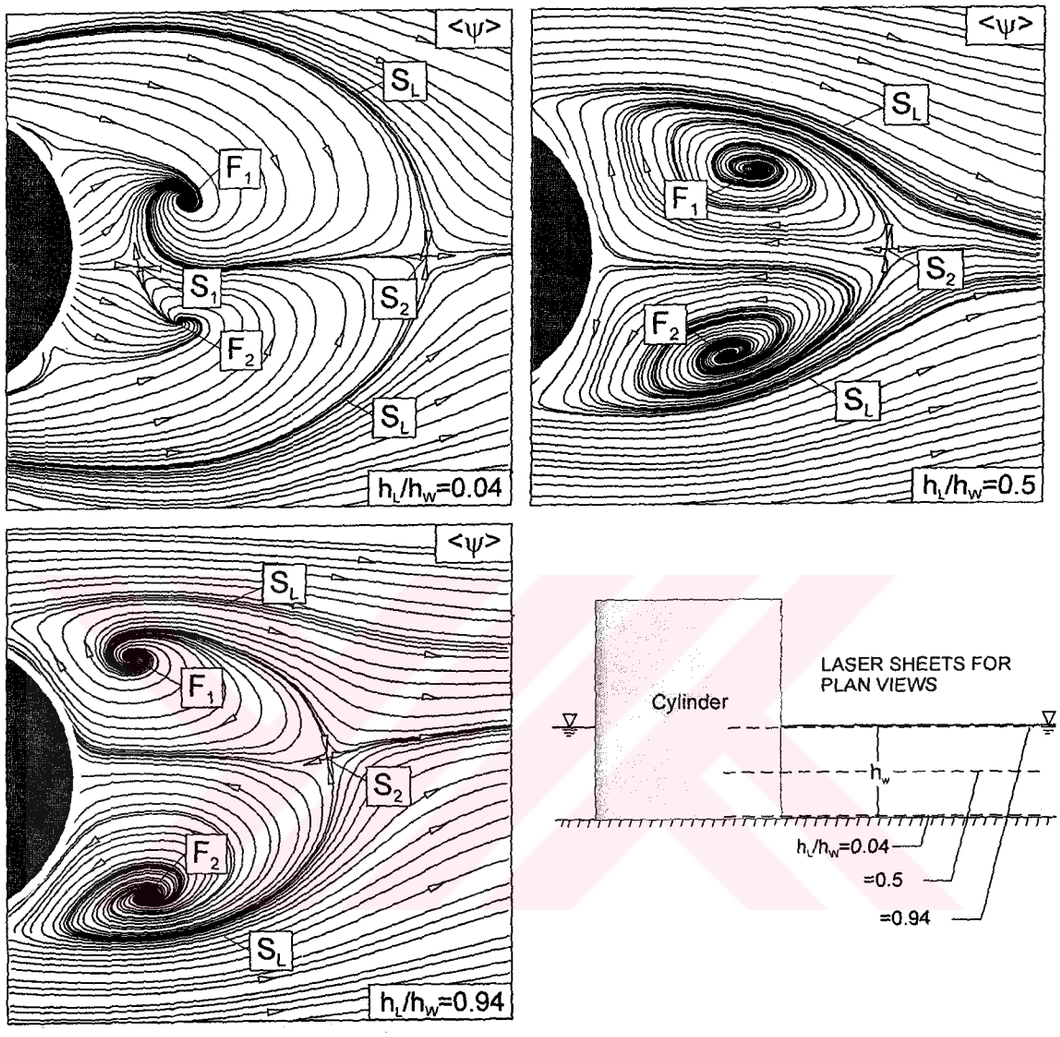

Figure 4.1.6. Comparison of time-averaged streamlines topology near the bed, midplane and free-surface elevations.

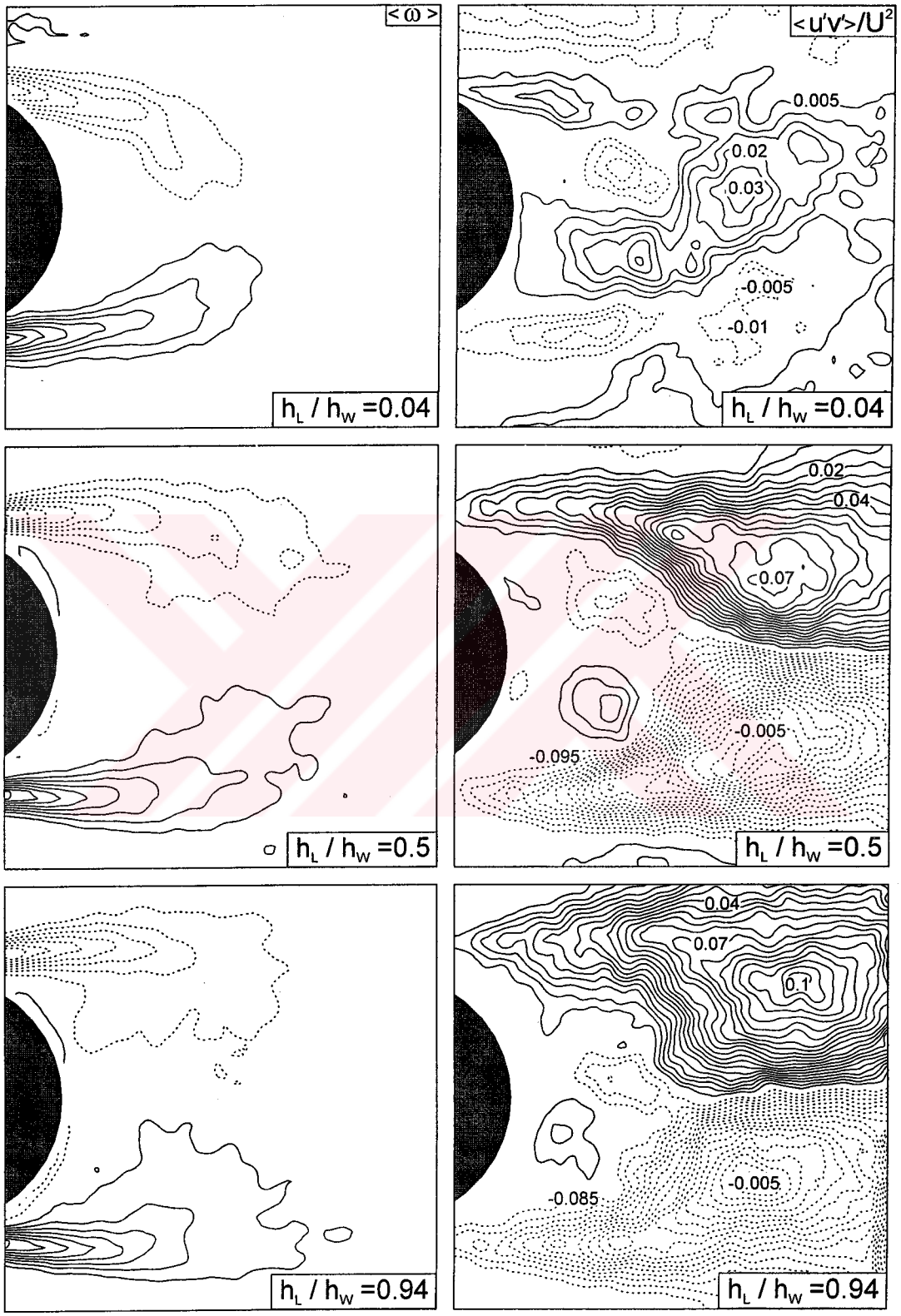

Figure 4.1.7. Comparison of time-averaged vorticity and Reynolds stress near the bed, midplane and free-surface layers. Minimum and incremental values of vorticity are $\omega_{min} = \pm 5\ sec^{-1}$ and $\Delta\omega = 5\ sec^{-1}$. Minimum and incremental values of normalized Reynolds stress are $[\langle u'v' \rangle / U^2]_{min} = \pm 0.005$ and $\Delta[\langle u'v' \rangle / U^2] = 0.005$.

Concerning the patterns of Reynolds stress shown in the right column of Figure 4.1.7., high concentrations are centered at a distance of approximately one cylinder diameter D downstream of the base of the cylinder. More explicitly, the centers of these concentrations occur at 0.91, 1.04 and 1.14 D for elevation corresponding to the near bed, midplane and free-surface respectively. The Reynolds stress pattern obtained at the midplane is more and less similar to that occurring in the free-surface elevation. Also, these overall from the Reynolds stress pattern at the midplane and free-surface are remarkably similar to that occurring in the near wake of a cylinder of larger spanwise extent, as determined experimentally by Lin et al. (2002), as well as calculated by Mittal and Balachandar (1995). The peak values of this dimensionless Reynolds stress $\langle u'v' \rangle / U^2$ are 0.03, 0.097 and 0.107 for the near bed, midplane and free-surface elevations respectively.

Finally, a distinguishing feature of the Reynolds stress pattern near the bed is the occurrence of additional concentrations exterior to the near-wake regions. This is due to the fluctuation associated with the necklace, or horseshoe vortex initially formed around the leading portion of the cylinder.

The transverse development of the turbulent mixing layers in an open channel flow of shallow water depth was investigated by Chu and Babarutsi (1988). They reported that turbulence in the shallow mixing layer may be considered to have two components with two distinct length scales. One is the small-scale turbulence, which is generated by the bed friction and limited in the length scale by the water depth. The other is the large-scale turbulence, which is generated by the transverse shear and characterized by a length scale comparable with the width of the mixing layer. The bed friction generates not only the small-scale turbulence but, at the same time, exerts a stabilizing influence on the large-scale turbulence. This bottom induced turbulence is mainly responsible for the vertical transports of momentum.

Contours of constant vorticity shown in first column of Figure 4.1.7 have the same magnitude near the bed, midplane and free-surface layers. But the area of circulation increases in the upper direction as a function of elevation. Tachie and Balachandar (2001) discussed that the transverse shear tends to destabilize the flow, while the bed friction has a stabilizing effect on the development of the wake. Thus

the extent of the spread of the wake depends on the relative magnitudes of the transverse shear and bed friction effects. If the bed friction effect becomes stronger in comparison to the transverse shear, the wake is stabilized and its lateral extent is limited. This flow phenomenon exists near the bed elevation. The weaker Reynolds stress occurs at this section as seen in top image of Figure 4.1.7. Hence, one would expect a higher ratio of transverse shear to bed friction effect to give a higher wake spread rate. Related to this discussion, the present study indicates that the width of the wake increases with the vertical direction. Concerning the distributions of Reynolds stress a stronger concentrations occur at the free-surface elevation, but weaker, concentration occur closer to the base of the cylinder. Higher values of Reynolds stress occur along the separation lines on both side of the cylinder having the peak values in close of the downstream of saddle point.

4.1.4.4. Patterns of velocity fluctuations as a function of elevation above the bed

Distribution of velocity fluctuations as a function of elevation above the bed surface, which are contours of constant root-mean-square streamwise velocity u_{rms} and transverse velocity v_{rms} are presented in Figure 4.1.8. An image of plane view in close region of the bed surface shows that the extrema of u_{rms} and v_{rms} are located relatively close the base of the cylinder. On the other hand, at the other two elevations, the extrema of u_{rms} and v_{rms} are displaced to a larger distance from the base of cylinder. The peak values of u_{rms}/U are 0.29, 0.41 and 0.43 which occur near the bed, midplane and free-surface elevations. The peak values of v_{rms}/U are 0.39, 0,50 and 0.49 which occur near the bed, midplane and free-surface. These root-mean-square values of transverse velocity fluctuation v_{rms} and streamwise velocity fluctuation u_{rms} are normalized by the free-stream velocity. The dominant feature of the flow inside the bubble envelope and in the wake region is v_{rms} fluctuations. The amplitude of v_{rms} fluctuations is the greatest at the midplane, h_L/h_W=0.5, and free-surface, h_L/h_W=0.94, elevations.

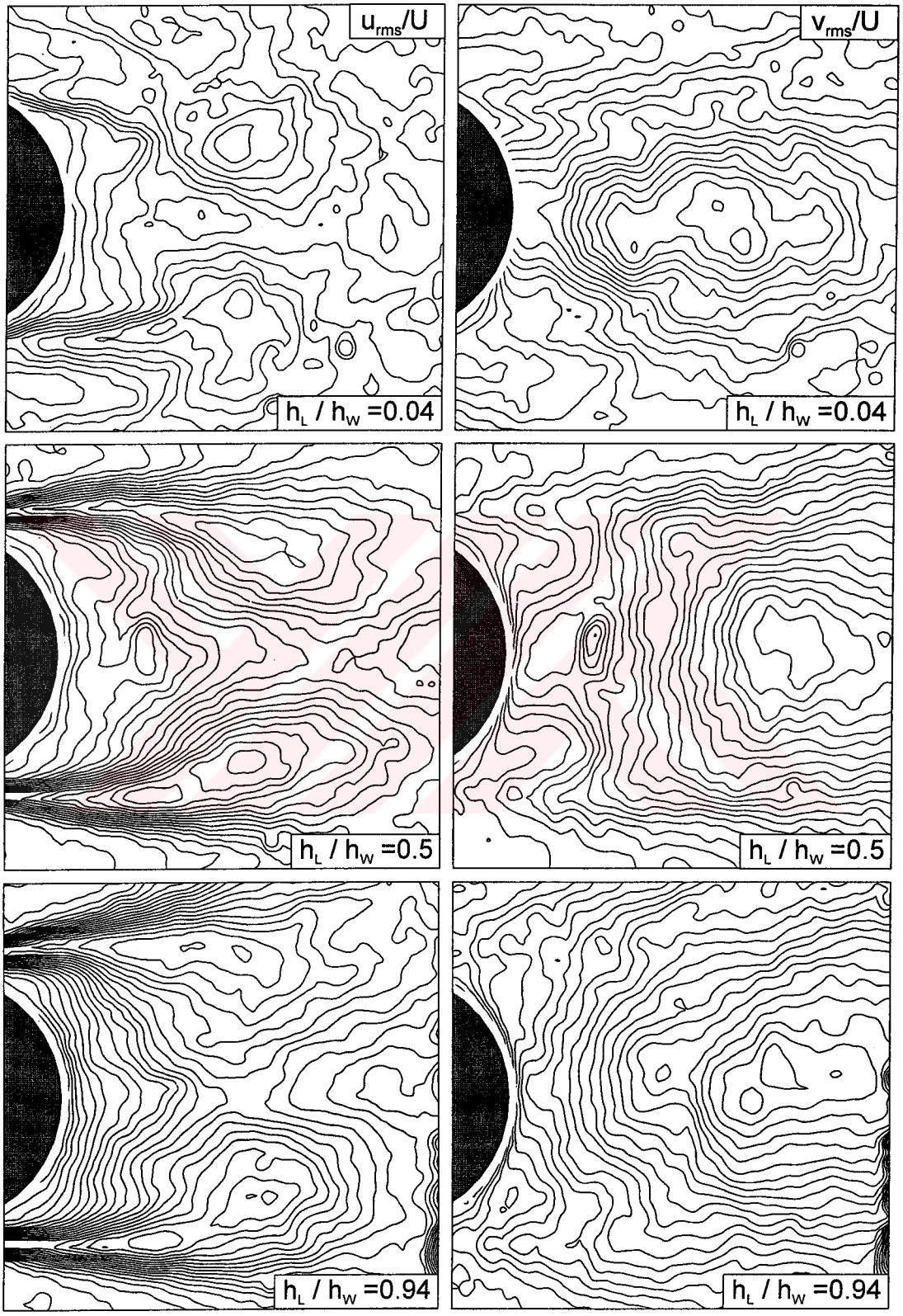

Figure 4.1.8. Comparison of root-mean-square velocity fluctuation near the bed, midplane and free-surface elevations. Minimum and incremental values of normalized rms values of streamwise u_{rms} and transverse v_{rms} velocity fluctuations are $[u_{rms}/U]_{min} = [v_{rms}/U]_{min} = 0.02$ and $\Delta[u_{rms}/U] = \Delta[v_{rms}/U] = 0.02$.

4.1.5. Phase-Averaged Flow Structure

4.1.5.1. Variation of patterns of flow structures near the bed during an oscillation cycle

The time history of development of the flow structure at a given elevation above the bed was determined from the sequence of instantaneous images of velocity, as described in Section of Material and Method. Construction of instantaneous streamline patterns allows identification of those images that occurred at the same phase of the vortex shedding cycle, according to the location of crucial saddle point relative to the base of the cylinder. Then, a total of four instantaneous images with coincident saddle points were averaged to produce a phase-averaged representation of the streamline topology. In addition, the averaged patterns of vorticity were determined at the same phases of the cycle of vortex shedding. As a result, at each selected phase of the oscillation cycle, both the streamline topology and the corresponding patterns of vorticity were available.

Figure 4.1.9a shows the near-wake development at an elevation immediately above the bed, h_L/h_w=0.04, for successive phases of the oscillation cycle, which are represented by five values of t/T, where T is the period of one complete cycle of Kármán vortex formation. This natural frequency of Kármán vortex formation was determined by an eye observation using chronometer. The value of T was measured as 1.6 sec . The value of Strouhal number $St = fD/\overline{U}$ is 0.194 in which $\overline{U}$ is the depth-averaged velocity, D is diameter of cylinder and f is frequency of Kármán vortex formation. Consider, first of all, the patterns of streamline topology shown in the right-hand column of Figure 4.1.9a. Each image shows an identifiable focus, which corresponds to the center of the spiraling streamline pattern. A further feature of the streamline topology in image of Figure 4.1.9a is the existence of a well-defined saddle point. The combination of this saddle point and spiral-like streamline pattern that leads to a limit cycle streamline is particularly evident in the images at t/T=0 and 0.54. Similar experimental work were also performed by Akıllı and Rockwell (2002). Pattern of phase-averaged vorticity and streamline topology reveal

that cluster of vorticity moves forward and backward in horizontal measuring planes. As a matter of simplicity, consider the top part of paper is forward and the bottom side backward. In this sense, when the cluster of vorticity moves downward as seen in top two images of Figure 4.1.9a, the saddle point occurs below the cluster of vorticity. This is indicated in terms of streamline topology. On the other hand, patterns of positive phase-averaged vorticity are elongated further downstream comparing to the patterns of negative phase-averaged vorticity. When the cluster vorticity moves upward, the saddle point occurs above this concentration of vorticity. This time, pattern of negative phased-averaged vorticity that appears above the cylinder elongates further downstream in the direction of the main flow.

Corresponding patterns of vorticity are shown in the left-hand column of Figure 4.1.9a. Positive (solid line) and negative (dash line) contours are indicated in relation to the saddle point S, which is extracted from the corresponding streamline topology, and shown schematically on each vorticity pattern. Consider the patterns of vorticity and saddle point locations to the top and bottom images of Figure 4.1.9a, i.e., t/T=0 and t/T=0.54. The saddle point S occurs at the location where the vorticity layer is pinched off by protrusion of the opposite layer that extends across the wake, yielding formation of a large-scale cluster of vorticity on the right-hand side of each image. Furthermore, the focus of the spiral pattern, in each images at t/T=0 and 0.54, is approximately at the extremum of the vorticity layer that extends across the near-wake, and has not yet detached to form an isolated concentration of vorticity.

All vorticity images of Figure 4.1.9a, i.e., t/T=0.18 and 0.36, show that the saddle point is again located at a position where contours of constant positive and negative vorticity layers from opposite sides of the wake are in close proximity to one another. Whereas the focus of the streamline pattern at t/T=0.18 is coincident with the extremum of vorticity in the upper layer at t/T=0.18, and likewise for lower vorticity layer at t/T=0.36, the streamline topology shows no well-defined spiral pattern corresponding to the vorticity extremum of the upper layer at t/T=0.36.

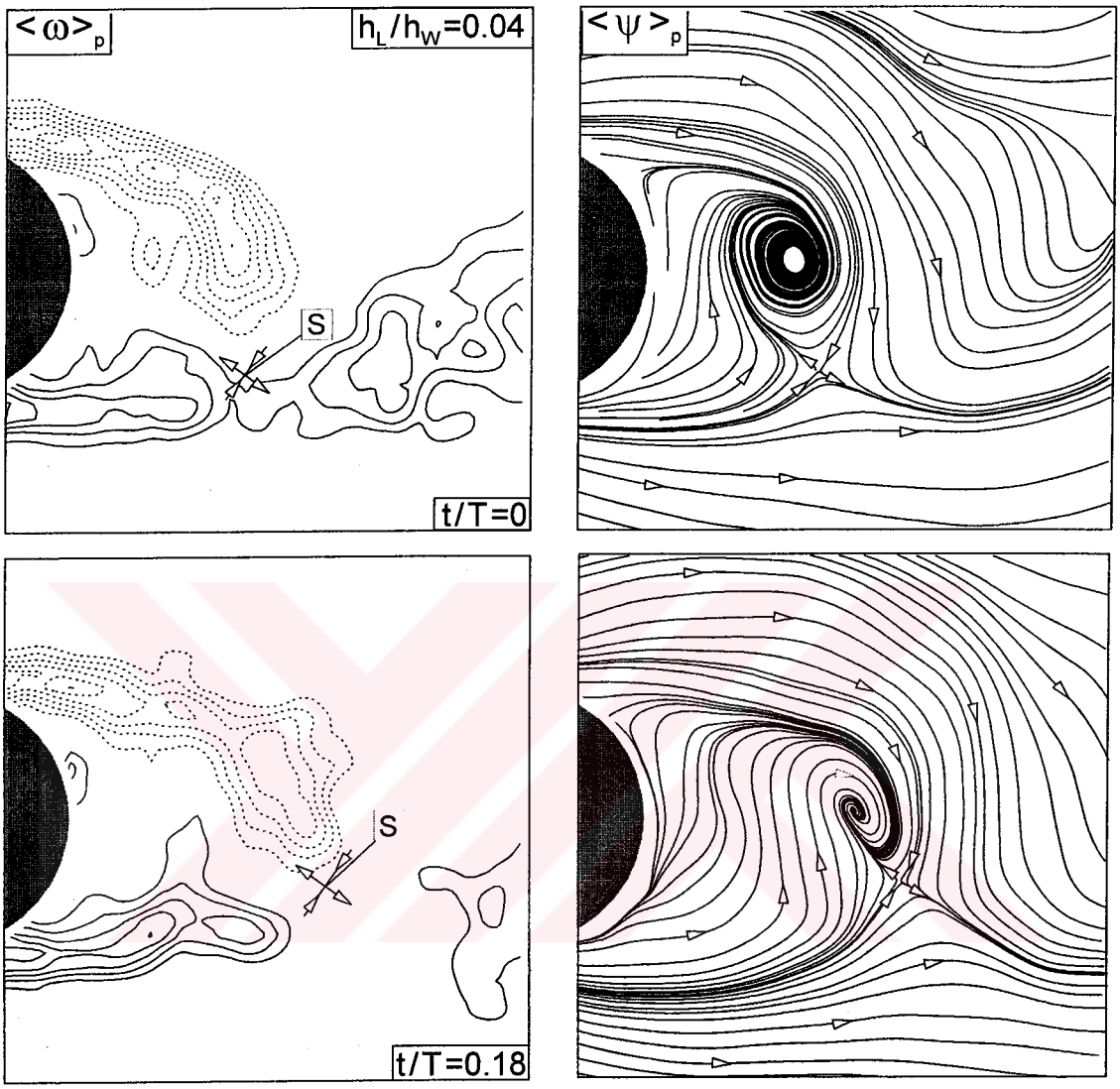

Figure 4.1.9a. Patterns of phase-averaged vorticity and streamline topology at sequential phases of the oscillation cycle, represented by increasing values of time t normalized by the period T of the Karman vortex formation. Minimum and incremental values of vorticity are $\omega_{min} = \pm 6\ sec^{-1}$ and $\Delta\omega = 4\ sec^{-1}$.

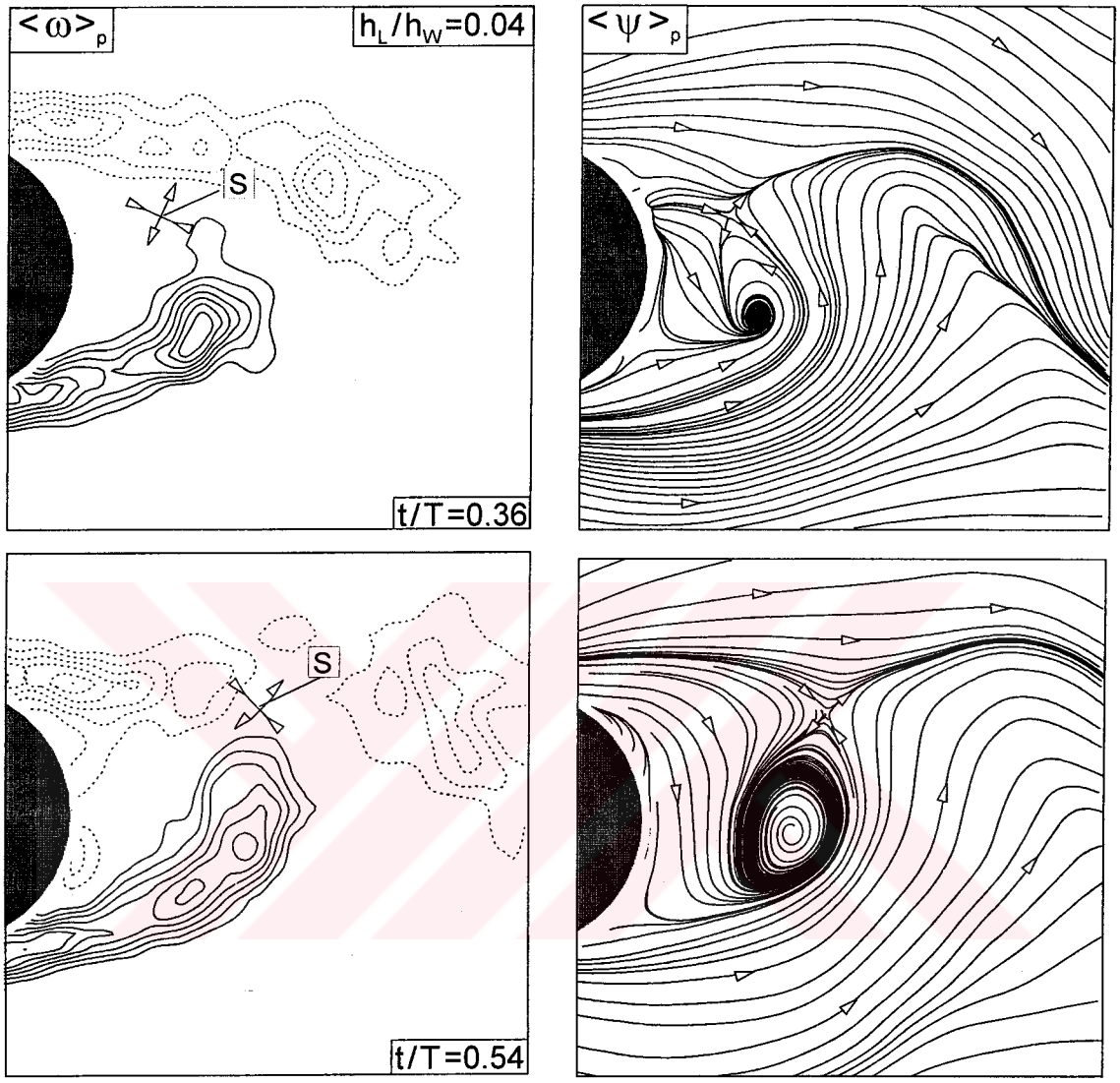

Figure 4.1.9a. Continued.

4.1.5.2. Comparison of flow structure as a function of elevation above the bed

Figures 4.1.9b and 9c show synchronized patterns of streamline topology at various elevations above the bed, along with corresponding patterns of vorticity. The criterion for phase-referencing (synchronization) at different elevations was a specified location of the saddle point in the near-wake region. Each of the images of Figure 4.1.9b was selected from a time sequence of images using this criterion. Simultaneous consideration of patterns of vorticity showed that the selected location of the saddle point corresponded to; (i) deflection of shear layer (from the opposite side of the cylinder) to its extreme position toward the centerline of the wake, and (ii) occurrence of a fully evolved, large-scale concentration of vorticity nearly coincident with the centerline of the wake. Despite the three-dimensionally of the near-wake , these features persisted for the same location of the saddle point at all elevations.

A consistent feature of the streamline topologies in Figure 4.19b and 9c is the spatial extent of the central portion of the spiraling streamline pattern. Near the bed, h_L/h_w=0.04, the central portion of the spiral pattern is of relatively small spatial extent, at the midplane, h_L/h_w=0.5, it extends over a somewhat larger spatial domain, and at the free-surface, h_L/h_w=0.94, it extends over a relatively large domain in the near-wake.

The issue arises as to the relationship between the streamline topologies described in the foregoing and the corresponding patterns of vorticity in the near-wake. The vorticity patterns of Figure 4.1.9b and 9c show the following features. Consider the vorticity layer that culminates in a definable, but not separate, agglomeration of vorticity. It is located at essentially the same spatial position as the focus (center) of each of the major spiral patterns of the streamline topology. In Figure 4.1.9b, the vorticity layer that leads to this region of agglomerated vorticity is from the upper surface of the cylinder, whereas in Figure 4.1.9c, it is from the bottom surface. Near the bed, h_L/h_w=0.04, this vorticity cluster is relatively concentrated, and at higher elevations of the midplane, h_L/h_w=0.5, and free-surface, h_L/h_w=0.94, it becomes more enlarged. This trend is apparently associated with the larger spatial

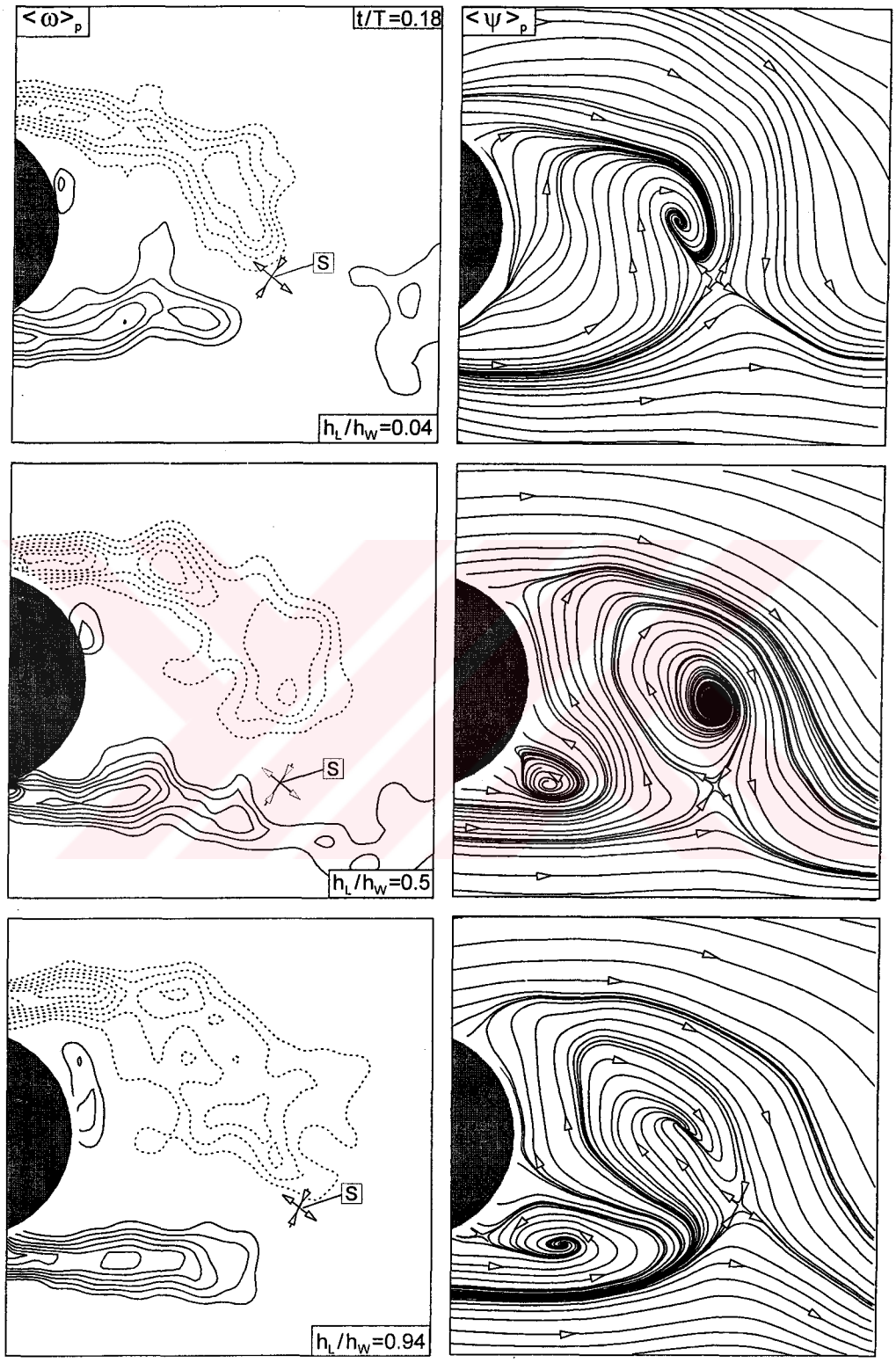

Figure 4.1.9b. Comparison of phase-averaged patterns of vorticity and streamline topology at elevations corresponding to the bed surface, the midplane and the free-surface of the shallow water layer at a given instant t/T = 0.18, where T is the period of Karman vortex formation. Minimum and incremental values of vorticity are $\omega_{min} = \pm 6\ sec^{-1}$ and $\Delta\omega = 4\ sec^{-1}$.

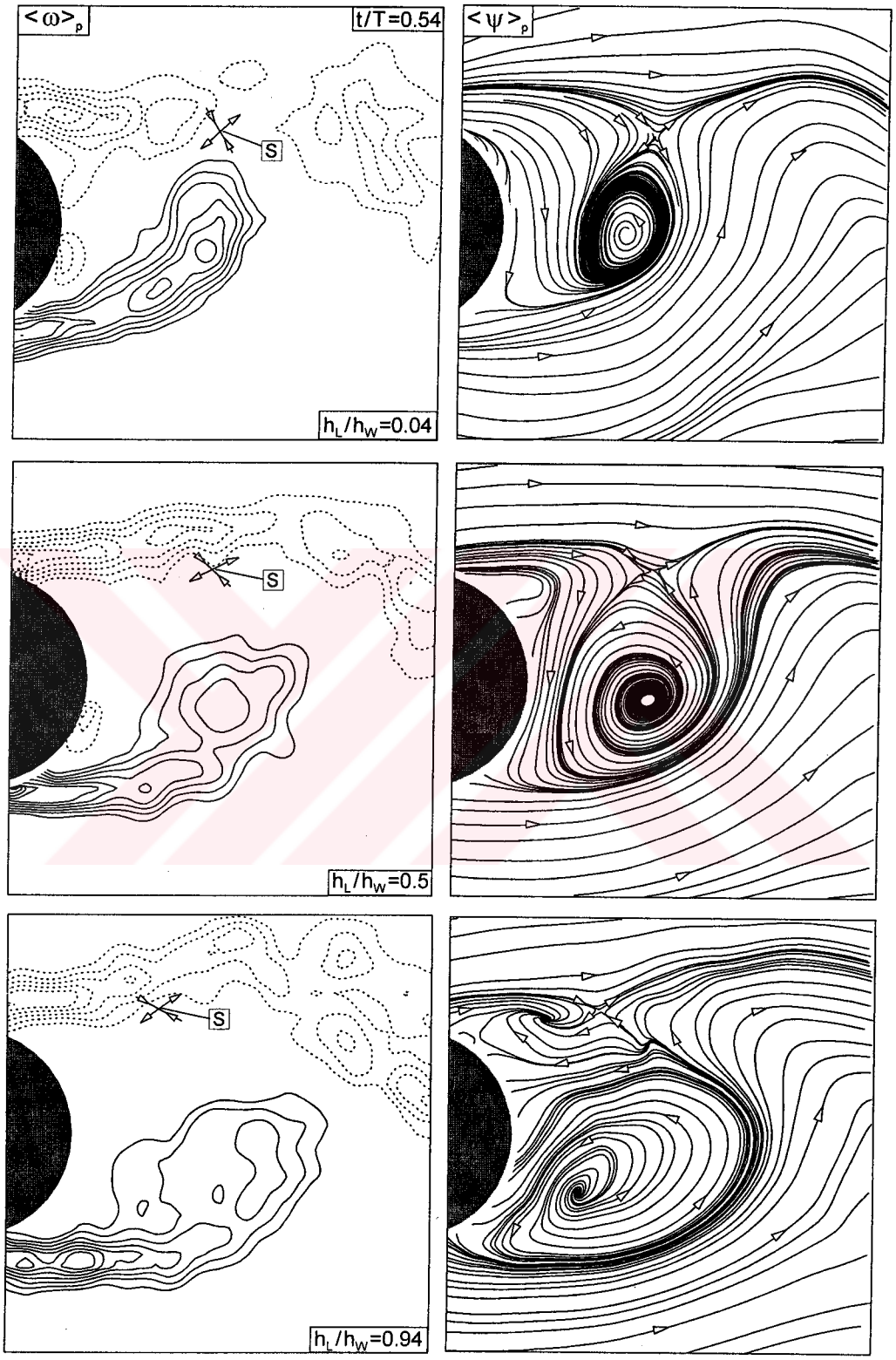

Figure 4.1.9c. Comparison of phase-averaged patterns of vorticity and streamline topology at elevations corresponding to the bed surface, the midplane and the free-surface of the shallow water layer at a given instant t/T = 0.54, where T is the period of Karman vortex formation. Minimum and incremental values of vorticity are $\omega_{min} = \pm 6\ sec^{-1}$ and $\Delta\omega = 4\ sec^{-1}$.

extent of the corresponding spiral-like streamline patterns at elevations above the bed.

4.1.6. Instantaneous Flow Structure in the Near-Wake Region of Vertical Cylinder

Instantaneous velocity vectors and vorticity contours in near-wake region of a vertical cylinder near the bed, at the midplane and free-surface elevations of shallow water layer are illustrated in Figure 4.1.10. For all elevations of shallow water layer, there is a well-defined, large-scale vortex formed from upper side of the cylinder. It has small-scale, Kelvin-Helmoltz vortices embedded within it. Especially, for free-surface elevation of shallow water layer, h_L/h_W=0.94, the small-scale vortices are evident on the lower side of cylinder. Identifiable small-scale concentrations of vorticity are detectable not only in the shear layers from the cylinder, but also in the eventually formed large-scale concentration of vorticity. The instantaneous structure of the separated layer which feeds into the Kármán vortex. A common feature of nearly all of the instantaneous flow structure in the near-wake region is the abrupt onset of well-formed, small-scale vortical structures in the shear layers from the cylinder. For all elevations of shallow water layer, the location of vortex formation is formed nearly at the same region.

4.1.7. Concluding Discussion

Local mean velocity distribution that was measured by the PIV agrees well with the previous results taken from the literature. This test was conducted to make sure that fully developed flow exists in the test chamber.

The pattern of time-averaged streamlines, near the bed elevation, shows that a saddle point and hence separation occurs just in front of the cylinder.

Horizontally oriented vorticity gradually grows and rolls up towards the cylinder which demonstrates how turbulent-like eruptive behavior of flow can occur in the base of the cylinder.

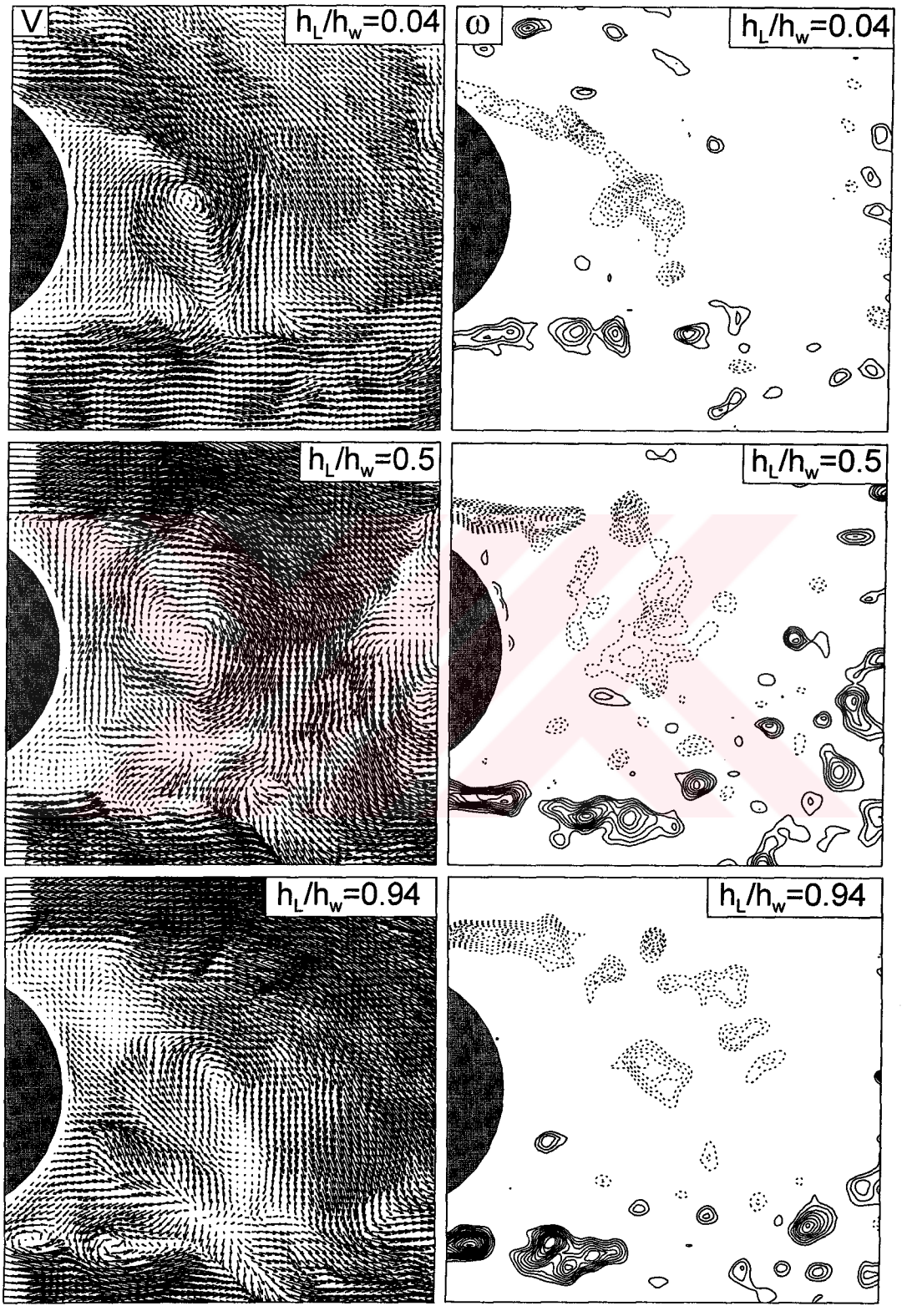

Figure 4.1.10. Patterns of instantaneous velocity vectors V and vorticity ω, near-wake region of a vertical cylinder, near the bed, $h_L/h_w = 0.04$, at the midplane, $h_L/h_w = 0.5$ and free-surface elevation, $h_L/h_w = 0.94$ of the shallow water layer. Minimum and incremental values of vorticity are $\omega_{min} = \pm 15$ sec^{-1} and $\Delta\omega = 5$ sec^{-1}.

The pattern of time-average streamline topology obtained near the bed elevation resembles with the surface topologies of Perry and Chong (1986). Wake region near the bed elevation occupies a larger area comparing to the results of midplane and free-surface elevations. But, counters of positive and negative time-averaged vorticity appear in close proximity to one another.

Stronger concentrations of Reynolds stress occur at the midplane and surface plane along the separation lines.

Instantaneous streamline topology and vorticity patterns in the plan views, in close region near the bed surface, a midplane and free-surface elevations reveals several features that are in general, associated with the topology from bluff-body wake of large spanwise extent. The location of the saddle point at various phases of the oscillation cycle is correlated with the patterns of vorticity in the near-wake region. The spanwise extent of the pattern of swirling streamlines increase with increasing elevation. Near the bed surface elevation, two saddle points exist but, in other images of plane view with a high level elevation there is only one saddle point. Akıllı and Rockwell (2002) indicated that in very close to the base of the cylinder, additional topological features exists near the bed surface, for example, in close region of the rare side of cylinder, there are symmetrical saddle points and an unstable node occurs at an elevation of h_L/h_w=0.06. This class of flow feature does not exist in the present experiment. This difference of phenomena may be caused due to the elevation differences. Whole foregoing features at the averaged topology are correlated with patterns of averaged vorticity and Reynolds stress. Near the bed surface elevation the vorticity layers remain relatively narrow and move toward the plane of symmetry of the base. At the same elevation a well-defined cluster of Reynolds stress close to the base are not evident. Whereas, the midplane of shallow water layer contains well organized clusters. The necklace or horseshoe vortices organizing from the inflow cylinder interactions cause extra Reynolds stress.

4.2. Control Vortex Formation From a Vertical Cylinder in Shallow Water: Effect of Localized Bed Roughness

An overview of the experimental system is given in Figure 4.2.1a. A cylinder of diameter D=50.8 mm pierced the free-surface. This cylinder was positioned a distance of 2,845 mm from the leading of the test section, in order to allow development of a fully turbulent boundary layer, according to the criteria of Kırkgöz and Ardıçoğlu (1997). The velocity of the free-surface was U=177.8 mm/s, which gives a values of Reynolds number, Re=4,498 based on water depth. The corresponding Reynolds number based on cylinder diameter is Re=8,996. For the shallow water wake, it is well known, including Grubišić et al. (1995) and Chen and Jirka (1995), that the existence of a self-excited instability is depended upon a stability parameter mentioned in section 2.2.1. The representation defined by Chen and Jirka (1995) is $S = C_f D/h_w$, in which C_f is bed friction coefficient, D is the cylinder diameter, and h_w is the water depth. For the present configuration, S=0.0132. Kármán-like vortices were formed in the near-wake at a value of Strouhal number $St = fD/\overline{U} = 0.194$, in which $\overline{U}$ is the depth-averaged velocity. The value of Froude number Fr based on the surface velocity U and the water depth h_w is $Fr = U/\sqrt{gh_w} = 0.36$. The corresponding value based on the depth-averaged velocity $\overline{U}$ is Fr=0.32. The inflow is therefore subcritical. Distortion of the free-surface in the vicinity of the cylinder had a maximum value of 0.76 mm. This value is a small fraction of the water depth, i.e., it corresponds to $0.029h_w$.

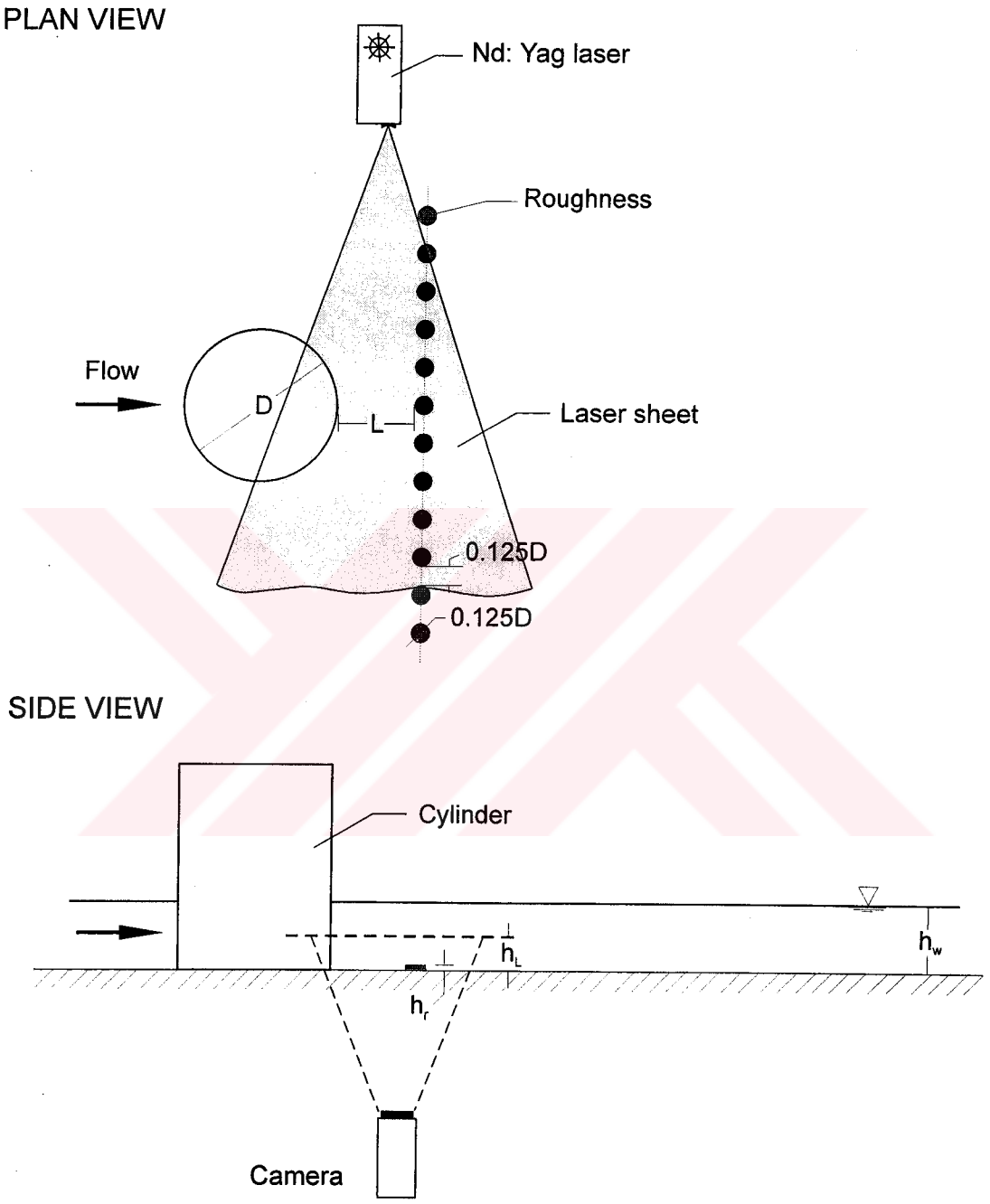

Figure 4.2.1a. Overview of cylinder in shallow water, location of roughness elements, and deployment of laser sheet at various elevations above the bed.

4.2.1. Effect of Roughness and Time-Averaged Topology of Near-Wake Region Near and Above Bed Surface

4.2.1.1. Topology upstream of roughness elements

Figure 4.2.1b gives a comparison between the extreme cases of no surface roughness and a dimensionless roughness $h_r/h_w = 0.25$ for elevations of the sheet near the bed surface $h_L = 0.04$, and at the midplane $h_L/h_w = 0.5$ of the shallow water layer. Near the bed surface, the well-defined critical points are evident such as a saddle point S_1; and the foci F_1 and F_2. The spiral nature of the streamline patterns leading to the foci F_1 and F_2 indicates three-dimensionality of the flow structure near the bed. Furthermore, the streamline patterns spiral inward to the foci, indicating that they are stable. In presence of the relatively large roughness element $h_r/h_w = 0.25$, the surface topology has the same general form, but the saddle point S_1 has moved further downstream from the base of the cylinder, relative to the case of no roughness. In addition, the spatial extent of the spiral pattern is smaller than for the case of no roughness.

The patterns on the midplane, i.e., $h_L/h_w = 0.5$, are represented by the images in the right column. An important feature is the absence of the saddle point S_1, which occurs near the bed. For the cases of no surface roughness and the relatively large roughness, the overall form of the averaged streamline topology is similar. In the presence of roughness, the apparent foci (centers) of the streamline pattern are shifted downstream relative to those corresponding to no roughness. The trajectories are closed curves having the shape of and ellipse that is called center.

4.2.1.2. Effect of localized surface roughness on the overall patterns of averaged streamline topology near the bed surface

Figure 4.2.2 shows a direct comparison of the averaged topology near the bed surface, taken with a field of view that extends over the region downstream of the

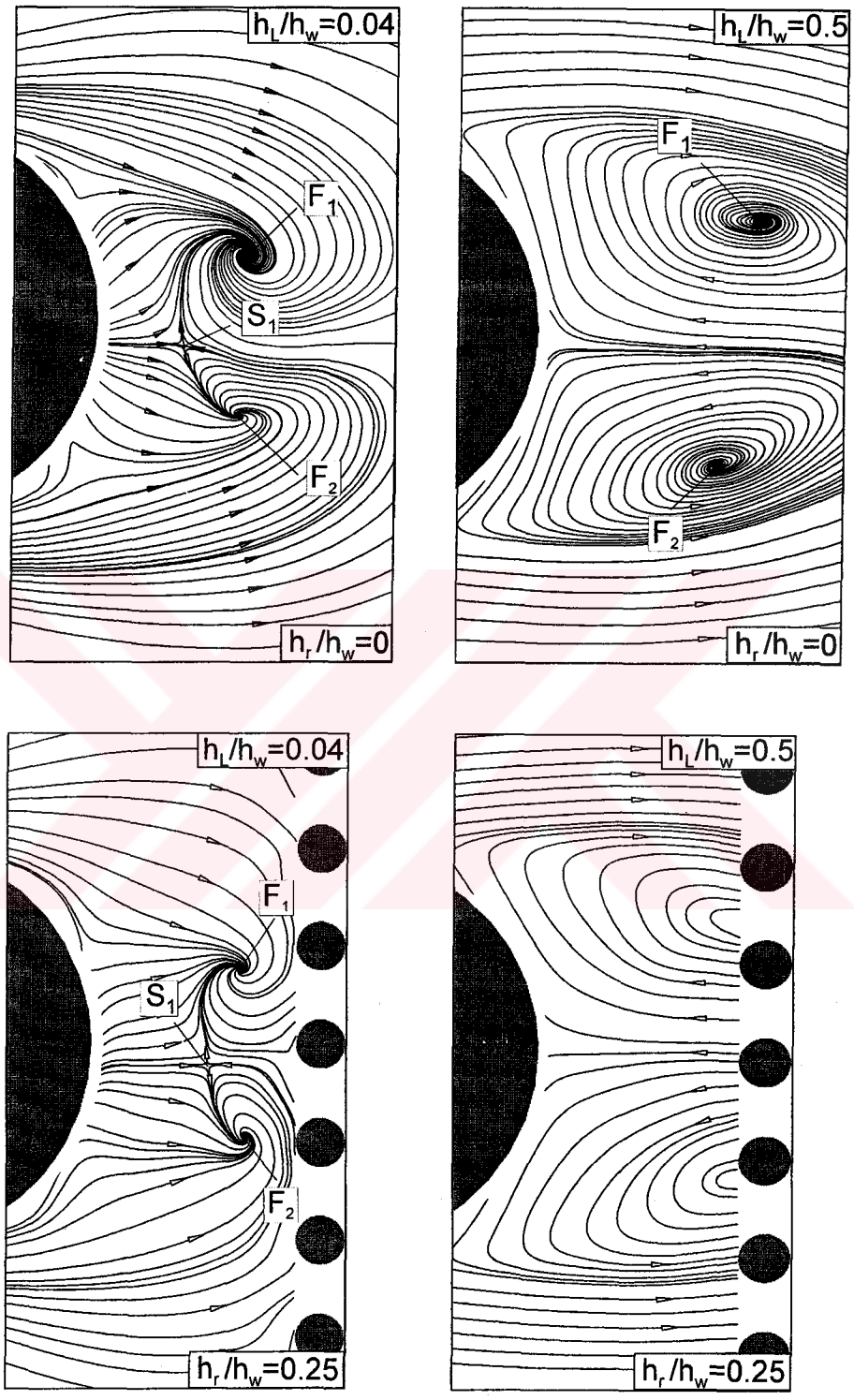

Figure 4.2.1b. Patterns of averaged streamlines in the very near-wake region for cases of no roughness, $h_r/h_w = 0$, and large roughness, $h_r/h_w = 0.25$, at elevations corresponding to the bed surface and the midplane, $h_L/h_w = 0.04$ and 0.5 respectively.

roughness elements. For the case of no roughness, shown in the top image, the two saddle points S_1 and S_2 are connected by an upstream-oriented streamline. In the presence of roughness, as indicated in the middle and lower images, the saddle point S_2 still exists. It is evident, however, that substantial distortion of the topology, relative to the case of no roughness, occurs immediately downstream of the roughness elements for cases of both relatively small and large roughness, i.e., h_r/h_w = 0.062 and 0.25. Furthermore, the form of surface streamline pattern is distinctly different for both of these cases. The pattern of the bottom image shows that the center of a pattern of concentric streamlines is approximately at the trailing-edge of the roughness elements. In the middle image, such a concentric pattern is not evident. The distance between points S_1 and S_2 enlarges as a function of roughness height. The length of the wake flow region in the lateral direction is the same in all images but the axial length of the wake region is expanded due to the roughness. Balachandar et al. (1999) report that the transverse flow is stable if the bed friction influence is sufficiently strong to suppress the development of the large-scale disturbance. As a consequence, the spanwise extent of the wake will be limited.

Figure 4.2.3 shows a direct comparison of the averaged topology downstream of the roughness elements for planes of observation near the bed and at the midplane of the water layer. Near the bed, corresponding to h_L/h_w = 0.04, as already indicated in Figure 4.2.2, the effect of even a relatively small value of roughness h_r/h_w = 0.062 is to substantially displace the saddle point S_2 in the downstream direction. On the midplane, represented by the images in the right column, relatively large displacement of the saddle point S_2 in the downstream direction occurs and eventually foci F_1 and F_2 appear only for the largest height roughness, as represented in the bottom image. A central feature of all of the patterns in the right column is that the width between streamlines that bound the recirculation cells, i.e., the streamlines that eventually connect to the saddle point S_2, is substantially narrower than the corresponding widths near the bed surface.

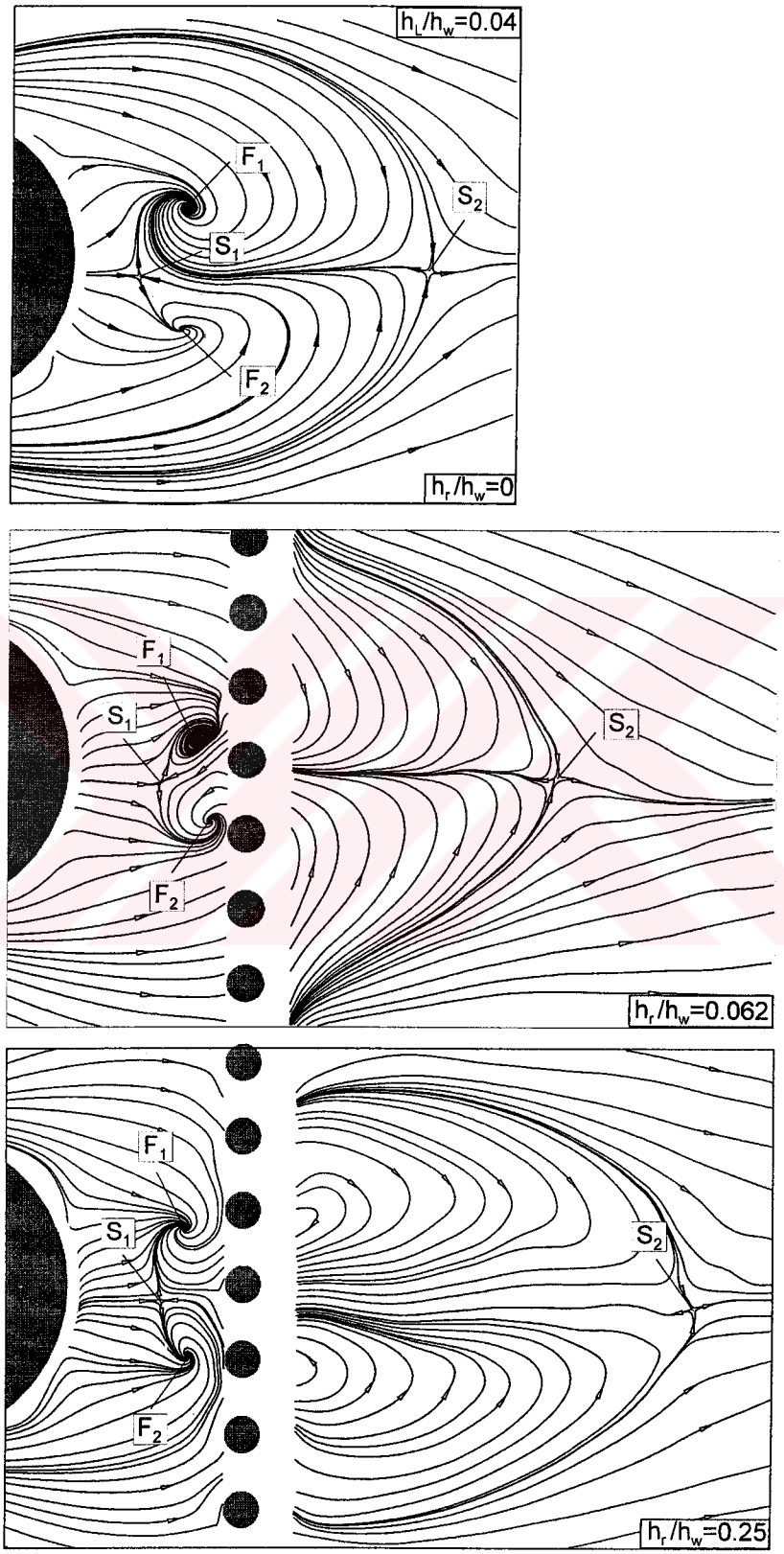

Figure 4.2.2. Overviews of averaged patterns of streamlines near the bed, h_L/h_w= 0.04, for the cases no roughness, small, and large roughness, h_r/h_w= 0, 0.062 and 0.25 respectively.

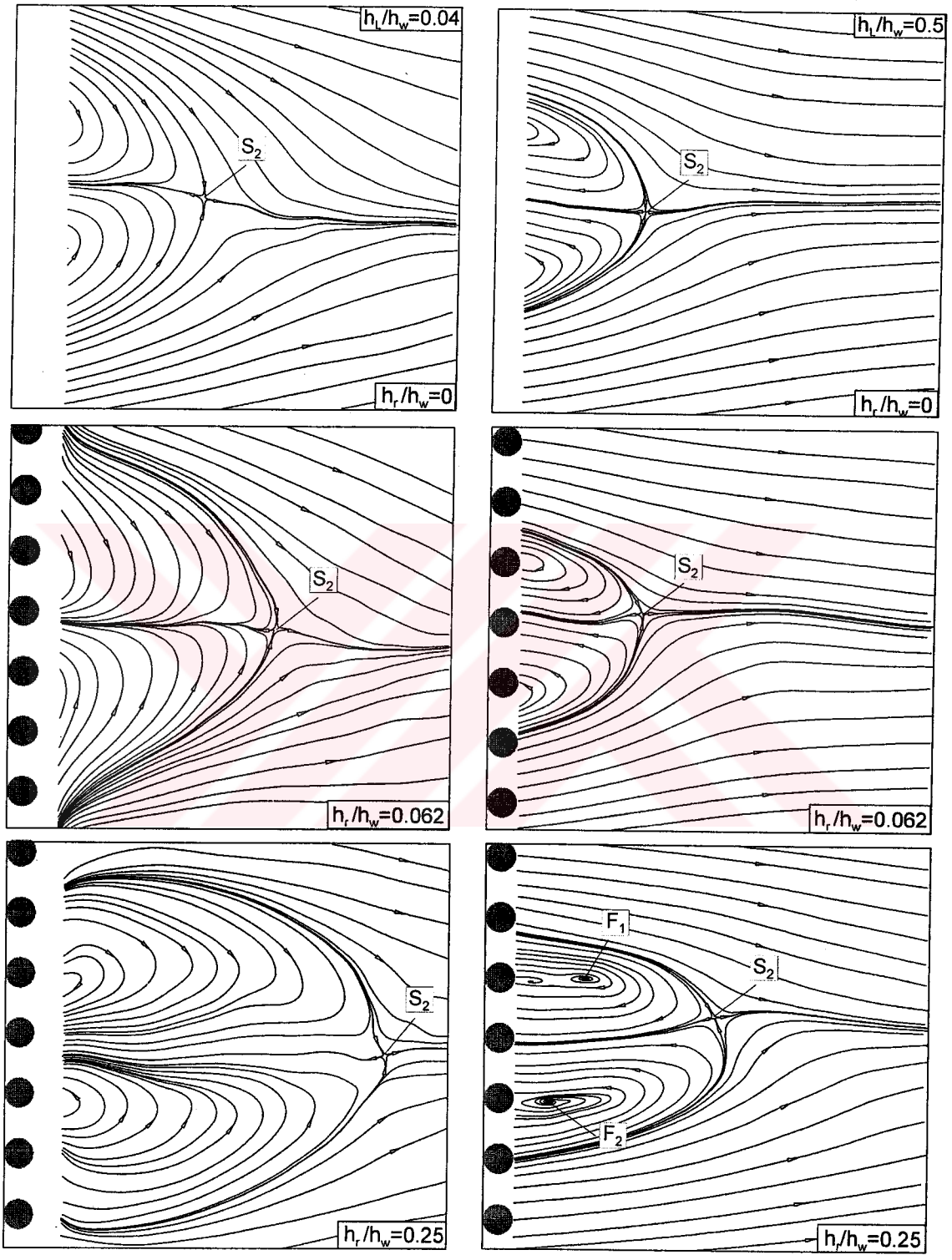

Figure 4.2.3. Direct comparison of patterns of averaged streamlines near the bed, h_L/h_w= 0.04, and at the midplane, h_L/h_w = 0.5, for no roughness, small, and large roughness, h_r/h_w= 0, 0.062, and 0.25 respectively.

4.2.1.3. Effect of roughness on regions of reverse flow

Contours of constant averaged streamwise velocity $<u>/U$ are given in Figure 4.2.4 for elevations near the bed and the midplane of the water layer. In each image, contours of constant positive $<u>/U$ are indicated by solid lines and negative values by dashed lines. Near the bed ($h_l/h_w = 0.04$) and for relatively small roughness $h_r/h_w = 0.062$, the negative pocket of $<u>/U$ extends further downstream than for the case of no roughness, and at the largest value of roughness, the streamwise extent of this negative pocket increases substantially. Regarding the peak negative value of $<u>/U$, it remains approximately equal for cases with and without roughness. At the midplane, represented by the images in the right column, the streamwise extent of the negative pocket of $<u>/U$ is smaller than near the bed for all cases. Again, a significant increase in the streamwise length of the pocket is evident for the largest roughness $h_r/h_w = 0.25$. Obviously averaged streamwise velocity is lower near the bed relative to velocity at the midplane.

4.2.2. Effect of Roughness on Patterns of Reynolds Stress

Figures 4.2.5a and 4.2.5b provide an overview of the effect of surface roughness on patterns of Reynolds stress near the bed surface and at the midplane of the shallow water layer and upstream and downstream of the roughness elements.

4.2.2.1. Effect of roughness on patterns of Reynolds stress correlation upstream of roughness element

The left column of Figure 4.2.5a gives contours of constant Reynolds stress correlation near the bed as a function of dimensionless roughness height h_r/h_w. For the case of no roughness shown in the top image, well-defined positive and negative contours of $<u'v'>/U^2$ are detectable from the near shoulders of the cylinder, due to fluctuations in the separating layers. In addition, pronounced positive and

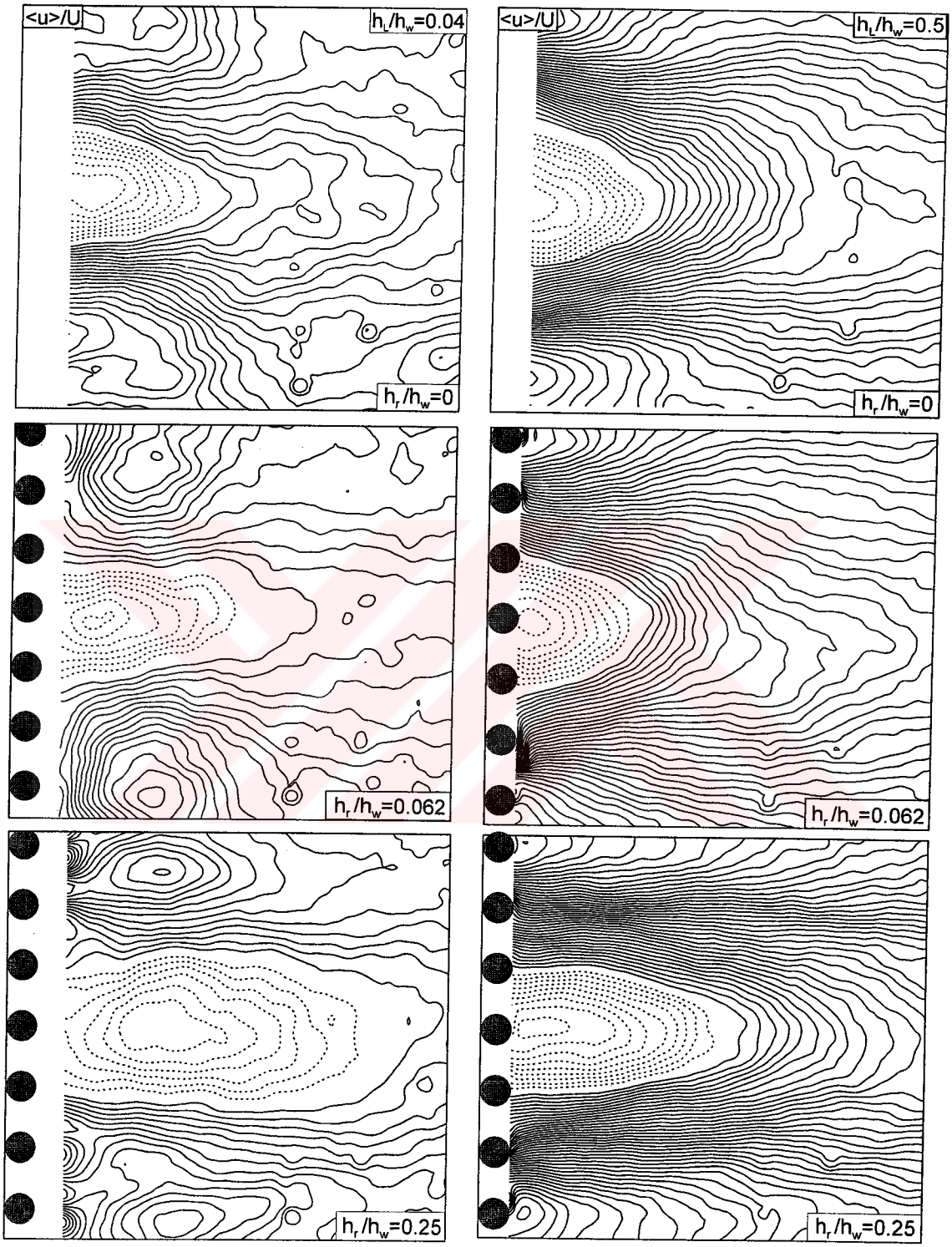

Figure 4.2.4. Patterns of averaged streamwise velocity, < u >/U, near the bed, h_L/h_w= 0.04, and at the midplane, h_L/h_w = 0.5, for no roughness, small, and large roughness, h_r/h_w= 0, 0.062 and 0.25 respectively.

negative concentrations occur immediately downstream of the base of the cylinder. They are due to sweeping of the vorticity layers across this region of the flow during formation of the large-scale vortical structures, as will be illustrated in Section 4.2.3. This pattern of $< u'v' > /U^2$ is, in fact, an inherent feature of the near-wake of a fully-submerged bluff body of large or infinite spanwise extent, due to the classical shedding of Kármán vortices (Mittal and Balachandar, 1995; Lin at al., 2001). For increasing values of dimensionless surface roughness, h_r/h_w = 0.062, 0.125 and 0.25, which are represented successively in the images of Figure 4.2.5a, these concentrations of Reynolds stress near the base region gradually disappear. In addition, the levels of Reynolds stress in the separating layers generally decreases, though an anomalous region occurs in the separated layer from the lower surface of the cylinder. Furthermore, in all images, regions of Reynolds stress are detectable along the top and bottom edges of each image. (Compare with the pattern at the bottom an top edges at the right image of Figure 4.1.3). They are due to fluctuations associated with the necklace or horseshoe vortex formed during the inflow-cylinder interaction. Patterns of $< u'v' > / U^2$ on the midplane are shown in the right column of images of Figure 4.2.5a. The overall trend with increasing roughness h_r/h_w is similar to the trend near the bed. The positive and negative concentrations located immediately downstream of the base are attenuated until, for the largest value of roughness, they are barely detectable. The peak value of Reynolds stress in the separating layers, relative to the case of no roughness, can be attenuated by as much as a factor of three near the bed (h_L/h_w=0.04) and by a factor six at the midplane (h_L/h_w=0.5).

Considering the images of Figure 4.2.5a, the substantial decrease in Reynolds stress for even small roughness h_r/h_w suggests an attenuation of the vortex shedding process in the very near-wake region. This aspect will be further interpreted in conjunction with instantaneous images in the Section 4.2.3. The attenuation of $< u'v' > /U^2$ even for the smallest roughness element h_r/h_w = 0.062, both near the bed and at the midplane, indicates that the effect of localized roughness is a global one, which extends over a substantial volume of the upstream region of the flow. The

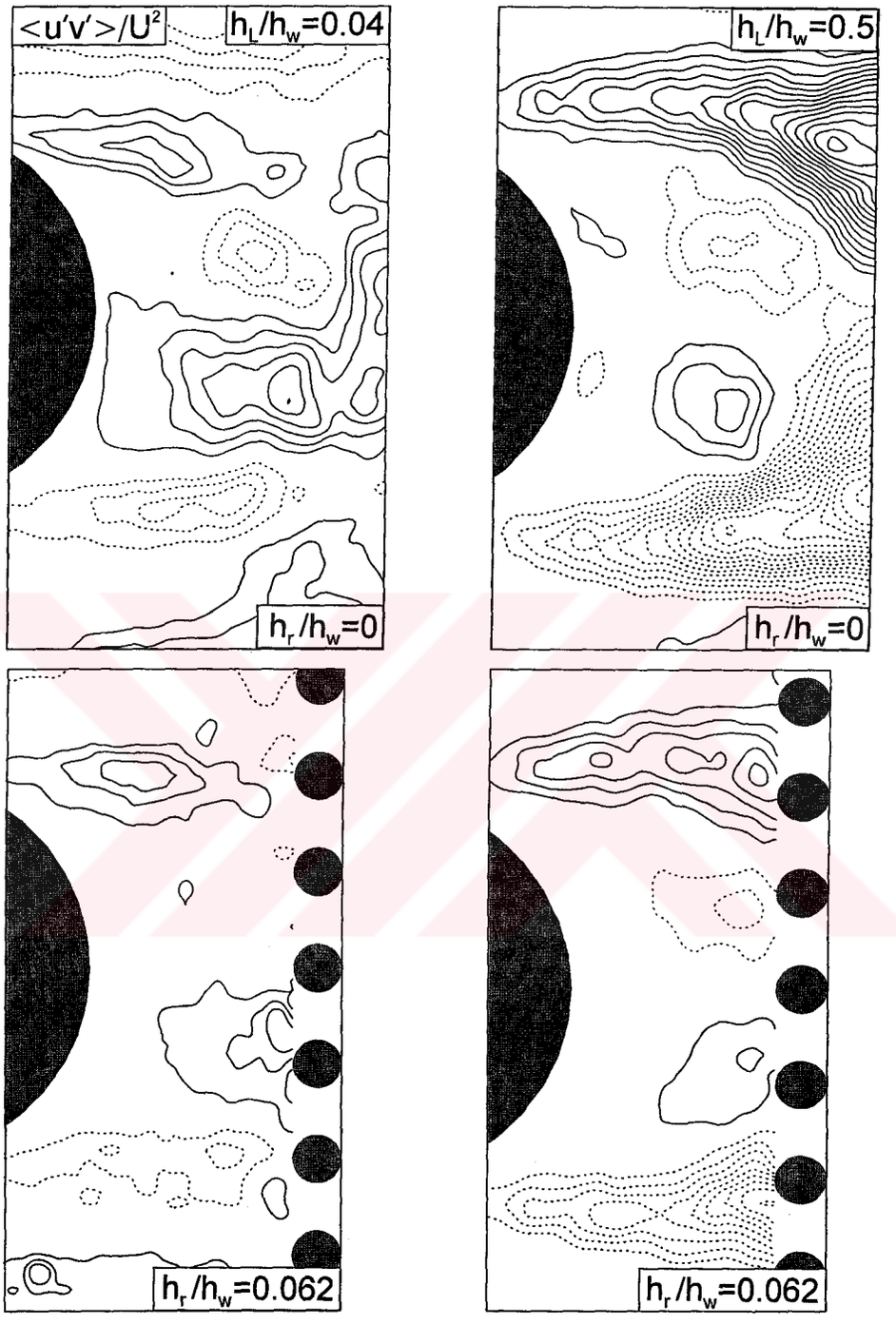

Figure 4.2.5a. Patterns of dimensionless Reynolds stress correlation, at locations upstream of the roughness elements, near the bed, $h_L/h_w = 0.04$, and at the midplane of the water layer, $h_L/h_w=0.5$, for no roughness, $h_r/h_w = 0$, and increasing values of roughness, $h_r/h_w = 0.062$, 0.125 and 0.25. For all images, the minimum and incremental values of dimensionless Reynolds stress correlation are $[\langle u'v'\rangle/U^2]_{min} = \pm 0.005$ and $\Delta[\langle u'v'\rangle/U^2]=0.005$.

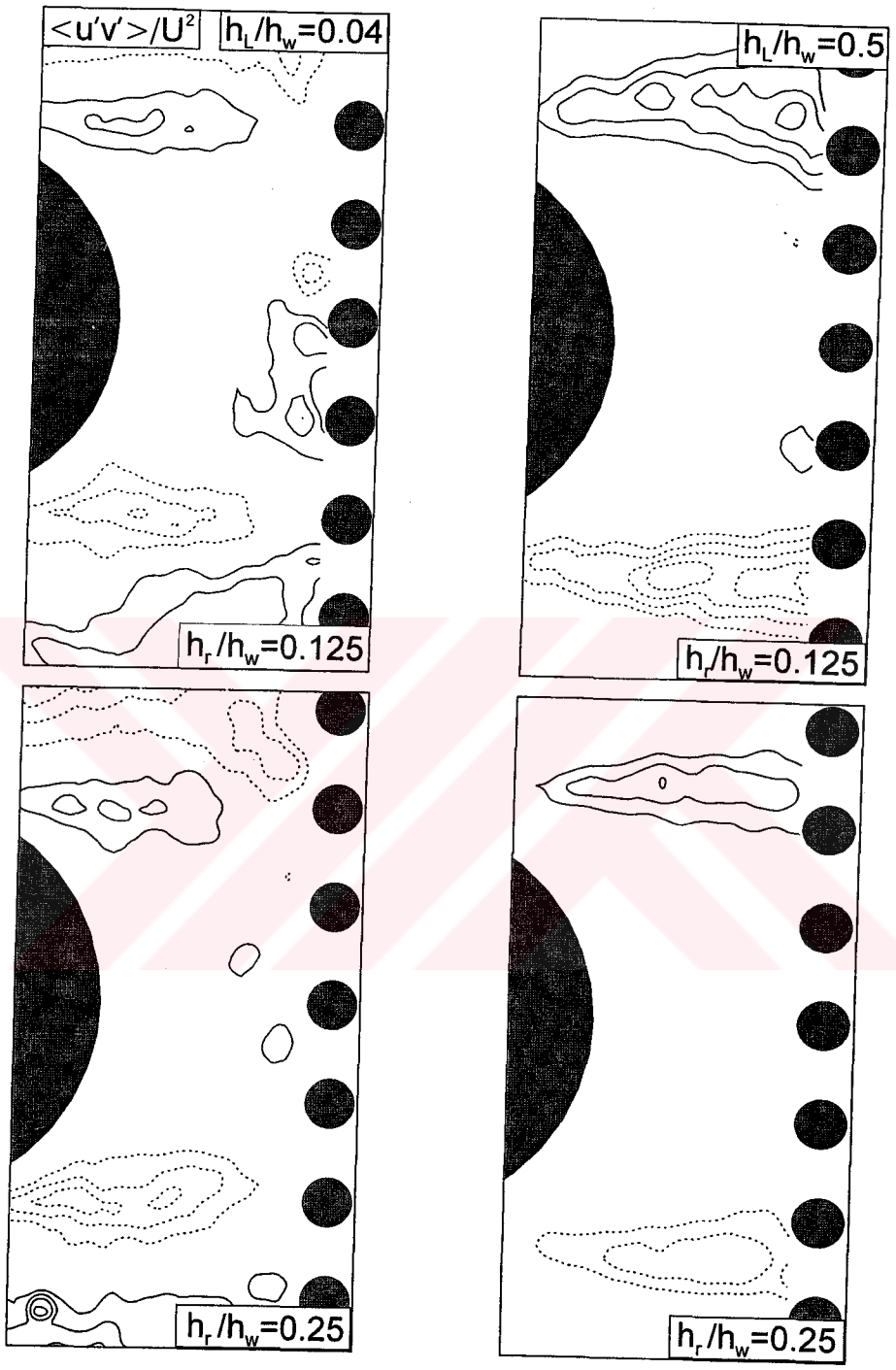

Figure 4.2.5a. Continued.

implication is that localized roughness interferes with the large-scale Kármán vortex formation, which arises from a global (absolute) instability in the near-wake region.

4.2.2.2. Effect of roughness on patterns of Reynolds stress downstream of roughness elements

The images of Figure 4.2.5b show the downstream consequence of the localized roughness on contours of constant Reynolds stress of $< u'v' > / U^2$ near the bed $h_L/h_w = 0.04$ and at the midplane $h_L/h_w = 0.5$. Consider, first of all, the patterns of Reynolds stress near the bed, shown in the left column of images. For the case of no roughness, well-defined concentrations of Reynolds stress occur on the left side of the image, whereas on the right side of the image, which represents a larger streamwise distance, only low levels of Reynolds stress are evident. In the presence of small roughness, $h_r/h_w = 0.062$, represented by the second image, the aforementioned concentrations of Reynolds stress become less distinct and, in fact, a number of interlaced lower level regions of $< u'v' > / U^2$ are evident. For this smallest roughness, the peak value of Reynolds stress $< u'v' > / U^2$ is approximately a factor of two smaller than for the case of no roughness. For $h_r/h_w = 0.125$, a number of clusters of $< u'v' > / U^2$ are again evident, and for the largest roughness $h_r/h_w = 0.25$, the patterns of $< u'v' > / U^2$ extend over larger, less defined regions.

For the flow under consideration, two distinct turbulence scales can be distinguished. There is a large-scale vortex motion generated by the cylinder and small-scale vortex motion generated by the bed friction. The bed friction, besides generating the small-scale motion, exerts a stabilizing influence on the large-scale motion (Balachandar et al., 1999).

This artificial roughness used in the present experiment generates small-scale motions which take roll of stabilizing the large-scale motion causing a reduction in Reynolds stress. But one can pay attention to the height of roughness which may be take roll of increasing the Reynolds stress as it happen in the case of $h_r/h_w = 0.25$. Tachie and Balachandar (2001) compared the results of show wakes generated by the

smooth and rough surfaces. They also concluded the flow over the smooth surface experience a relatively lower momentum loss as the flow approaches the test body. This will results in a higher separating velocity and consequently larger defect in the wake region.

In the right column of images of Figure 4.2.5b, corresponding to the midplane of the water layer, all patterns of $< u'v' > / U^2$ have generally a similar form. With increasing roughness, the locations of the extrema of $< u'v' > / U^2$ are displaced downstream. The peak value of $< u'v' > / U^2$ at the smallest value of roughness h_r/h_w = 0.062 is nearly a factor of two smaller than for the case of no roughness.

It can be concluded that the smallest height of roughness with constant diameter h_r/h_w=0.062 reduces the magnitude of the Reynolds stress near the bed surface and midplane. But increasing the height of the roughness to a h_r/h_w=0.25 the level of Reynolds stress also increases. This is due to the fact that each regions creates individual vortices with greater magnitude. This happens due the emerging flow from the open gap of the roughness h_r/h_w=0.25 are surrounded by a wake flow in which small-scale vortices appear; the boundary between core and wake flow is one of intense shear. Eventually between core and wake flow involved in the entrainment process and hence the intensity of Reynolds stress increase to a greater value corresponding to the flow of no roughness. For the smallest roughness h_r/h_w=0.062, the level of small-scale vortices are not high enough to create similar type of Reynolds distribution relative to the h_r/h_w=0.25.

These observations of the Reynolds stress patterns of Figures 4.4.5a and 4.4.5b suggest discernible modifications of the instantaneous flow structure, which is addressed in the next section.

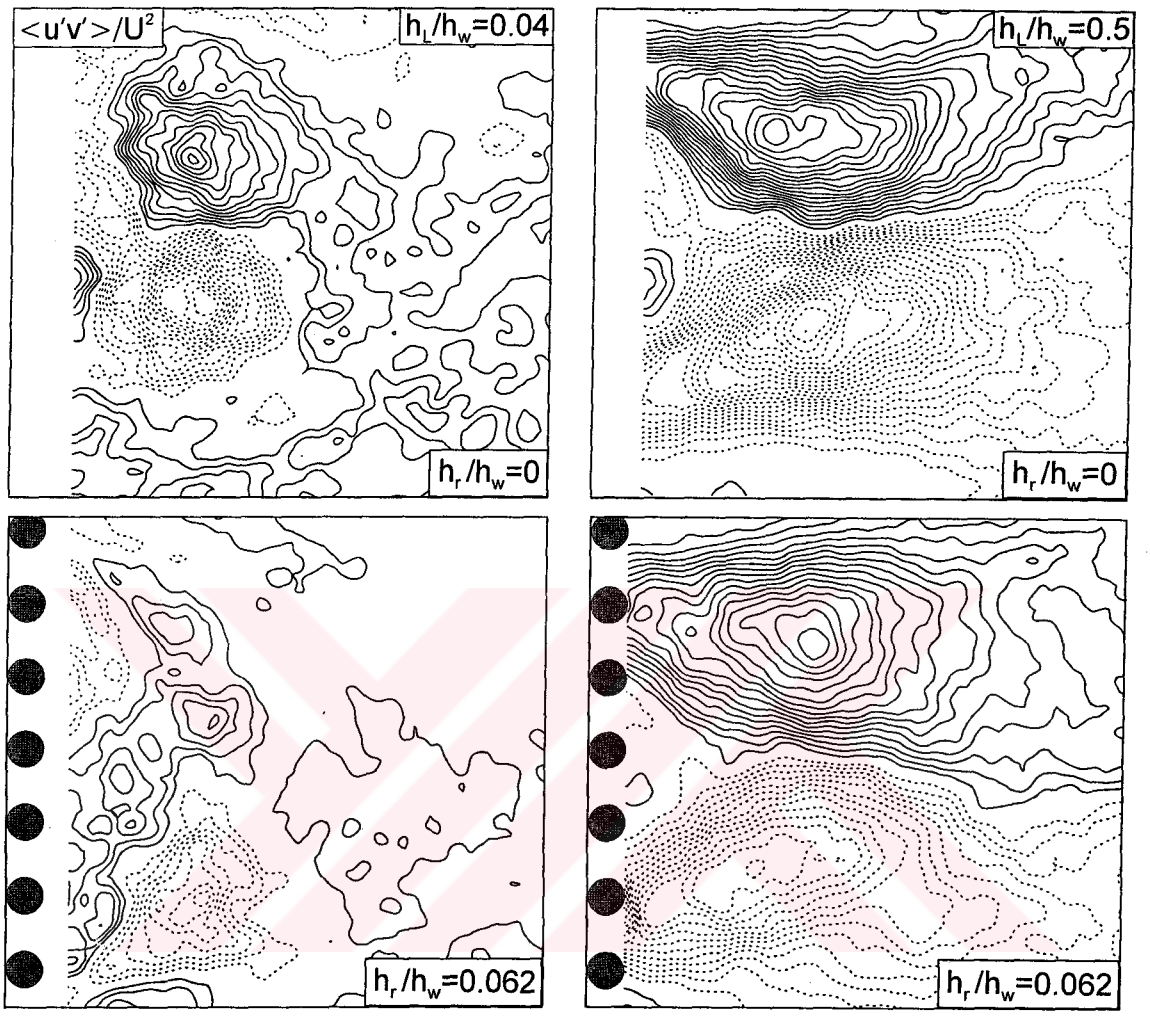

Figure 4.2.5b. Patterns of dimensionless Reynolds stress correlation, at locations downstream of the roughness, near the bed, $h_L/h_w = 0.04$, and at the midplane of the water layer, $h_L/h_w = 0.5$, for no roughness, $h_r/h_w = 0$, and increasing values of roughness, $h_r/h_w = 0.062$, 0.125 and 0.25. For all images, the minimum and incremental values of dimensionless Reynolds stress correlation are $[\langle u'v' \rangle /U^2]_{min} = \pm 0.005$ and $\Delta [\langle u'v' \rangle /U^2] = 0.005$.

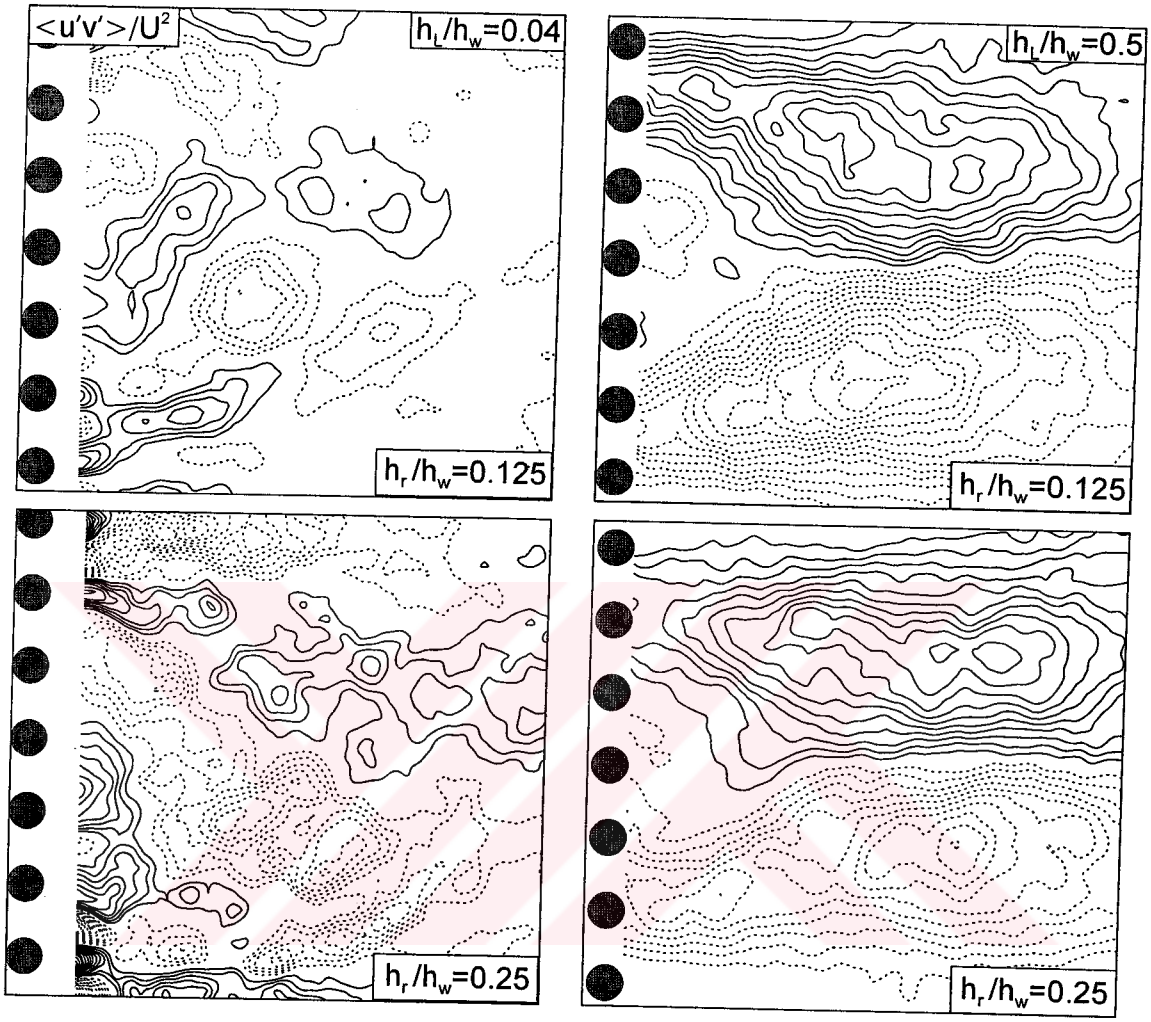

Figure 4.2.5b. Continued...

4.2.3. Effect of Roughness on Global, Instantaneous Flow Patterns

4.2.3.1. Instantaneous patters of velocity and vorticity upstream of roughness elements

The averaged representations of the flow topology and structure described in the previous sections were obtained by averaging the instantaneous images acquired during a given run, as described in Section of Materials and Method. The image layout of Figure 4.2.6a compares representative instantaneous patterns of velocity and vorticity near the bed and midplane, corresponding to h_L/h_r = 0.04 and 0.5, for the cases of no roughness and the case of relatively small roughness, h_r/h_w = 0.062. For the case of no roughness, near the bed, represented by the top row of images (i) and (ii), large-scale swirl patterns of velocity vectors are evident near the base of the cylinder. Corresponding contours of constant vorticity indicate that the shear layer is swept across the base region and exhibits a well-defined, large-scale concentration of vorticity.

In the presence of relatively small roughness, h_r/h_w = 0.062, shown in the third and fourth rows of images of Figure 4.2.6a, large-scale swirls of velocity vectors are no longer evident. Rather, small-scale swirls are present, they appear immediately adjacent to the regions of large velocity gradient on either side of the cylinder. These small-scale structure are due to the small-scale Kelvin-Helmholtz vortices and their coalescence.

Viewed together, the images of Figure 4.2.6a show the sensitivity of the instantaneous structure of the near-wake to small roughness, and reaffirm the interpretation given in Section 4.2.2, namely the global sensitivity of upstream regions of the flow to relatively small, localized roughness near the bed, which is described in the averaged representation of Section 4.2.1.

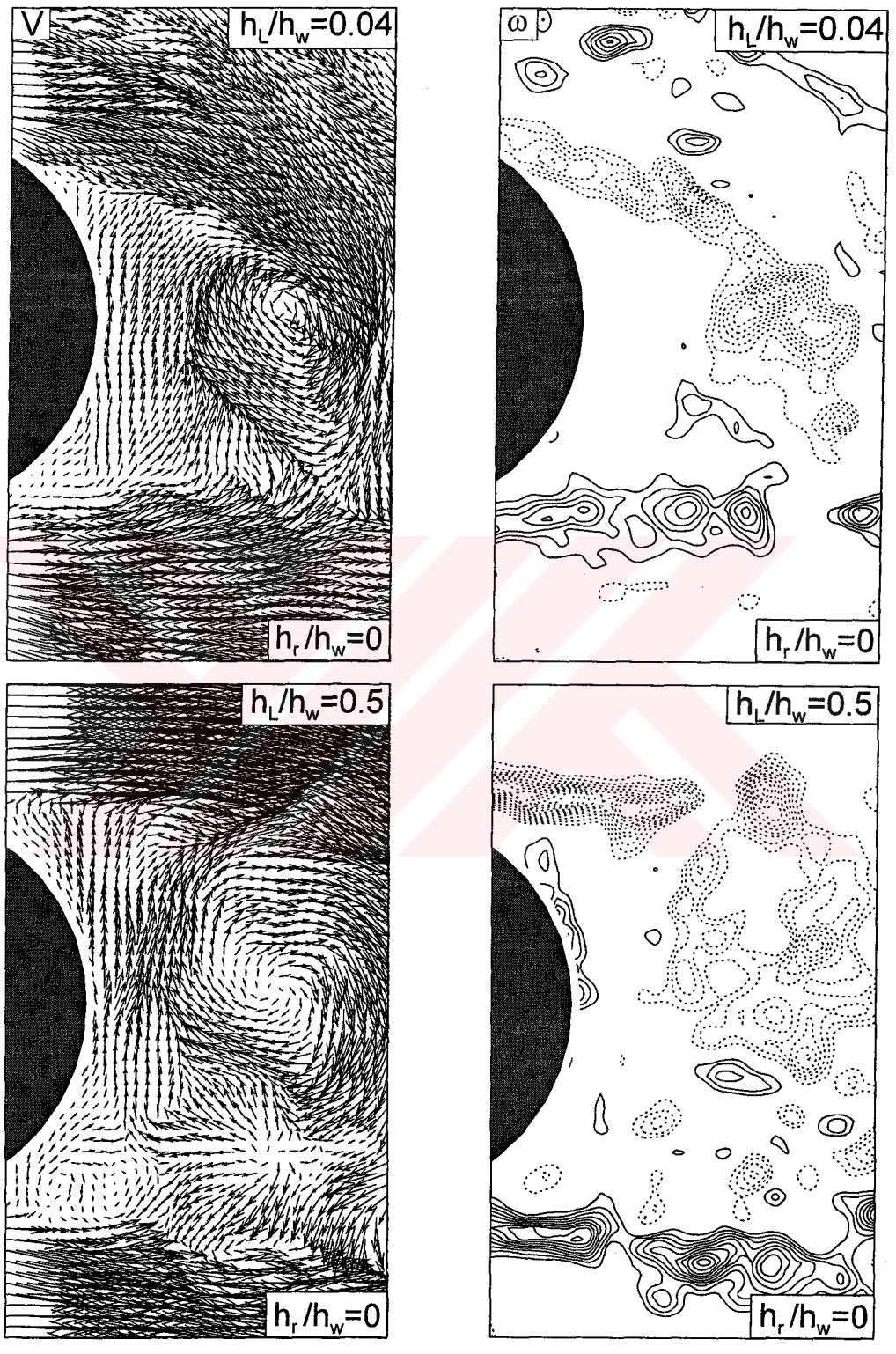

Figure 4.2.6a. Patterns of instantaneous velocity vectors V and vorticity ω, upstream of the roughness elements, near the bed, h_L/h_w= 0.04, and at the midplane of the shallow water layer, h_L/h_w= 0.5, for the case of no roughness, h_r/h_w= 0, and small roughness, h_r/h_w = 0.062. Minimum and incremental values of vorticity are ω_{min} = ±10 sec^{-1} and $\Delta\omega$ = 5 sec^{-1}.

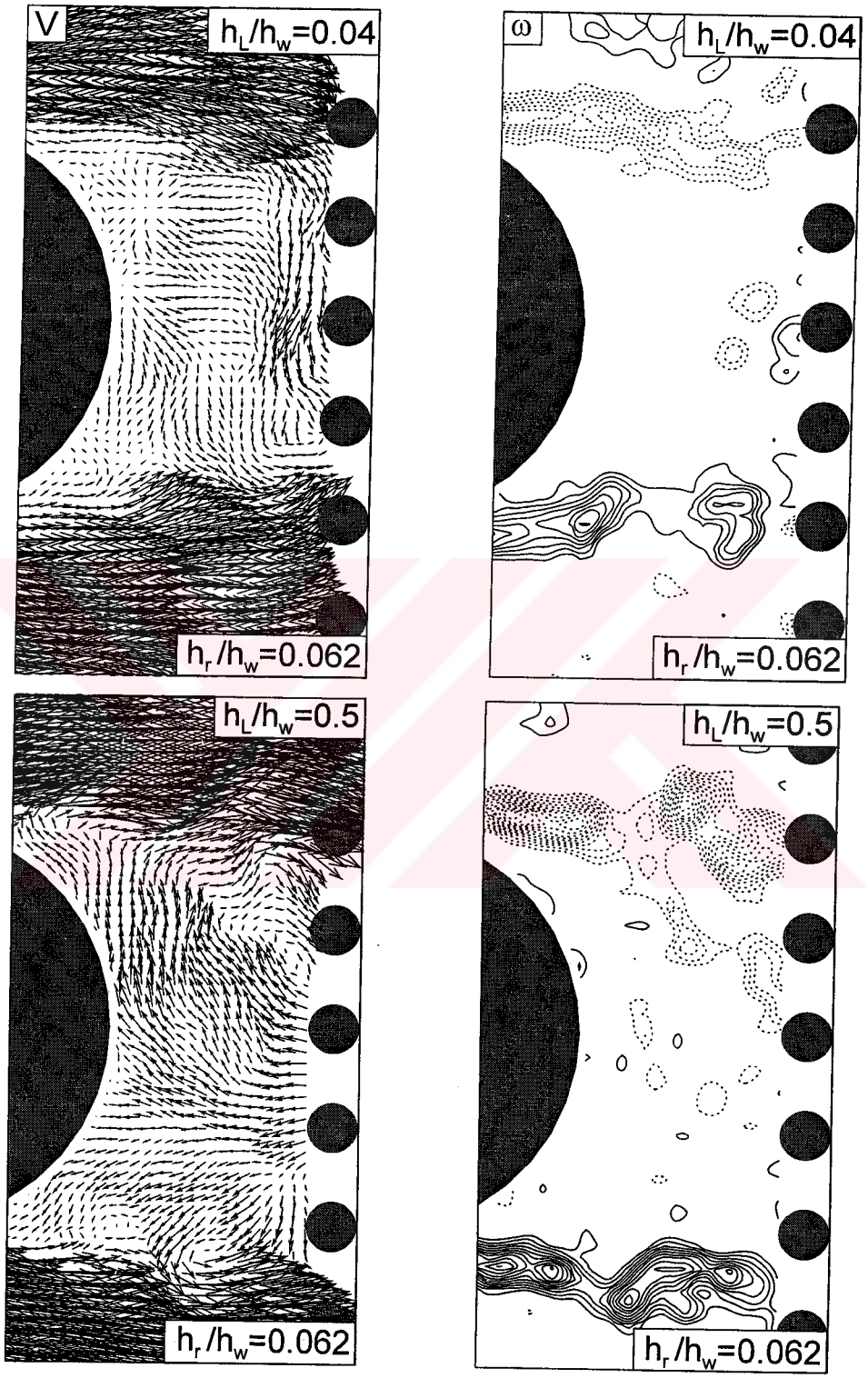

Figure 4.2.6a. Continued..

4.2.3.2. Instantaneous patterns of velocity and vorticity downstream of roughness element

The cases of no roughness and the smallest height roughness (h_r/h_w=0.062) are shown in Figure 4.2.6b. Patterns of instantaneous velocity and vorticity are compared near the bed (h_L/h_w = 0.04) and midplane and (h_L/h_w = 0.5). When selecting the instantaneous images, attempts were made to match the instantaneous patterns at the same phase of the cycle of large-scale vortex formation. In each instantaneous image of velocity, an elongated region of low velocity extends across the wake. In the corresponding patterns of vorticity, elongated positive (solid line) vorticity layers are evident. At the midplane (h_L/h_w = 0.5), these positive layers of vorticity are particularly prevalent, both for cases with and without roughness. It is therefore evident that similar structural features of the flow can occur over regions located downstream of the roughness element. However, this similarity is valid only selected instantaneous images. The time-averaged patterns of Reynolds stress of Figure 4.4.5b show a substantial reduction in peak level of Reynolds stress, even for the smallest roughness element, h_r/h_w = 0.062. That is, in the presence of roughness, the instantaneous patterns of Figure 4.2.6b, which are matched with those for the case of no roughness, occur only in an intermittent fashion.

4.2.4. Concluding Discussion

4.2.4.1. Averaged topology and pockets of reverse flow

The topological features of the averaged streamline patterns near the bed, in the absence of roughness, show an owl-face of the first kind, which involves two well-defined foci and saddle points. In the presence of roughness of various heights, this overall form of the topology tends to persist. That is, if one considers regions both downstream and upstream of the roughness elements, they form, generally

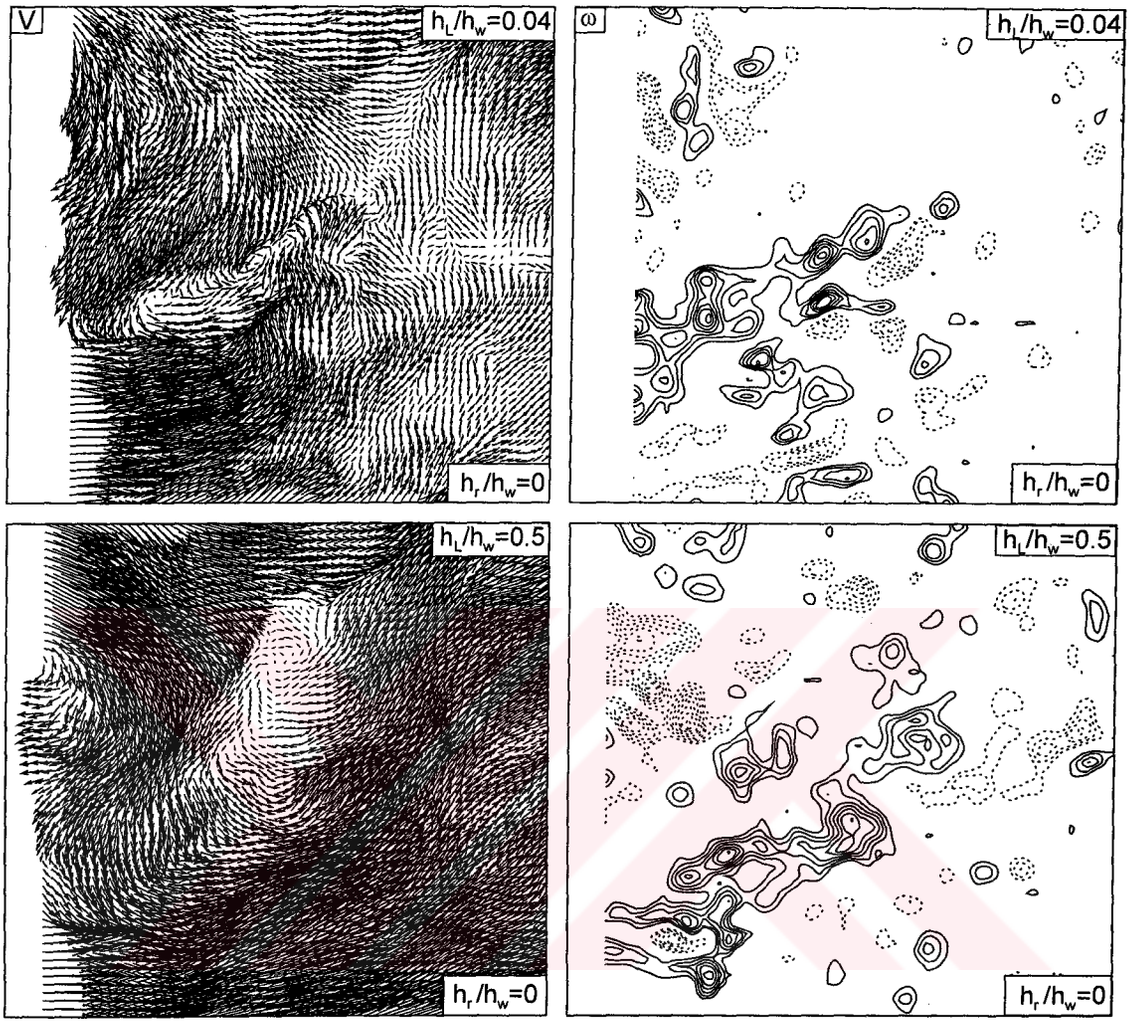

Figure 4.2.6b. Patterns of instantaneous velocity vectors V and vorticity ω, downstream of the roughness elements, near the bed, h_L/h_w= 0.04, and at the midplane of the shallow water layer, h_L/h_w=0.5, for the case of no roughness, h_r/h_w=0, and small roughness,h_r/h_w = 0.062. Minimum and incremental values of vorticity are ω_{min} = ±10 $sec^{-1}$and $\Delta\omega = 5\ sec^{-1}$.

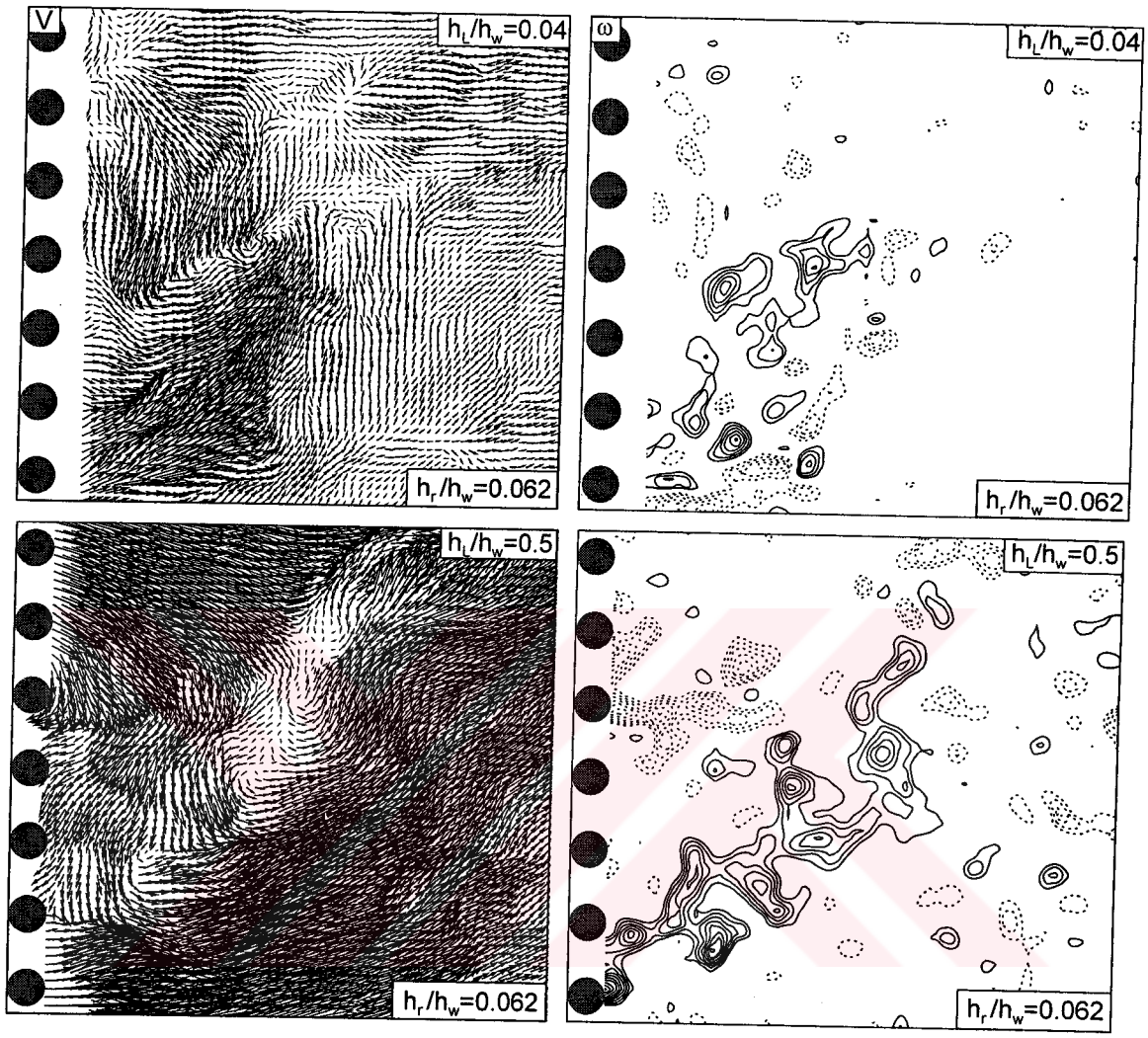

Figure 4.2.6b. Continued.

speaking, an owl-face of the first kind, the details of distortion of the streamline patterns notwithstanding.

These features of the averaged streamline topology are related to the streamwise extent of pockets of negative streamwise velocity near the bed and at the midplane elevations. For the region downstream of the roughness, this pocket of negative streamwise velocity becomes substantially elongated with increasing roughness height, even though the peak value of negative velocity is not altered significantly.

4.2.4.2. Patterns of Reynolds stress

Patterns of Reynolds stress, at both the bed and the midplane, generally show decreasing peak values with increasing height of the roughness. In fact, the smallest roughness height yields a substantial reduction in the Reynolds stress level in the very near-wake, both near the bed and at the midplane. Downstream of the roughness elements, near the bed, the overall pattern of Reynolds stress concentrations, as well as the peak values, is altered substantially near the bed, even for the smallest value of roughness height. At the midplane, the overall form of the pattern of Reynolds stress concentrations remains similar, but the loci of the extrema of the concentrations is displaced downstream with increasing roughness height.

4.2.4.3. Instantaneous patterns of flow structure

All of the foregoing observations are, of course, intimately related to the patterns of instantaneous flow structure represented herein by instantaneous velocity and vorticity. It is demonstrated that even the smallest roughness height clearly attenuates the onset of large-scale, Kármán-like vortex formation in the region close to the base of the cylinder, relative to the case of no roughness. These overall features are evident not only near the bed but also at the midplane.

4.3. Flow Structure From a Horizontally Positioned Cylinder in Shallow Water

Flow structure past a horizontal cylinder beneath a free-surface of shallow water is investigated in this part of the work. In general, flow over circular cylinders immersed in deep water has been studied extensively. But, very little attention has been given to the behavior of flow past a cylinder placed close to the free-surface including shallow water applications. Sheridan et al. (1997) stated that flow past a cylinder in an unbounded medium gives rise to self-sustained, limit cycle oscillations involving formation of large-scale Kármán vortices. Briggs (1964) and Bers (1975) first defined the concept of absolute and convective instability. Chen and Jirka (1998) investigated the linear stability of shallow turbulent mixing layer. Chu and Babarutsi (1988) considered the case of a shallow mixing layer and determined the critical value of the bed friction number for stability. A review paper of Huerre and Monkowitz (1990) and Oertel (1990) reported that the absolute instability which investigates the limit cycle oscillations has recently been recognized. Chen and Jirka (1997) investigated the effect of a bottom friction on the absolute and convective stability characteristics of wake flow by a linear stability analysis and the conditions for transformation between absolute and convective instability, as well as between convectively unstable and stable wake states.

An experimental work of Seal and Smith (1999) allows detailed observation of three-dimensional vortex-vortex and associated vortex-surface interactions that appear similar to those observed in a turbulent boundary layer. They observed that the three-dimensional interactions of the braided vortices induce a pair of local surface-fluid eruptions reminiscent of the near-wall bursting that is characteristic of the near-wall generation process for fully turbulent boundary layers.

Akıllı and Rockwell (2002) investigated the near wake of a vertically placed circular cylinder in shallow water. Kahraman et al. (2002) employed a localized roughness element to control vortex formation from a vertical cylinder. In both works, a technique of high-image-density particle image velocimetry was used in order to provide detailed information of physics of flow of this kind.

As indicated in Figure 4.3.1 cylinders with diameters of D=19.05, 12.70 and 6.35 mm were mounted horizontally and adjusted to desired positions beneath the free-surface. The top of the cylinder touched the free-surface. The corresponding values of Reynolds numbers based on the cylinder diameters were Re=3,374, 2,249 and 1,125 respectively. Furthermore, it is possible to define a Froude number based on the cylinder diameter D as $Fr = U_{max}/\sqrt{gD}$ =0.41, 0.50 and 0.71. The value of Froude number based on water depth h_w is $Fr = U_{max}/\sqrt{gh_w}$ =0.36. As Sheridan et al. (1997) mentioned, there are deviations from one instantaneous image to the next for unsteady flow pattern. Therefore, the flow field must be interpreted with caution in attempting to deduce the time-averaged state of the flow. But, the advantage of the present wholefield approach is that small-scale concentrations of vorticity, which are not phase repetitive with the large-scale vortical events in the flow, are typically lost during time- or phase-averaging processes and can be captured only by considering an instantaneous snapshot of the flow field.

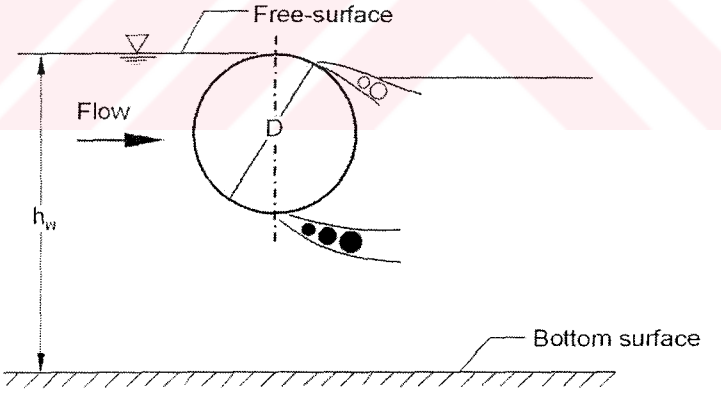

Figure 4.3.1. Overview of experimental arrangement and definition of flow and geometrical parameter

During the experiment, it was found that laser sheet did not illuminate the region of the flow above the top surface of the cylinder. Consequently, both the velocity field and the locus of the free-surface could not be determined in these regions. Therefore, these areas in each image were shaded in white.

In this part of the work, the basic classes of flow structure in the near-wake were also determined experimentally at sufficiently low value of Froude number Fr.

The diameter of the cylinder was increased with small increments in order to determine the values that exhibited major changes in the near-wake patterns. During the course of the experiment, dimensionless cylinder diameters D/h_w=075, 0.50 and 0.25 were used in order to reveal the gradual alterations of near-wake of flow past a cylinder placed beneath the free-surface of shallow water.

4.3.1. Overview of Patterns of Streamlines and Vorticity

Figure 4.3.2a shows the effect of different values of dimensionless cylinder diameter D/h_w = 0.75, 0.5 and 0.25 on the time-averaged patterns of streamlines and vorticity. Prior to starting each experiment, the cylinder was submerged in the shallow water layer such that its upper surface was coincident with the free-surface. When a steady-state flow was attained, the free-surface tended to glide over the upper surface of the cylinder and form a jet-like flow in the near-wake region. Details of this phenomenon are dependent upon the Froude number Fr. Due to reflection and blockage issues associated with the laser illumination, it is not possible to characterize in detail this thin film over the top of the cylinder and in a region extremely close to the cylinder surface in the near-wake region. The possible existence and orientation of this jet-like flow in the wake region could be characterized immediately downstream of the shadow regions (indicated by white background) in each of the images of Figure 4.3.2a. Proper interpretation of the free-surface distortion occurring adjacent to the wake flow of the horizontal cylinder requires accurate determination of the surface coordinates. However, during the experiment, these coordinates of the surface were not tracked. It is evident from the fields of view located closest to each of the cylinders, that the streamline topology in the very near-wake of each cylinder is a strong function of the cylinder diameter and the Froude number $U_{max}/\sqrt{gD}$ =0.41, 0.50 and 0.71 associated with the dimensionless cylinder diameters D/h_w = 0.75, 0.5 and 0.25 respectively. In order to observe the basic classes of flow structure over the large area of the real flow field three different images were merged in one figure as seen in figure 4.3.2a. Here, the overall pattern of the wake, the formation of a large-scale recirculation bubble and

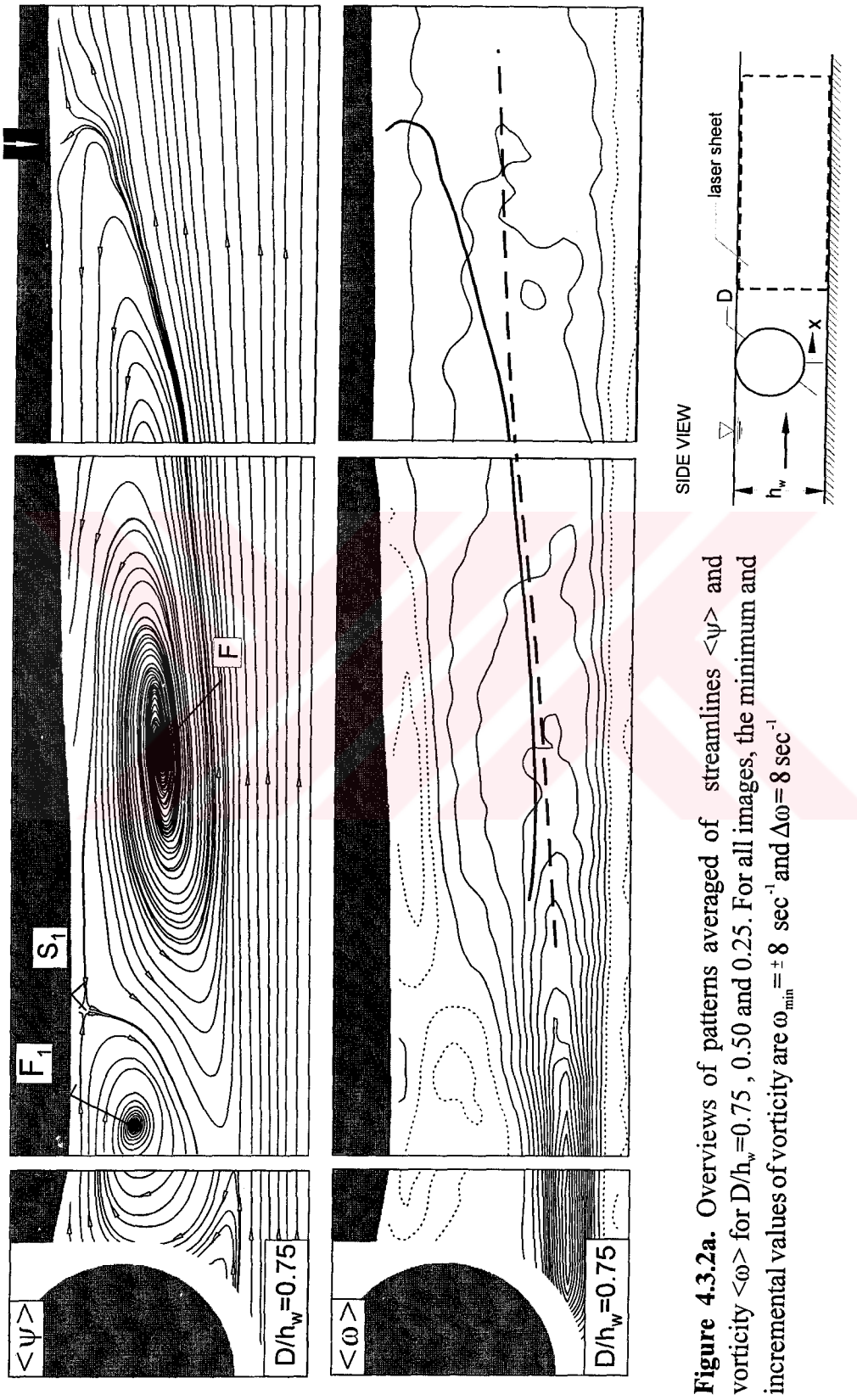

Figure 4.3.2a. Overviews of patterns averaged of streamlines $\langle\psi\rangle$ and vorticity $\langle\omega\rangle$ for D/h_w=0.75 , 0.50 and 0.25. For all images, the minimum and incremental values of vorticity are ω_{min} = ± 8 sec^{-1} and $\Delta\omega$= 8 sec^{-1}

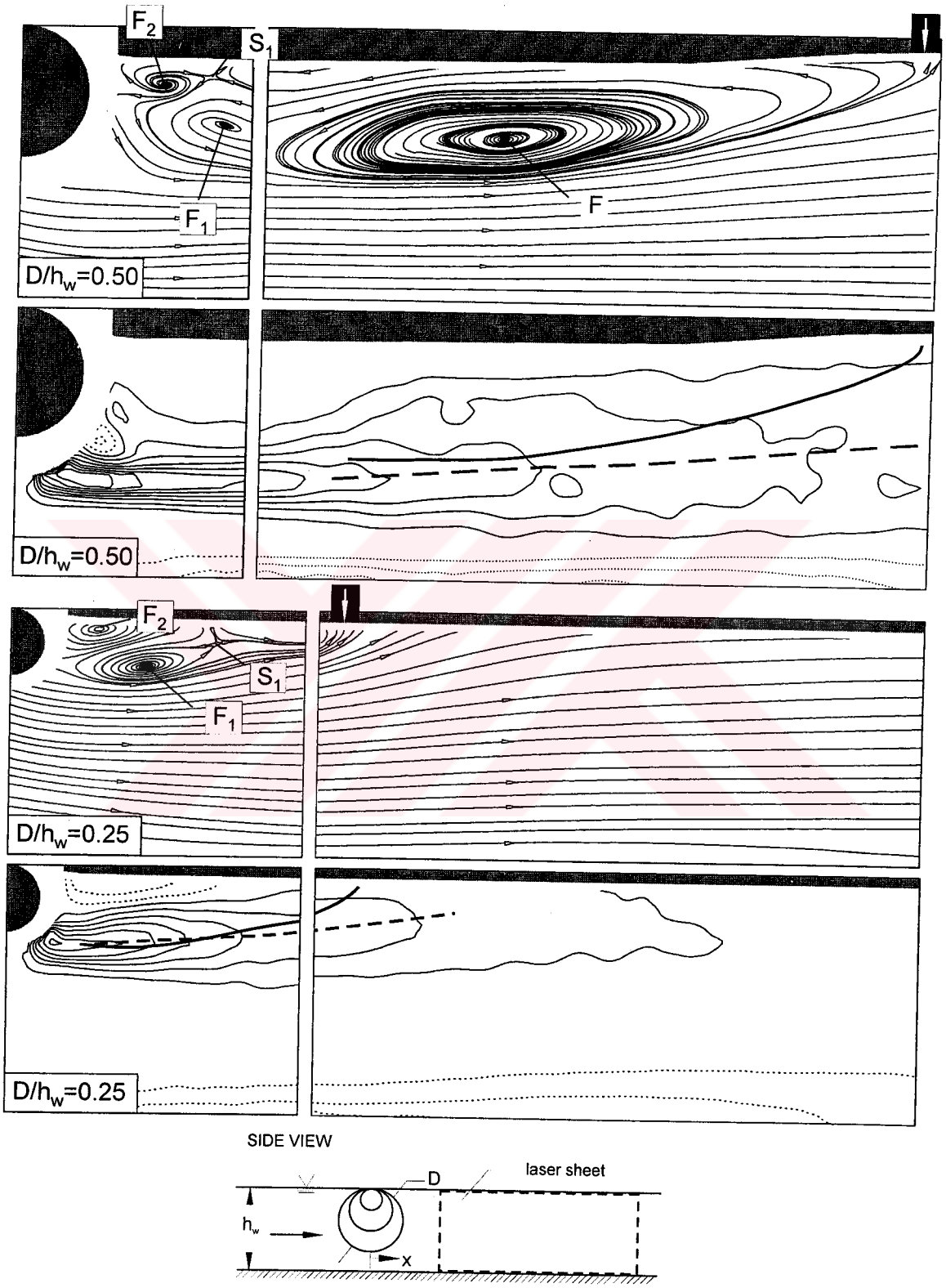

Figure 4.3.2a. Continued.

the reattachment point can be seen instantaneous values of each image was taken at different times. The pattern of streamlines consistently resembles a complete recirculation bubble the wake flow region. The counter-flow occurs in the upstream direction between the free-surface and the mixing layer which starts from the bottom surface of the cylinder that satisfy the entrainment demands of the mixing layer. These features will be addressed in further detail in Figure 4.3.2b.

Viewing each of the flow fields of Figure 4.3.2a as a whole, it is evident that a well-defined reattachment relocation is a common feature; it is indicated by the vertical arrow immediately adjacent to the free-surface. For all configurations, it is possible to identify a primary recirculation bubble, whose focus (apparent center) is designated as F. Furthermore, each of these primary cells has an unstable focus that is the streamlines spiral outward from the focus F, with the exception of the domain in the immediate vicinity of F, whereby limit cycle (closed) streamlines are evident. Furthermore, for the largest value of $D/h_w = 0.75$, an additional recirculation cell with a focus F_1 exists, and a half-saddle point S_1 occurs immediately adjacent to the free-surface between the foci F_1 and F. The streamline emanating from S_1 is oriented outward towards the free-stream and eventually defines the edge of the recirculation cell centered at F.

For the smaller value of $D/h_w = 0.5$, the focus F_1 appears close to the base of the cylinder, and the saddle point S_1 has moved away from the free-surface, and closer to the base of the cylinder. For $D/h_w = 0.25$, the cell with a focus F_1 is identifiable and the saddle point S_1 is displaced well beneath the free-surface.

4.3.1.1. Patterns of Averaged Vorticity

The shear layer formed from the lower surface of the cylinder has a magnitude of average vorticity $\langle\omega\rangle$ that rapidly decreases with decreasing values of D/h_w. For $D/h_w = 0.75$, 0.5 and 0.25 respectively, values of peak averaged vorticity are 132.95, 84.19 and 66.80 sec^{-1}. For each of these patterns of averaged vorticity $\langle\omega\rangle$, the line with long dashes corresponds to the approximate center of each of the contours of constant vorticity, ω. On the other hand, the solid-line corresponds to the

reattachment streamline. It is evident that these two lines are coincident at the upstream locations, but rapidly diverge as the flow reattaches to the free-surface. The length of the wake flow region in the streamwise direction is function of D/h_w. For 0.75, a high rate of jet-like flow exists between bed and lower surface of the cylinder.

4.3.2. Topology of Very Near-Wake Region in Relation to Jet-Like Flow Patterns

Figure 4.3.2b directly compares patterns of streamline topology, along with foci F and saddle points S identified in Figure 4.5.2a, with the averaged velocity fields in the near-wake region. For the top row of images, which represent D/h_w = 0.75, a jet-like flow, which originates from the thin layer of water over the top of the cylinder, is evident immediately beneath and essentially parallel to the free-surface. As a result, a large-scale swirl pattern of velocity vectors and streamlines exists in the near-wake region. The saddle point appears near the separation line at the lower region near-wake flow. Streamline topology and vector velocity show that rotation of the vertical of the near-wake flow occurs in clockwise direction.

On the other hand, for the case D/h_w = 0.5, shown in the second row of images, the pattern of velocity vectors shows that the jet remains attached to the surface of the cylinder, and is deflected downwards in contrast to the previous situation. This phenomenon was first identified by Sheridan et al. (1998). The consequence of this type of jet-like flow from the cylinder is to induce a more complex topology in the near-wake region, involving foci F_1 and F_2, along with a saddle point S_1, which is displaced beneath the free-surface. The rotation of vortical structure of the near-wake flow happens in counterclockwise direction. Finally, for the bottom row of images, corresponding to the smallest diameter cylinder, D/h_w = 0.25, a jet-like flow is not identifiable, and the topology shows two cells with foci F_1 and F_2 with the saddle point S_1 displaced relatively far beneath the free-surface.

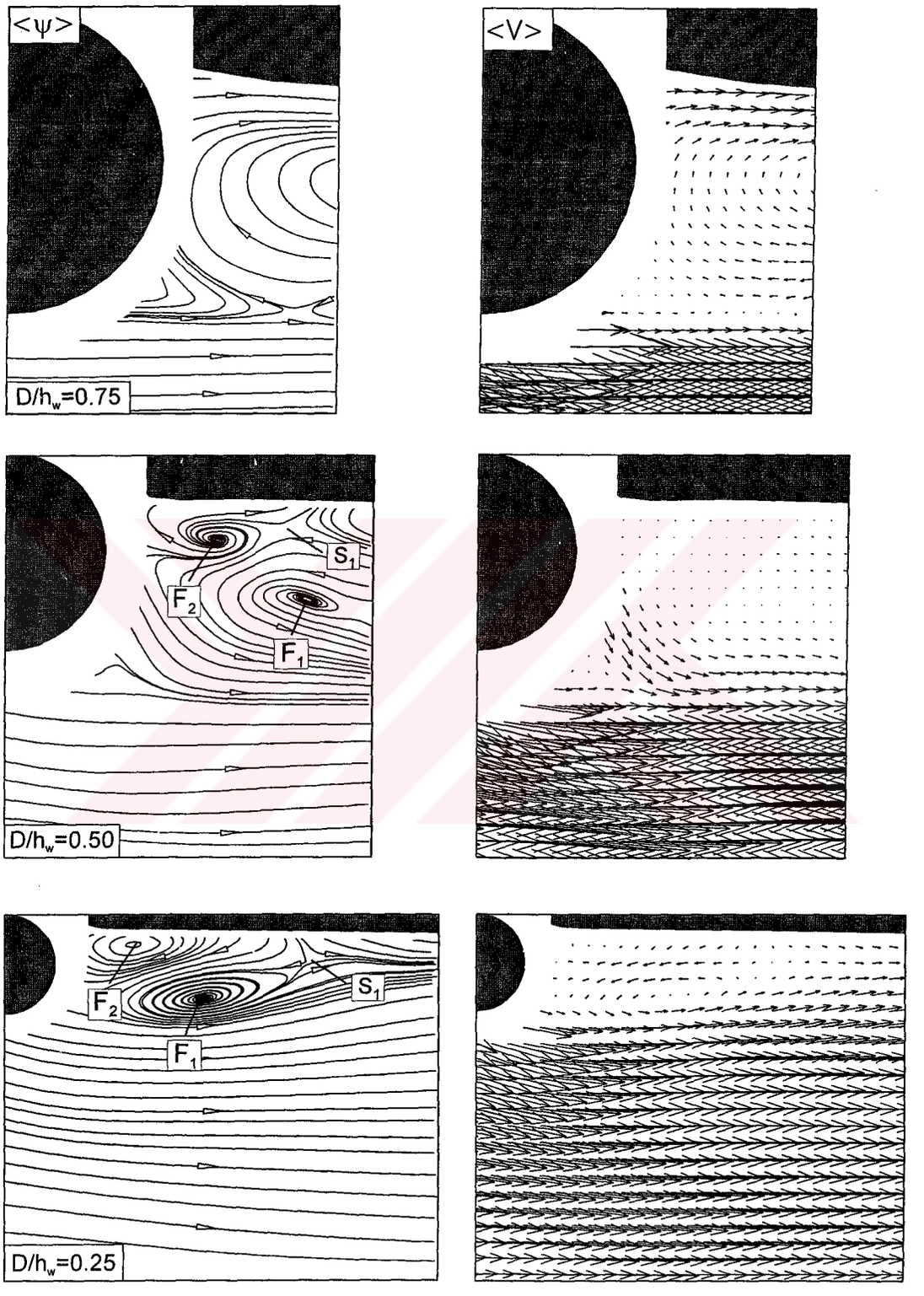

Figure 4.3.2b. Pattrens of time-averaged streamlines <ψ> and velocity vectors <V> in the near-wake region of a horizontal cylinder for D/h_w=0.75, 0.50 and 0.25 respectively.

4.3.3. Patterns of Reynolds Stress in Relation to Patterns of Averaged Velocity, Streamline Topology, and Vorticity

Figure 4.3.3a and 4.3.3b directly compare patterns of Reynolds stress $< u'v' > /U^2$ with corresponding patterns of streamline topology $<\psi>$, averaged velocity $<V>$ and averaged vorticity $<\omega>$. For the case of the intermediate D/h_w = 0.75 and 0.25 cylinder diameters, the field of view was chosen to include the regions of high Reynolds stress and the location of reattachment to the free surface. For the largest cylinder D/h_w = 0.75, it was necessary to employ two fields of view, as indicated in the top set of images of Figures 4.3.3a and 4.3.3b. Furthermore, on each pattern of Reynolds stress, the thick, bold black line indicates the locus of the reattachment streamline.

As shown in the top two sets of images of Figure 4.3.3a, the peak values of Reynolds stress $< u'v' > /U^2$ generally followed the reattachment streamline. In turn, the locus of this reattachment streamline is generally in accord with the peak values of averaged vorticity $<\omega>$ and regions of large gradients of averaged velocity $<V>$. As the location of reattachment is approached, however, the major effects occur. First of all, the magnitude of the maximum value of Reynolds stress decreases from its peak value at a location further upstream. Second, as the reattachment point itself is approached, the locus of the reattachment streamline cuts across contours of constant Reynolds stress $< u'v' > /U^2$ until, at the free-surface, the magnitude of Reynolds stress is very small. In fact, at streamwise locations downstream of reattachment, the magnitude of Reynolds stress, though it decays somewhat, still has substantial values. This feature is consistent for all values of dimensionless cylinder diameter D/h_w. This observation suggests that the instantaneous physics of the flow that is associated with high values of Reynolds stress $< u'v' > /U^2$ at locations upstream of reattachment persists in regions downstream of reattachment. As will be shown in the next section, well-defined vortical structures that are generated in the

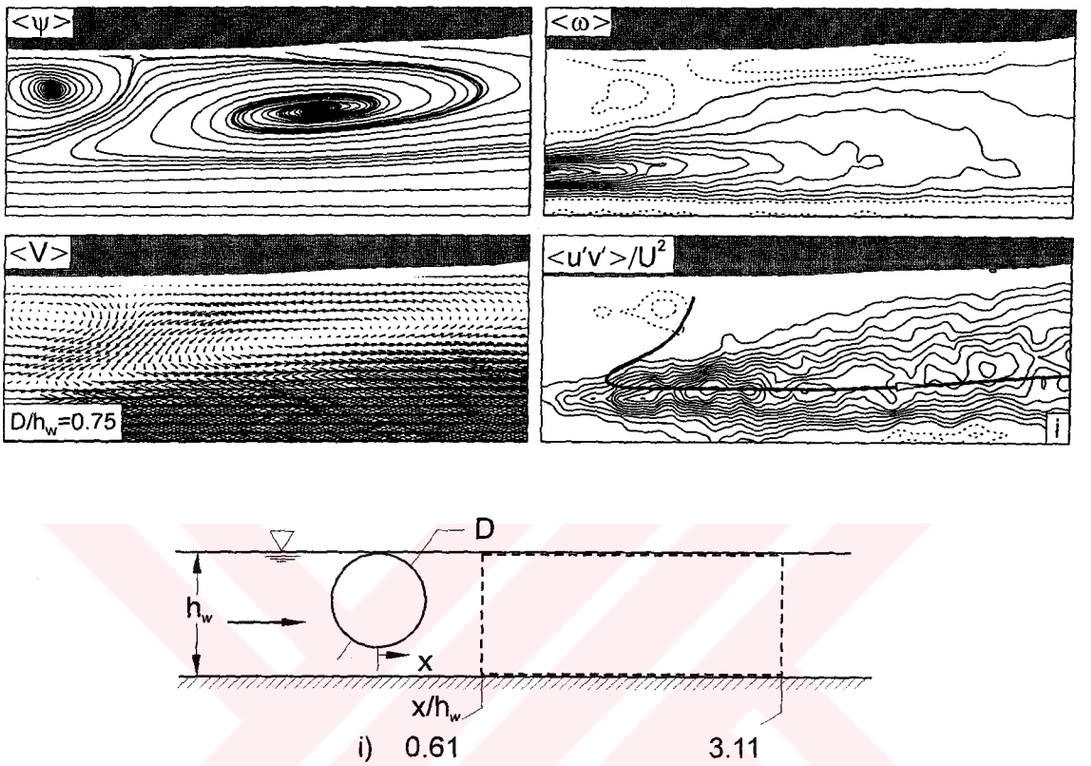

Figure 4.3.3a. Time-averaged streamlines topology $<\psi>$, velocity vectors and patterns of time-averaged vorticity $<\omega>$ and normalized Reynolds stress $<u' v' >/U^2$ downstream of a horizontal cylinder for D/h_w=0.75, 0.50 and 0.25. Sketch shows the location of laser sheet. For all images, minimum and incremental values of vorticity and normalized Reynolds stress are $\omega_{min} = \pm 8$ sec^{-1} and $\Delta\omega$=8 sec^{-1}, $[<u' v' >/U^2]_{min} = \pm 0.005$ and $\Delta[<u' v' >/U^2]$=0.005 respectively.

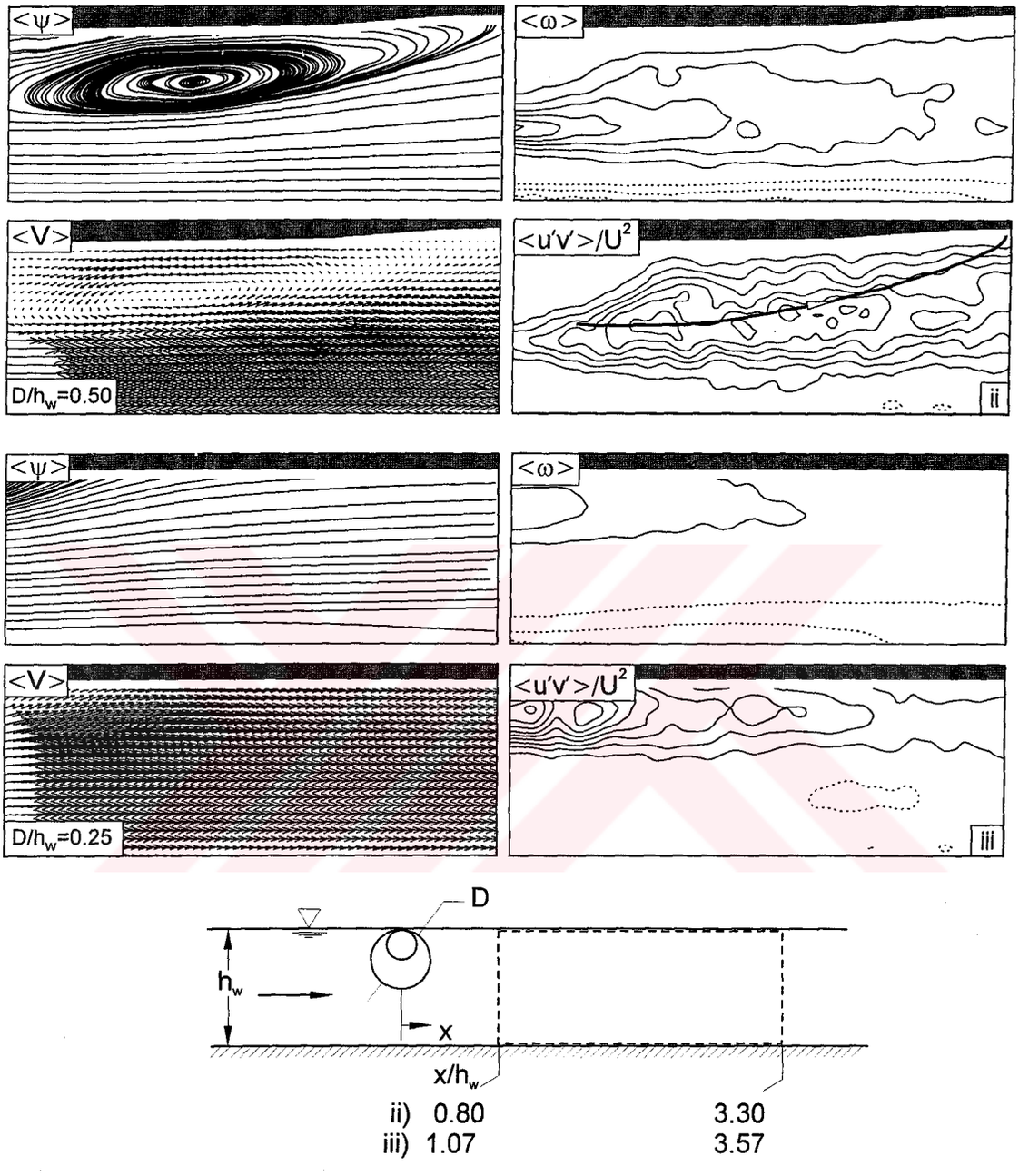

Figure 4.3.3a. Continued.

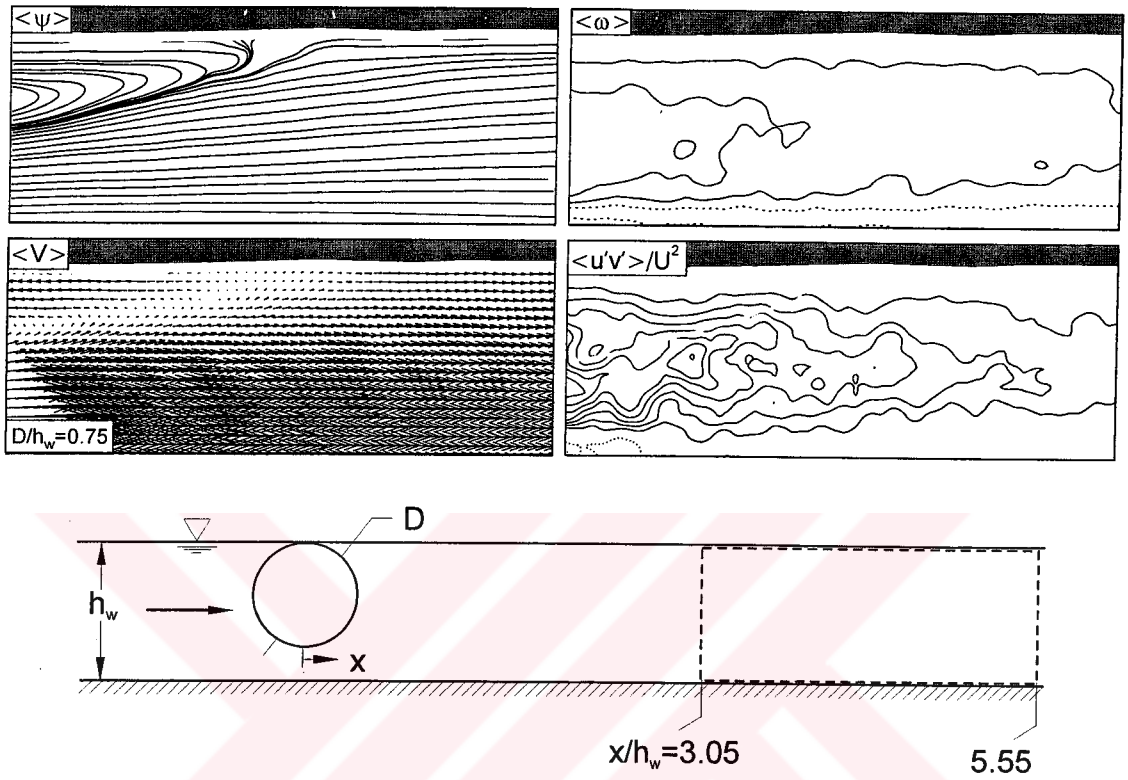

Figure 4.3.3b. Time-averaged streamlines topology $\langle\psi\rangle$, velocity vectors and patterns of time-averaged vorticity $\langle\omega\rangle$ and normalized Reynolds stress $\langle u' v' \rangle/U^2$ further downstream of a horizontal cylinder for D/h_w=0.75. Sketch shows the location of laser sheet. For all images, minimum and incremental values of vorticity and normalized Reynolds stress are ω_{min}= ± 8 sec^{-1} and $\Delta\omega$=8 sec^{-1}, $[\langle u' v' \rangle/U^2]_{min}$= ± 0.005 and $\Delta[\langle u' v' \rangle/U^2]$=0.005 respectively.

shear layer upstream of reattachment move downstream through the reattachment location.

4.3.4. Instantaneous Structure of Velocity, Vorticity and Streamline Topology

Figures 4.3.4a and 4b show, for the largest cylinder diameters $D/h_w = 0.75$ and 0.5 respectively, the instantaneous structure of the patterns of vorticity, streamline topology and velocity for the same fields of view, as shown in Figures 4.3.3a and 4.3.3b. For each field of view, averaged representations, as well as two randomly selected instantaneous images are illustrated. An open gap between bed and lower surface of the cylinder is one fourth of the water level. So, jet-like flow is evident through this open gap. In the last two images of Figure 4.3.4a well-concentrated vortex expands further downstream. A substantial reduction in the level of the vorticity is due to the expansion of core-flow region in the lateral direction as seen in the last two images of Figure 4.3.4a. The location of reattachment point is not clearly defined by the patterns of instantaneous streamlines, but it gives a rough idea where the reattachment streamline merges the free-surface. A similar conclusion can be derived from the instantaneous vector velocity. Flow patterns of vorticity show distinctive, small-scale concentrations of vorticity, as well as larger-scale structures that involve coalescence of these smaller-scales. In fact, these identifiable regions of vorticity exist even at locations well downstream of reattachment. It is therefore evident that the origin of the regions of high Reynolds stress $< u'v' > /U^2$, shown in Figures 4.3.3a and 4.3.3b, are these definable small-scale concentrations of vorticity and their conglomeration.

The corresponding patterns of instantaneous streamline topology show, in most cases, swirl patterns that are associated with the clusters of small-scale vorticity concentrations. It is evident that these patterns of streamline topology $<\psi>$ do not simply represent the perturbation from the averaged topology shown in the top row of each set of images. That is, the location of saddle points adjacent to the free-surface and foci of the large-scale swirl patterns in the averaged topology $<\psi>$ do not appear in any of the instantaneous images.

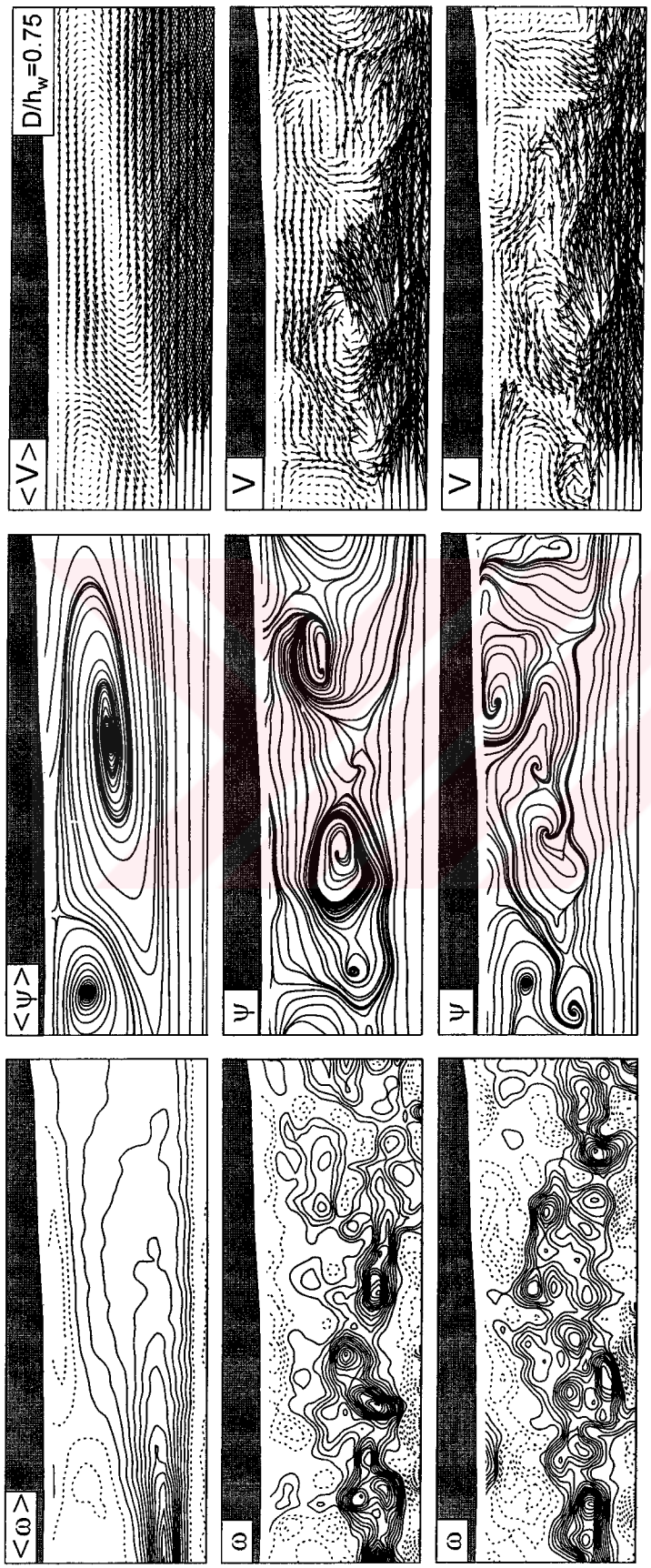

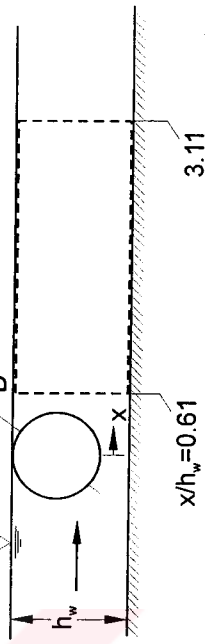

Figure 4.3.4a. Time-averaged and instantaneous streamlines topology ψ, velocity vectors V and patterns of vorticity ω near and further downstream of a horizontal cylinder for D/h_w=0.75. Sketch shows the location of laser sheet. For all images, minimum and incremental values of vorticity are $\omega_{min} = \pm 8$ sec^{-1} and $\Delta\omega$=8 sec^{-1}.

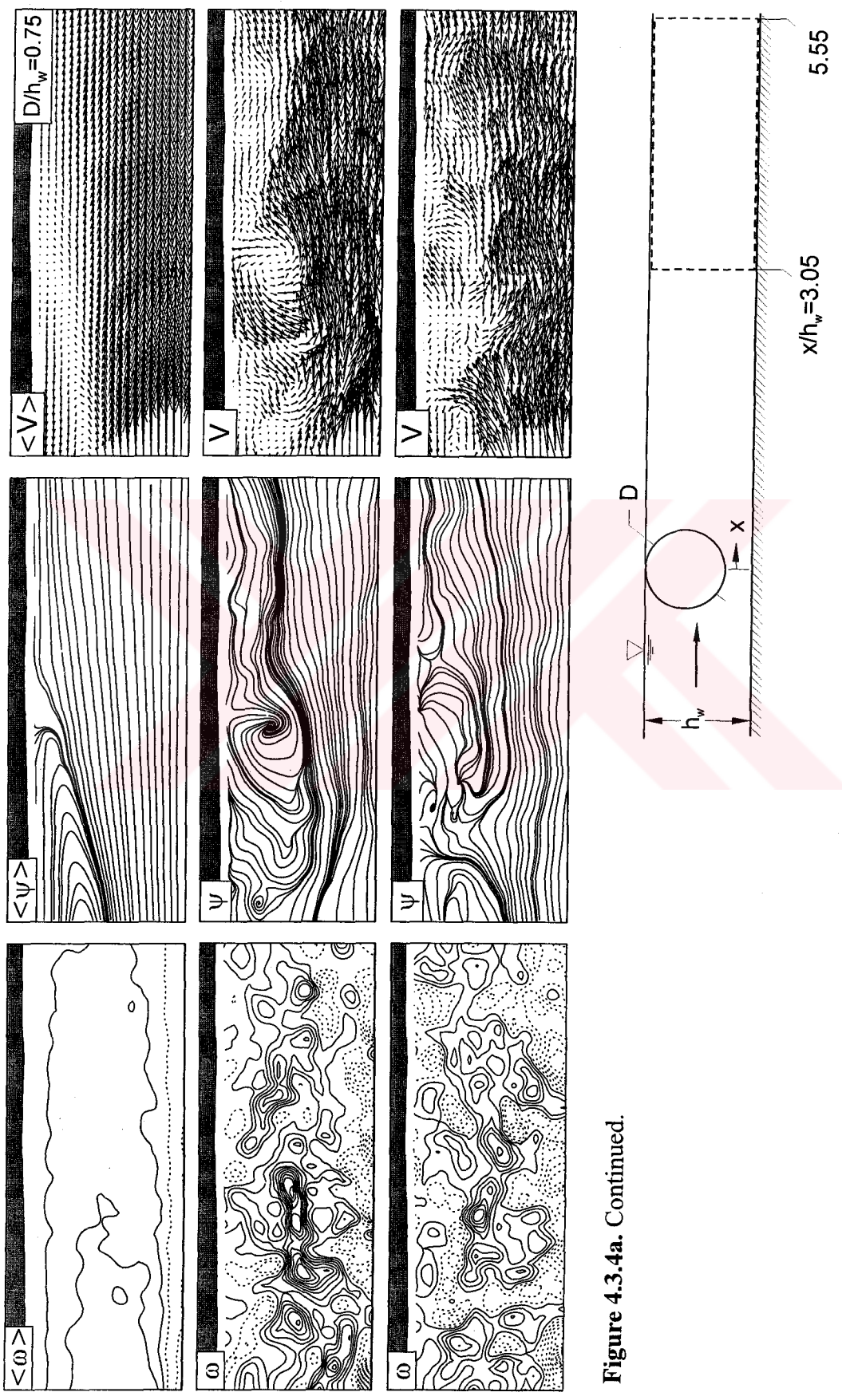

Figure 4.3.4a. Continued.

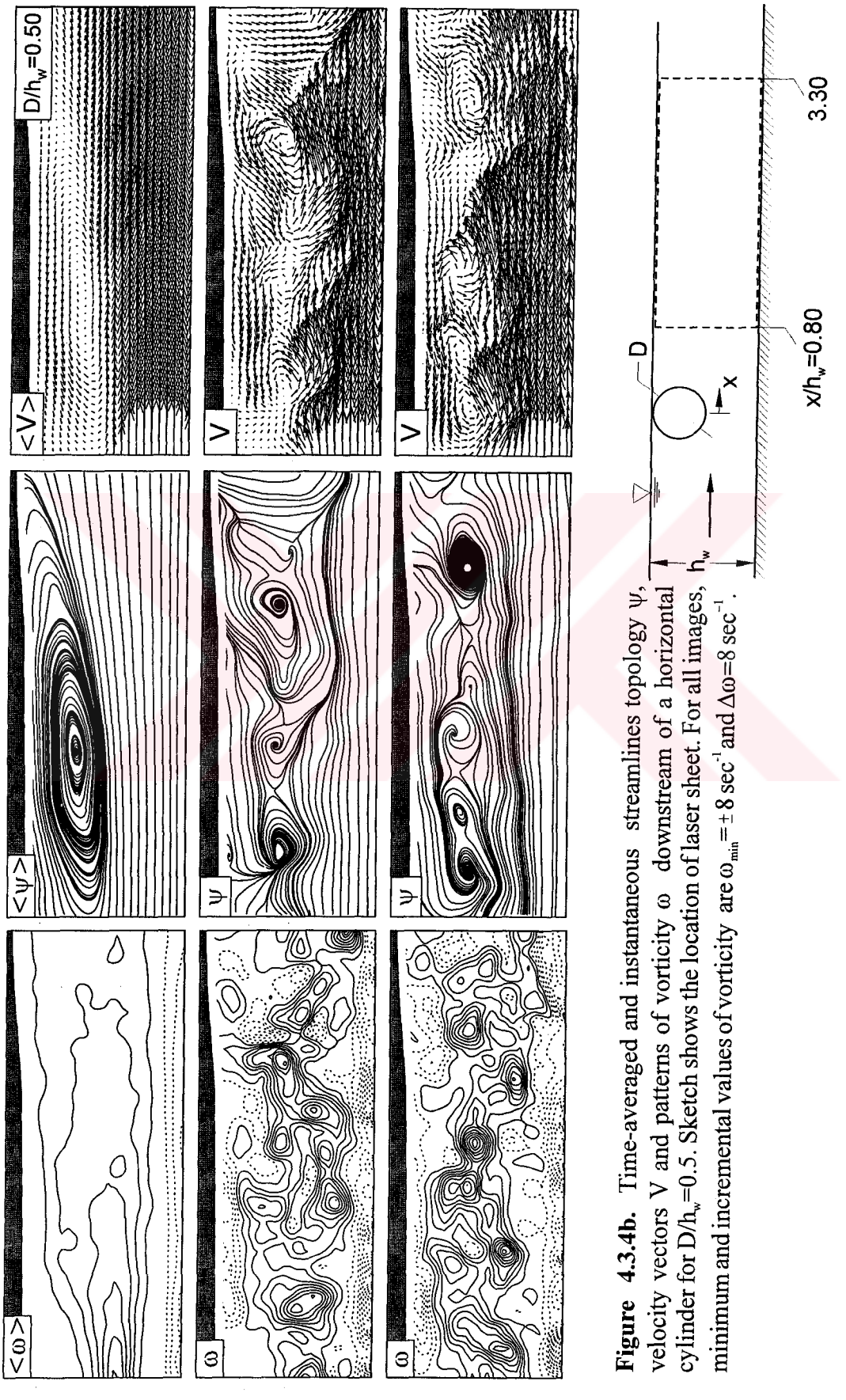

Figure 4.3.4b. Time-averaged and instantaneous streamlines topology ψ, velocity vectors V and patterns of vorticity ω downstream of a horizontal cylinder for $D/h_w=0.5$. Sketch shows the location of laser sheet. For all images, minimum and incremental values of vorticity are $\omega_{min} = \pm 8\ sec^{-1}$ and $\Delta\omega=8\ sec^{-1}$.

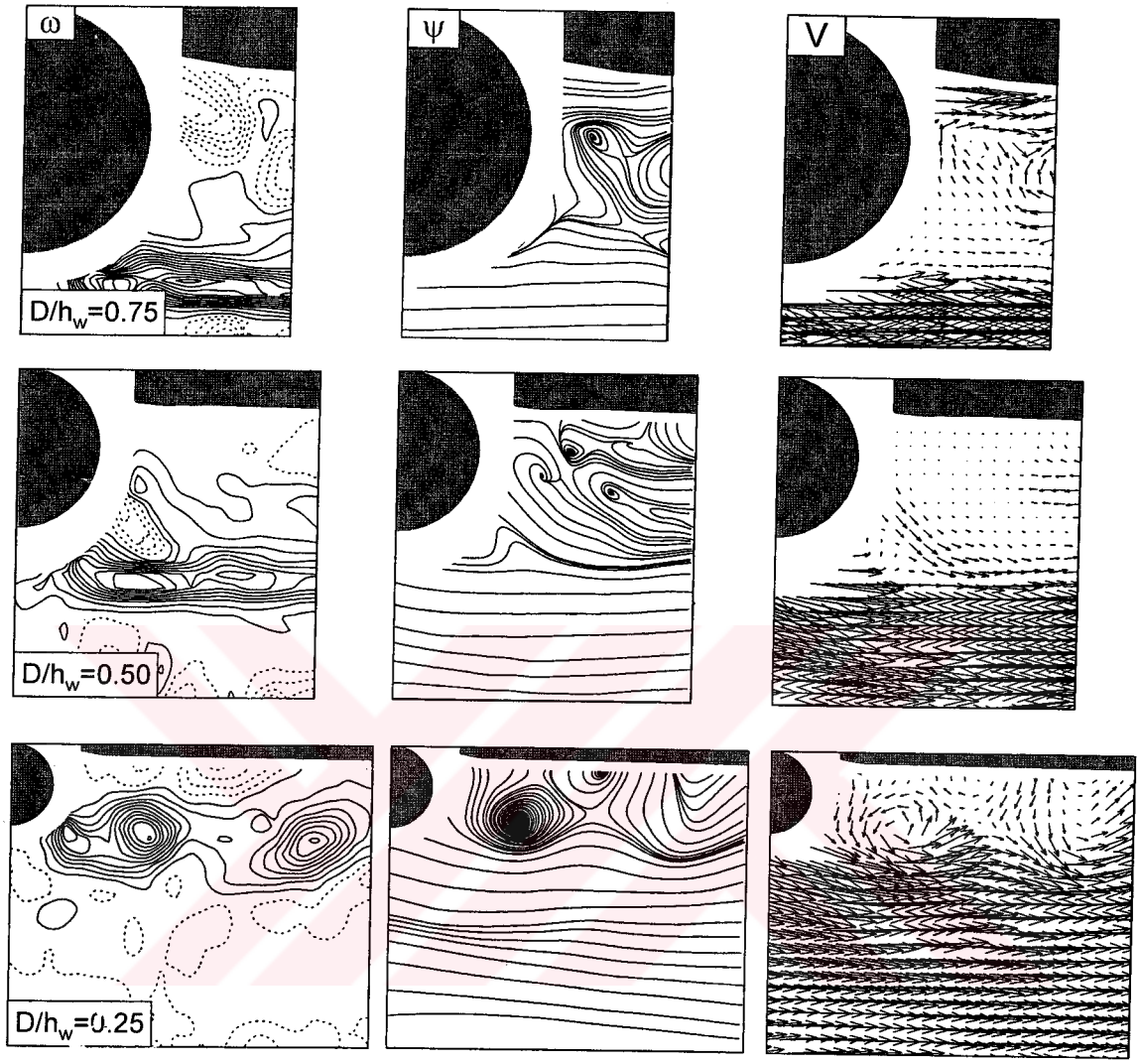

Figure 4.3.4c. Instantaneous streamlines topology ψ, velocity vectors V and patterns of vorticity ω in the near-wake region of a horizontal cylinder for D/h_w=0.75, 0.5, 0.25. For all images, minimum and incremental values of vorticity are $\omega_{min} = \pm$ 8 sec^{-1} and $\Delta\omega$=8 sec^{-1}.

The patterns of instantaneous velocity exhibit large-scale swirl patterns that can occupy the entire region between the interfaces of the separated shear layer along the edge of the reattachment zone all the way to the free-surface. In fact, these large-scale swirl patterns persist through and downstream of the region of time-averaged reattachment of the flow. This effect is particularly evident at locations near and downstream of reattachment of the set of images corresponding to $D/h_w = 0.5$ in Figure 4.3.4b and 4.3.4c. For the largest cylinder diameters $D/h_w = 0.75$ and 0.5 respectively, an elongated shaped instantaneous vortices occur immediately adjacent to the lower surface of the cylinder. On the other hand, for the smallest cylinder diameter $D/h_w = 0.25$ a circular shaped vortices appear in close region of the lower surface of the cylinder.

4.3.5. Three-Dimensional Structure of Flow

In this part of the work, the variations of streamwise vorticity in the longitudinal direction in the cross-plane are examined. The cross-flow planes are selected as stations along the streamwise direction. These inverted position of cross-flow planes allowed the acquisition of instantaneous images of the velocity over the fields of view as indicated in Figure 4.3.5a.

Figure 4.3.5a gives an overview of patterns of instantaneous velocity, streamline patterns and vorticity at various cross-sectional cuts A through D, which extend from the region of the separated shear layer immediately downstream of the cylinder to a location near flow reattachment. At all cross-sectional locations, the patterns of velocity vectors show regions of localized swirl. They are associated with well-defined concentrations of streamwise vorticity (ω_x).

At location AA, the pattern of streamwise vorticity is centered at an elevation from the bottom surface corresponding approximately to the locus of maximum spanwise vorticity ω_y. In other words, these structures clearly arise in the separated shear layer from the cylinder. They have a spanwise spacing varying approximately from 0.62 D to 0.2 D. The peak values of vorticity of the streamwise concentration ω_x is 68.33 sec^{-1}. These values compare with the peak levels of ω_y vorticity shown

in the two instantaneous images in the top of Figure 4.3.4a, which have peak values ranging from 162.5 to 199.2 sec^{-1}. At locations further downstream, along the recirculation zone and in the vicinity of reattachment, i.e., sections BB through DD, the concentrations of vorticity ω_x occupy regions successively closer to the free-surface until, at section DD, pronounced concentrations of streamwise vorticity of alternating sign occur immediately beneath the free-surface. The average spanwise spacing in these concentrations is of the order of 0.40 D. Furthermore, the peak values of vorticity over the entire section DD are in the range of 50.1 to 26.5 sec^{-1}. Viewing the patterns of streamwise vorticity ω_x of the entire set of images in the bottom row of Figure 4.5.5a, the characteristic spanwise spacing is in the range from 0.7 D to 0.2 D. It is therefore concluded that the scale of the streamwise vorticity concentrations ω_x is relatively unaffected by the cross-sectional location along the reattachment zone. Furthermore, the peak values of vorticity ω_x show only a mild decrease in the region of the shear layer immediately downstream of separation from the cylinder, i.e. at DD.

Further features of the three-dimensionality at cross-sections AA and DD are shown in Figure 4.3.5b, in the form of streamline topology and patterns of velocity vectors over the respective cross-sections. At location AA, the predominant features are relatively large velocity vectors in the downward direction, due to the entrained flow demanded by the developing shear layer from the surface of the cylinder. The corresponding pattern of streamlines shows a series of nodal lines at an elevation corresponding to the edge of the vorticity layer ω_y that separates from the surface of the cylinder. This nodal line involves spatially periodic occurrence of saddle points S_a and S_b. Furthermore, at the free-surface, the streamlines tend to merge into local nodes of the form indicated by N_b.

At location DD, however, such nodal lines, nodes and saddle points no longer occur. The flow is generally directed towards the free-surface, due to the process of reattachment indicated by the quasi-two-dimensional streamline pattern in the top set of images. Occurrence of foci at F_a and F_b represent the three-dimensionality at this section.

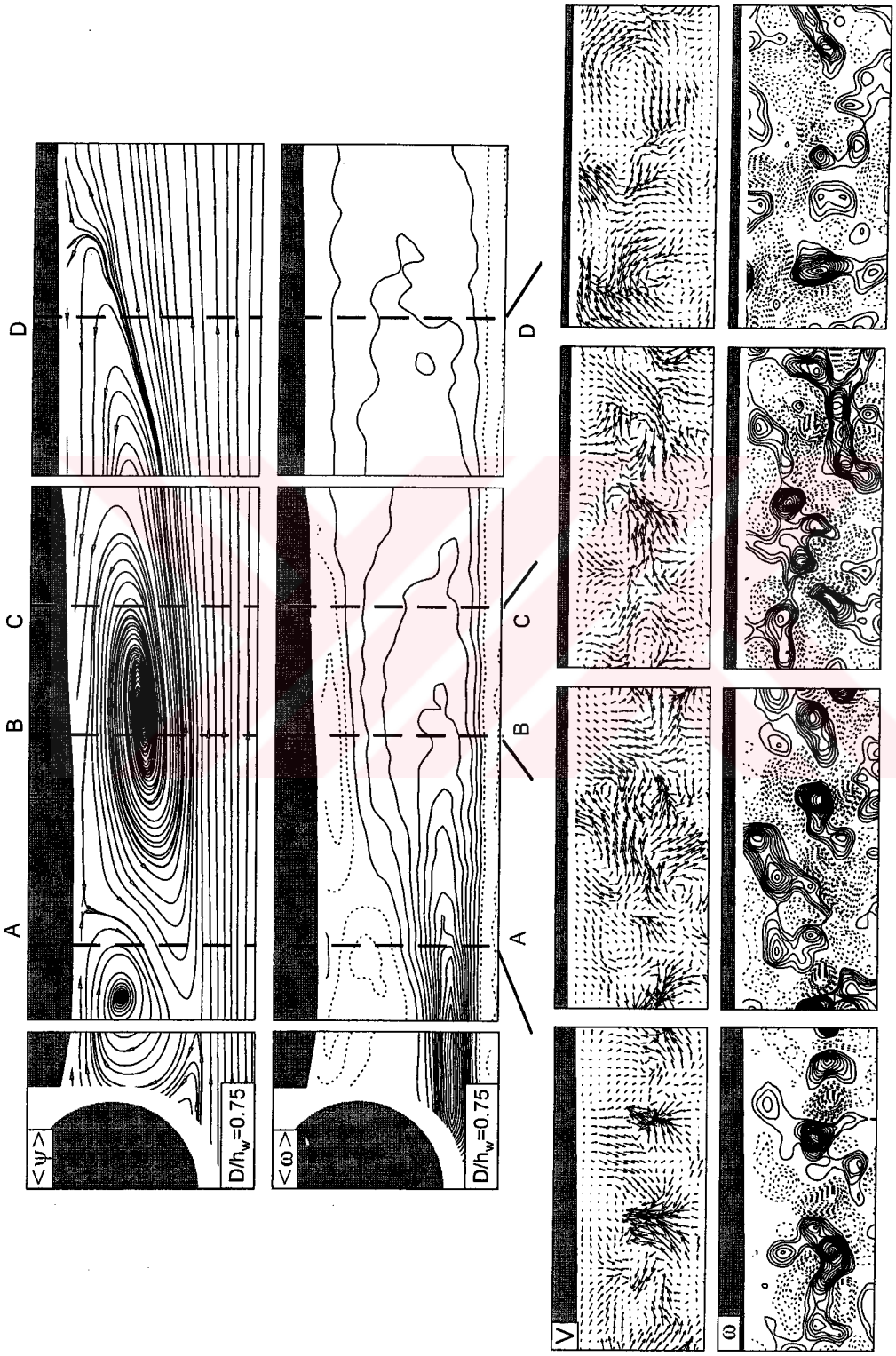

Figure 4.3.5a. Overview of patterns of instantaneous velocity V and streamwise vorticity ω_x at various cross-sectional cuts A through D, which extend from the region of the separated shear layer immediately downstream of the horizontal cylinder to a location near flow reattachment for $D/h_w=0.75$. For all images, minimum and incremental values of vorticity are $\omega_{min} = \pm 4\ sec^{-1}$ and $\Delta\omega=4\ sec^{-1}$.

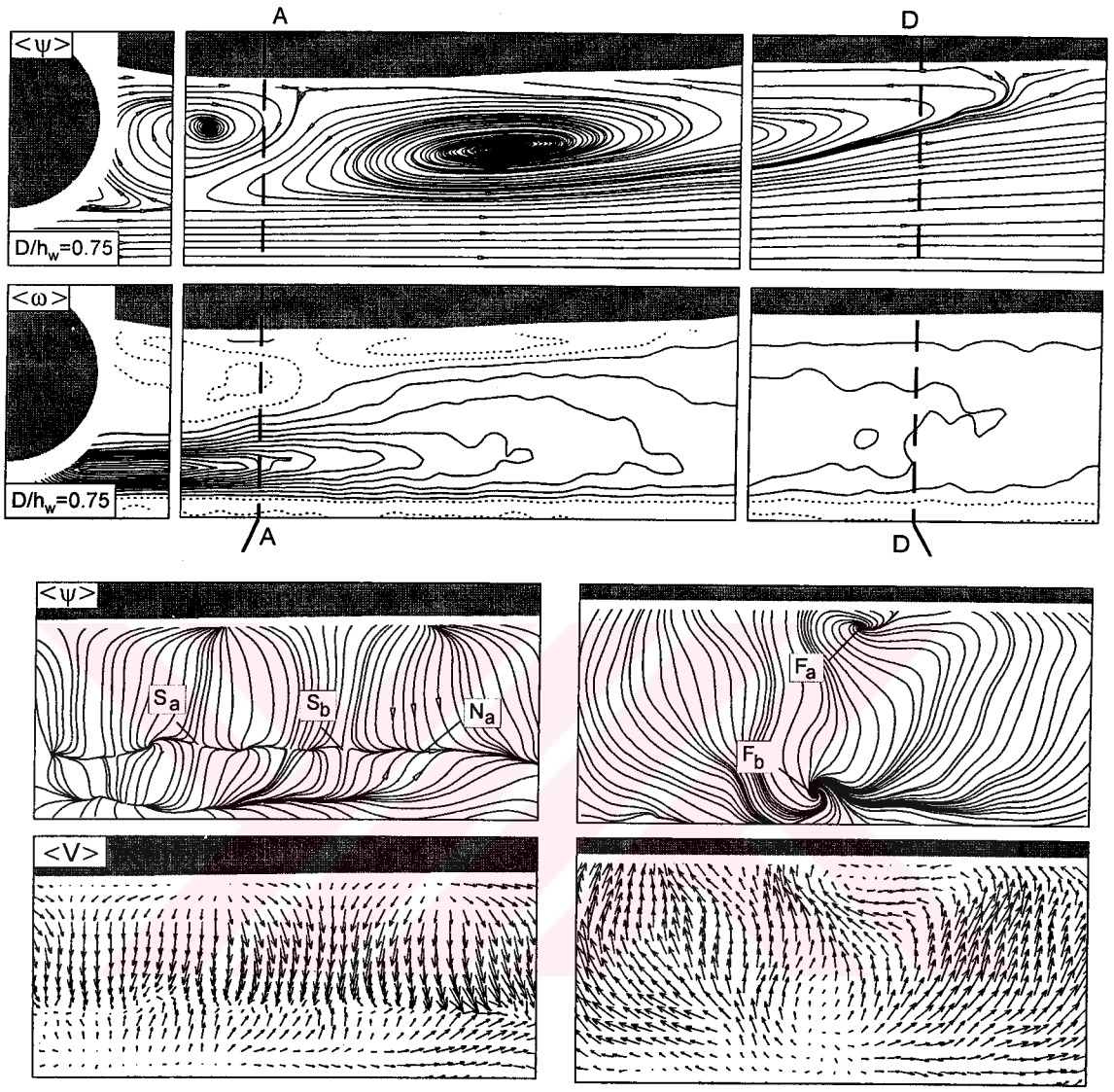

Figure 4.3.5b. Overview of patterns of time-averaged velocity <V> and streamlines <ψ> at cross-sectional A and D, which extend from the region of the separated shear layer immediately downstream of the horizontal cylinder to a location near flow reattachment for D/h_w=0.75.

4.3.6. Concluding Discussion

The diameter of cylinder was varied in small increments in order to determine the values that exhibited major changes in the near-wake patterns. For the cases of D/h_w = 0.75, 0.5 and 0.25 cylinder diameters indicate that the streamline topology in the very near-wake of each cylinder is a strong function of the cylinder diameter and the Froude number $U_{max}/\sqrt{gD}$ =0.41, 0.50 and 0.71 associated with dimensionless cylinder diameters D/h_w = 0.75, 0.5 and 0.25 respectively. The counter-flow in the upstream direction along the mixing layer exists where secondary recirculation cell with a focus F_1 occurs. On the other hand, the primary recirculation bubble as indicated by streamline topology in Figure 4.3.2a shows that the direction of rotation opposes the direction of secondary recirculation cell. However, an entrainment process between free-surface and the mixing layer occurs satisfying the necessary flow transfer between core and recirculating flows. The counter-flow rotation in the direction of upstream occurs for only the D/h_w = 0.75 case. For other cases of the cylinder diameters D/h_w = 0.5 and D/h_w = 0.25, both secondary and primary recirculting bubbles have the same direction of the mixing layer. All recirculating bubbles F, F_1 and F_2 rotate in clockwise direction. It can be concluded that the magnitude of entrainment process is higher when the counter-flow direction opposes the direction of core flow along the mixing layer as seen in the case of D/h_w = 0.75. A high rate of entrainment process may increase the unsteadiness of the flow. The magnitude of jet velocity increases by increasing the diameter of the cylinder causing concentrated positive vorticity. The mixing layer in the downstream region of the flow is dominated by the positive vorticity as seen in Figure 4.3.2a. For the case of D/h_w = 0.75, a jet-like flow, which glides over the top surface of the cylinder, is evident immediately beneath the free-surface. This surface jet-like flow stimulates the secondary recirculation bubble which rotates in clockwise direction as indicated by streamline topology and vector velocity.

The Reynolds stress $< u'v' > /U^2$ values are the greatest at a location in the front portion of the vorticity concentration. A high level of Reynolds stress fluctuations exist along the shear layer. Entrainment process may be the cause of the high rate of Reynolds stress fluctuations. Instantaneous physics of flow that is associated with high values of Reynolds stress $< u'v' > /U^2$ along the shear layer persists further downstream of the reattachment point. After a certain amount of distance the magnitude of Reynolds stress $< u'v' > /U^2$ diminishes because of no entrainment process. Instantaneous structure of the pattern of vorticity indicates that a well-concentrated vorticity occurs along the shear layer. A substantial deterioration in the level of the vorticity is due to the divergence of the core flow region. The variations of streamwise vorticity in the longitudinal direction in the cross-flow plane are examined. Contours of vorticity and distribution of velocity vectors also indicate that high concentration of vorticity occurs along the shear layer. A substantial deterioration in the level of the vorticity is due to the divergence of the core flow region.

Variations of streamwise vorticity in the longitudinal direction in the cross-flow plane are examined. Contours of vorticity and distribution of velocity vectors also indicate that high concentration of vorticity occurs along the shear layer. Viewing all images together show that concentrated vortices gradually expand and slightly diminish while flow proceeds downstream in the longitudinal direction.

5. CONCLUSIONS AND RECOMMENDATIONS

In this study, vortex formation of a vertical cylinder in shallow water and its control was investigated. In order to control vortex formation behind cylinder a narrow transverse strip of roughness elements was placed behind the cylinder on the bottom surface of water channel. A technique of high-image-density particle image velocimetry (PIV) was employed to obtain global, instantaneous representations of the flow patterns, which lead to phase- and time-averaged patterns of streamline topology and Reynolds stress on planes at and above the bed. The wake structure of a horizontal cylinder submerged beneath the free-surface was also investigated.

5.1. Vortex Formation from a Vertical Cylinder in Shallow Water Flow

The turbulent boundary layer extends through the whole water depth is one of the important characteristics of shallow water layer. Because of that, the set of tests were conducted to make sure that fully developed flow exists in the test section. The local mean velocity distribution measured by PIV agrees well with previous results taken from the literature.

The formation of a large-scale Kármán vortex in shallow water, as visualized by a dye marker, involves upward oriented axial flow through the center of the vortex. This vortex eventually leads to a horizontal vortex that induces significant distortion of the free-surface. In shallow water layer, however, the effect of the specified distance between the bed and the free-surface is associated with three-dimensional mechanism that gives rise to a horizontally oriented vortex which is evident immediately beneath the free-surface for a significant portion of the Kármán vortex cycle.

Despite the existence of the three-dimensional mechanism visualized by a dye marker, the instantaneous, sectional streamline topology and vorticity patterns in horizontal planes, at the bed and at various locations above the bed, exhibit several features that are typically associated with the topology of the bluff body wakes of large spanwise extent. A number of distinctive characteristics are, however, evident in the topology at the bed.

Furthermore, the locations of the saddle point at various phases of the oscillation cycle are correlated with the patterns of vorticity in the near wake region. This correlation includes the relationship between the occurrence or nonoccurrence of well-defined, distinct concentration of vorticity in relation to foci of the streamline patterns.

Comparison of the streamline topology and patterns of vorticity at elevations at and above the bed show that a common saddle point can be identified at approximately the same spatial position in the near wake for all elevations. With increasing elevation above the bed, the spanwise extent of the pattern of swirling streamlines increases, which is in accord with more broadly distributed patterns of the vorticity cluster in the near wake region. Furthermore, using the common saddle point as a phase reference, the streamline pattern above the bed shows reattachment to the base, which encloses a well-defined focus. At the bed, this pattern does not exist.

All of the foregoing features of the averaged topology are correlated with patterns of averaged vorticity and Reynolds stress. Near the bed, the vorticity layers remain relatively narrow and rapidly drawn toward the plane of symmetry of the base, relative to the patterns at elevations above the bed. Regarding the patterns of Reynolds stress near the bed, well-defined clusters of Reynolds stress close to the base are not evident. Such clusters do occur, however, at the midplane of the shallow water layer in the present investigation. They are well-known feature of wake from cylinders of large spanwise extent. Furhermore, near the bed, additional patterns of Reynolds stress appear exterior to the near wake; they are due to the necklace (horseshoe) vortex originating from the inflow-cylinder interaction.

5.2. Control of Vortex Formation From a Vertical Cylinder in Shallow Water: Effect of Localized Bed Roughness

The effect of localized surface roughness on the vortex formation from a cylinder in shallow water has been characterized. In contrast to previous approaches to control the near-wake structure of vortex shedding from a cylinder of large

spanwise extent, involving various types of surface roughness along the span of the cylinder, the present study has aimed to determine the global sensitivity of the near-wake structure to confined roughness on the bed (bottom) surface. Instantaneous wholefield patterns of the flow structure, along with averaged representations, are provided for planes near the bed and at the midplane of the shallow water layer. These types of images allow determination of the degree to which the localized surface roughness alters not only the region of the wake downstream of the roughness elements, but also the possible modifications in regions upstream of the roughness.

The location of the upstream saddle point adjacent to the base of the cylinder is sensitive to the height of the roughness, but the location of the downstream saddle point varies more substantially with roughness height; for the latter, large downstream displacements of the saddle point can be attained for the largest height of roughness. Broadly similar, but less pronounced, trends are evident for the averaged topology at the midplane; for the limiting case of small roughness, however, changes of the averaged streamline topology are barely discernible in this region of the flow.

Patterns of Reynolds stress, at both near and the midplane, generally show decreasing peak values with increasing height of the roughness. In fact, the smallest roughness height yields a substantial reduction in the Reynolds stress level in the very near-wake, both near the bed and at the midplane. Downstream of the roughness elements, near the bed, the overall pattern of Reynolds stress concentrations, as well as the peak values, is altered substantially near the bed, even for the smallest value of roughness height. At the midplane, the overall form of the pattern of Reynolds stress concentrations remains similar, but the loci of the extrema of the concentrations is displaced downstream with increasing roughness height.

It is demonstrated that even the smallest roughness height clearly attenuates the onset of large-scale, Kármán-like vortex formation in the region close to the base of the cylinder, relative to the case of no roughness. These overall features are evident not only near the bed but also at the midplane.

From a conceptual standpoint, it is known that the occurrence of large-scale vortex formation from a cylinder in a shallow water layer, or for that matter from a cylinder of infinite spanwise extent, arises from a global (absolute) instability of the near-wake region, as evident in the citations given in the Introduction. The present investigation is a first attempt to control the large-scale vortex formation using localized surface roughness elements of relatively small height on the bed of a shallow layer. It is evident that this localized roughness has a pronounced effect on the entire domain of the near-wake, apparently due to interference with the global instability that normally gives rise to Kármán vortex formation close to the base of the cylinder. It is, however, difficult to link the interference effects of the roughness elements to the concept of a global (absolute) instability of the near-wake. The former is a three-dimensional mechanism, while the concept of a global instability is inherently two-dimensional. The primary consequence of the roughness elements may be to enhance the interaction between the fluid and the bed surface, leading to attenuation of the vortex shedding, in the fashion described by Grubisic et al. (1995).

5.3. Flow Structure From a Horizontally Positioned Cylinder in Shallow Water

The aim of the investigation in this part of the work is to identify the possible states of the wake when the cylinder is submerged horizontally beneath the free-surface of the shallow water. The upper surface of the cylinder was adjusted in order to be coincident with the free-surface. The diameter of the horizontal cylinder was gradually increased in order to determine the values that exhibited major changes in the near-wake patterns. Sheridan and Rockwell (1997) placed a cylinder horizontally beneath a free-surface of a deep water flow. They observed that small changes of the distance between the upper surface of the cylinder and free-surface cause profound alterations in the near-wake patterns compared to the wake structure of a fully-submerged cylinder.

The diameter of the cylinder was varied in small increments in order to determine the values that exhibited major changes in the near-wake patterns. For the cases of t D/h_w = 0.75, 0.5 and 0.25 cylinder indicate that the streamline topology in

the very near-wake of each cylinder is a strong function of the cylinder diameter and the Froude number $U_{max}/\sqrt{gD}$ =0.41, 0.50 and 0.71 associated with dimensionless cylinder diameter D/h_w = 0.75, 0.5 and 0.25 respectively. Considering the present data analysis, only the streamline topology indicates the reattachment point to the free-surface clearly. Comparison of the results of three different cylinder diameters reveals that the magnitude of the jet-like flow which occurs between the lower surface of the cylinder and channel bed affect the whole characteristics of flow downstream of the cylinder. It is also obvious that jet-like flow originating from the top surface of the cylinder alters the behavior the wake flow region.

The saddle points first appear in the upstream of the primary recirculating bubble for the largest value of D/h_w=0.75. But the saddle point moves further downstream of the primary recirculating bubble for the smallest value of D/h_w=0.25. The average vorticity $<\omega>$ rapidly decreases with decreasing the values of D/h_w. As the core flow region i.e. the jet-like flow cross-section expands while it moves further downstream. Contours of averaged vorticity $<\omega>$ also diverge as the flow approaches to the point which reattaches the free-surface.

Average streamline topology and patterns of velocity vectors over the cross-planes that are placed upstream of the reattachment point indicate that the flow is three-dimensional. Overview of patterns of time-averaged velocity vector clearly indicate that entrainment flow process occurs between separated flow and core flow region across the shear layer. The scale of the streamwise vorticity concentrations ω_x is relatively unaffected by the cross-sectional location along the reattachment zone.

5.4. Recommendations for Future Work

The present work focused on flow past a vertical and horizontal cylinders in turbulent shallow water. Results are presented showing the vortex structures in the wake of a cylinder placed vertically and horizontally in close proximity to the free-surface.

From physical standpoint, it is necessary to account both the destabilizing effect of transverse shear across the wake and the stabilizing influence of bed

friction. As future studies, an experimental investigations with PIV system can be undertaken to study the effects of roughness over a complete bed surface on the structure of turbulent boundary layers in shallow water. Similar study was carried out by Tachie et al. (2000) using a Laser Doppler Anemometry (LDA) in shallow water flow for three different types of rough surfaces as well as a hydraulic smooth surface. But, it is not possible to identify wake flow region with a single point measurement device. In order to verify flow past a cylinder in a great detail one should use PIV measurement technique. Perforated plate and a wire mesh sheet can be used as a rough surface. Also, sand grain roughness can be coated over the channel bottom surface. Here, the size of roughness can be varied in order to see the profound effect of surface roughness on the inner and outer region of turbulent boundary layer. By altering Reynolds numbers it will be valuable to study laminar flow for the same geometry.

In order to compare the results of the PIV technique with the Critical Point Theory, shallow water flow should be kept laminar on smooth bed surface. The basic concepts of the Critical Point Theory can also be obtained by a technique of high-image density Particle Image Velocimetry applied to laminar shallow water flow. Here, the introduction of notion such as bed friction lines, critical points, separation (or attachment) lines, hence and hence, topological rules allowed a consistent description of flow fields.

It is known that separation point on the cylinder surface varies with Reynolds number. So, it could also be good idea to vary Reynolds number in the range of $1<Re<10^6$. In order to see a break point of boundary layer on the cylinder surface moving backward and forward, a digital camera should be focused on a smallest frame of flow field as much as possible.

Effect of cylinder oscillation on the wake of the cylinder in shallow water flow may also be studied. Here, the frequency of perturbation can be an important parameter. For example, the frequency of perturbation that correspond naturel frequency of shear layer may change vortical pattern in a different manner. Control of vortex shedding around the cylinder in shallow water can also be a interesting subject on engineering application.

REFERENCES

ADRIAN, R.J., 1986. Image shifting technique to resolve directional ambiguity in double pulsed velocimetry. Applied Optics, Vol. 25, pp. 3855-3858.

ADRIAN, R.J., 1988. Statistical properties of particle image velocimetry measurements in turbulent flow. Laser Anemometry in Fluid Mechanics. Ed. R.J. Adrian et al, Lisbon, pp. 115-129.

ADRIAN, R.J., 1991. Particle-Imaging techniques for experimental fluid mechanics. Annual Review of Fluid Mechanics. Vol. 23, pp. 261-304.

ALVAIN , V. and Chu, V. H., 1985. Turbulent exchange flow in shallow compound channel. Proceeding of the 21th I.A.H.R Congress, Melbourne, pp 19-23.

AKILLI, H. and ROCKWELL, D., 2002. Vortex formation from a cylinder in shallow water. Physics of Fluids, Vol. 14, No.9, pp. 2957-2967.

ALTAI, W., ZHANG, J. and CHU, H. V., 1999. Shallow turbulent flow simulation using two-length-scale model. Journal of Engineering Mechanics, Vol. 125, No. 7, pp:.780-788.

BABARUTSI, S., GANOULIS, J. and CHU, V. H., 1989. Experimental Investigation of shallow recirculating flows. . Journal of Hydraulic Engineering, Vol. 115, No. 7, pp. 906-923.

BABARUTSI, S. and CHU, V. H., 1991. Dye-concentration Distribution in shallow recirculating flows. Journal of Hydraulic Engineering, Vol. 117, No. 5, pp. 643-659.

BALACHANDAR, R., CHU, V.H. and ZHANG, J., 1997. Experimental study of turbulent concentration flow field in the wake of a bluff body. Journal of Fluid Engineering, Vol. 199, pp. 263.

BALACHANDAR, R., TACHIE, M. F. and CHU, V.H., 1999. Concentration profiles in shallow turbulent wakes. Journal of Fluid Engineering, Vol. 121, pp. 34-43.

BALACHANDAR, R., RAMACHANDRAN, S. and TACHIE, M. F., 2000. Characteristics of shallow turbulent near wakes at low Reynolds number. Journal of Fluid Engineering, Vol. 122, pp. 302-308.

BALACHANDAR, R. and TACHIE, M. F., 2001. A study of boundary layer-wake interaction in shallow open channel flows. Vol. 30, pp. 511-521. Experiments in Fluids.

BERS, A. 1975. Linear waves and instabilities. In Physique des Plasmas. Ed. C. Dewitt and J. Peyraud, pp. 117. Gordon and Breach.

BLOOR, M. S., 1964. The transition to turbulence in the wake of a circular cylinder. Journal of Fluid Mechanics, Vol. 19, pp. 290-304.

BRIGGS, R. J. 1964. Electron-stream interaction with Plasmas. MIT Press.

CARTER, W. R., EINSTEIN, A., HINDS, J., POWELL, R. W. and SILBERMAN, E. 1963. A.S.C.E. Task force on friction factors in open channels. Journal of Hydraulic Division, ASCE, Vol. 89 (HY2), pp. 97-143.

CHEN, D. and JIRKA H., 1995. Experimental study of plane turbulent wakes in a shallow water layer. Fluid Dynamics Research, Vol. 16, pp. 11-41.

CHEN, D. and JIRKA H., 1997. Absolute and convective instabilities of plane turbulent wakes in a shallow water layer. Journal of Fluid Mechanics, Vol. 338, pp. 157-172.

CHEN, D. and JIRKA H., 1998. Linear stability of turbulent mixing layers and jets in shallow water layers. Journal of Hydraulic Research, Vol. 36, pp. 815-829.

CHEN, D. and JIRKA H., 1999. LIF study of plane jet bounded in shallow water layer. Journal of Hydraulic Engineering, Vol. 125, No. 8, pp. 817-826.

CHU, H. V., WU, J.-H, KHAYAT, R. E., 1991. Stability of transverse shear flows in shallow open channels. Journal of Hydraulic Engineering, Vol. 117, No. 10, pp. 1370-1388.

CHU, H. V., and BABARUTSI, S., 1988. Confinement and bed-friction effects in shallow turbulent mixing layers. Journal of Hydraulic Engineering, Vol. 114, No. 10, pp. 1257-1274.

CHYU, C., 1995. A study of the near-wake structure from a circular cylinder. Ph.D. Thesis, Lehigh University Mechanical Engineering and Mechanics, Bethlehem, PA, USA.

CHYU, C. and ROCKWELL, D., 1996. Evolution of patterns of streamwise vorticity in the turbulent near wake of a circular cylinder. Journal of Fluid Mechanics, Vol. 320, pp. 117-137.

ÇETİNER, O., 1998. Flow structure and loading due to an oscillating cylinder in steady current. Ph.D. Thesis, Lehigh University Mechanical Engineering and Mechanics, Bethlehem, PA, USA.

DÉLERY, J. M., 2001. Toward the education of Three-Dimensional Separation. Annu. Rev. Fluid Mech. Vol. 33. pp. 129-154.

DENIZ, D. and STAUBLI, T. H., 1997. Oscillating rectangular and octagonal profiles: interaction of leading and tariling-edge vortex formation," Journal of Fluids and Structures, Vol. 11, pp. 3-31,

DRACOS, T., GIGER, M. and JIRKA, G. H., 1992. Plane turbulent jets in a bounded fluid layer. Journal of Fluid Mechanics, Vol. 241, pp. 587-614.

EL-GHUSEN, M. A., MAZEN M. A., MARTINUZZI, R. J., 1998. A experimental investigation of turbulent flow around surface-mounted pyramid in a thin boundary layer. Proceedings of FEDSM'98: 1998 ASME Fluids Engineering Division Summer Meeting, June 21-25.

GERRARD, J. H., 1978. The wakes of cylindrical bluff bodies at low Reynolds number. Phil. Trans. R. Soc. London A, Vol. 288, pp. 351-382.

GYR, A. and SCHMID, A., 1997. Turbulent flows over smooth erodible sand beds in flumes. Journal of Hydraulic Research, Vol. 35, pp. 525-544.

GRUBIŠIĆ, V., SMITH R. B. and SCHÄR, C., 1995. The effect of friction on shallow-water flow past an isolated obstacle. Journal of the Atmospheric Sciences, Vol. 52, pp. 1985-2005.

HAVEL, B. and MARTINUZZI, R.J., 1998. Turbulent flow around two interfering surface-mounted cubic obstacles. Proceedings of FEDSM'98, ASME Fluids Engineering Division Summer Meeting, June 21-25.

HO, C. M. and HUERRE, P., 1984. Perturbed free shear layers. Annu. Rev. Fluid Mech. Vol. 16, pp. 365-424.

HOYT, J. W. and SELLIN, R. H. J., 1995. A flow visualization study of separated flow over circular, elliptical and square cylinders. FED. Vol. 217, Separated and Complex Flows, ASME.

HUERRE, P. and MONKEWITZ, P. A. 1990. Local and Global Instabilities in Spatially Developing Flows", Ann. Rev. of Fluid Mech., Vol. 22, pp. 473-539.

INGRAM, R. G. and CHU, H. V., 1987. Flow around island in Rupert Bay: An investigation of the bottom friction effect. Journal of Geophysical Research , Vol. 92, No. C13, pp. 14521-14533.

JOHANSEN, J. B. and SMITH, C. R., 1983. The effects of cylindrical surface modification on turbulent boundary layers. Report FM-3, Department of Mechanical Engineering and Mechanics, Lehigh University, Bethlehem, PA.

KARATEKİN, O., WANG, F.Y. and CHARBONNIER, J., 1998. Near wake of a three dimensional bluff body at angle of attack. Proceedings of FEDSM'98: 1998 ASME Fluids Engineering Division Summer Meeting, June 21-25.

KEULEGAN, G. H., 1938. Laws of turbulent flow in open channels. J. Res., Nat. Bureau of Standards, Washington, D. C., Vol. 21, pp. 707-741.

KEANE, R. D., and ADRIAN, R. J., 1992. Theory of cross-correlation analysis of PIV images. Applied Scientific Research, Vol. 49, No.3, pp. 191-215.

KIRKGÖZ, M. S. and ARDIÇLIOĞLU, M. 1997. Velocity profiles of developing and developed open channel flow. Journal of Hydraulic Engineering, Vol. 123, pp. 1099-1105.

KLENANOFF, P. S., 1955. Characteristics of turbulence in a boundary layer with zero pressure gradient. NACA Technical Notes, No. 1347, Washington, D. C.

LIN, J. C., 1994. NFILVB, software, Fluid Mechanics Lab., Lehigh University Mechanical Engineering and Mechanics, Bethlehem, PA, USA.

LIN, J. C., YANG. Y. and ROCKWELL, D., 2001. Flow Past Two Cylinders in Tandem: Instantaneous and Averaged Flow Structure. submitted to the Journal of Fluids and Structures.

LLOYD, P. M. and STANSBY, P. K., 1997. Shallow-water flow around model conical island of small side slope. I: Surface piercing. Journal of Hydraulic Engineering, Vol. 123, pp. 1057-1067.

LOU, S. C. 1994. Effects of incidence and afterbody shape on flow past bluff cylinders. Journal of Wind Engineering and Industrial Aerodynamics, Vol. 53, pp. 375-399.

LOURENÇO, L. M. and KROTHAPALLI, A. 1996. Particle Image Velocimetry. Handbook of Fluid Dynamics and Fluid Machinery Vol. 1, Ed. Schetz J. and Fuhs A. E., John Wiley and Sons, Inc, New York, pp. 988-1002.

MITTAL, R. and BALACHANDAR, S. 1995. Effect of Three-Dimensionality on the Lift and Drag of the Nominally Two-Dimensional Cylinders. Physics of Fluids, Vol. 7, pp. 1841-1865.

NAUDASHER, E. and ROCKWELL, D. 1994. Flow-Induced Vibrations: An Engineering Guide. Balkema Press, Rotterdam.

NEZU, I. And RODI, W., 1986. Open channel flow measurements with a Laser Doppler Anemometer. Journal of Hydraulic Engineering, Vol. 112, pp. 335-355.

NEZU, I., TOMINAGA, A. and NAKAGAWA, H., 1993. Field measurements of secondary currents in straight rivers. Journal of Hydraulic Engineering, Vol. 119, pp. 598-614.

NEZU, I. and NAKAGAWA, H., 1993. Turbulence in open channel flow. IAHR Monograph Series, Balkema Press, The Netherlands.

PATTIARATCHI, C., JAMES, A. and COLLINS, M., 1986. Island wakes and headland eddies: A comprasion between remotely sensed data and laboratory experiments. Journal of Geophysical, Vol. 92, No. C1, pp. 783-784.

PERRY A. E. and CHONG M. S., 1986. A series-expansion study of the Navier-Stokes equations with applications to three-dimensional separation patterns. Journal of Fluid Mechanics, Vol. 173, pp. 207-223.

PERRY A. E. and STEINER, T. R., 1987. Large-scale vortex structures in turbulent wakes behind bluff bodies. Part I. Vortex formation processes. Journal of Fluid Mechanics, Vol. 174, pp. 233-270.

PRAISNER, T. J., SABATINO, D. R. and SMITH, C. R. 2000. Simultaneously Combined Liquid-Crystal Surface Heat Transfer and PIV Flow-Field Measurements. Experiments in Fluids, Vol. 30, No. 1, pp. 1-10.

PURTELL, L. P., KLEBANOFF, P. S. and BUCKLEY, F. T., 1981. Turbulent boundary layer at low Reynolds numbers. Physics of Fluids, Vol. 24, pp. 802-811.

RAFFEL, M., WILLERT, E.C., and KOMPENHANS, J., 1998. Particle image velocimetry. Springer-Verlag Berlin Heidelberg, New York.

ROCKWELL D., MAGNESS, C., TOWFIGHI, J., AKIN, O. and CORCORAN, T., 1993. High-Image-Density Particle Image Velocimetry using scanning techniques. Experiments in Fluids, Vol. 14, pp. 181-192.

ROSHKO, A., CARDELL, G. and LISOSKI, D., 1993. Interactions between the vortices and the free shear layer in bluff body wakes. Fourth ONR Workshop, Tempe, Arizona, USA, December 8-10.

SEAL, C. V. and SMITH, C. R., 1997. Intertwining laminar necklace vortices. Physics of Fluids Vol. 9, S9.

SEAL, C. V., SMITH C. R. and ROCKWELL, D. 1997 "Dynamics of the Vorticity Distribution in End-wall Junctions. AIAA Journal, Vol. 35, No. 6, pp. 1041-1047.

SEAL, C. V. and SMITH, C. R., 1999. Visualization of a mechanism for three-dimensional interaction and near-wall eruption. Journal of Fluid Mechanics, Vol. 394, pp. 193-203.

SCHÄR, C. and SMITH R. B., 1993. Shallow-water flow past isolated topography. Part II: Transition to Vortex Shedding. Journal of the Atmospheric Sciences, Vol. 50, pp. 1401-1412.

SCHLICHTING, H., 1968. Boundary layer theory. McGraw-Hill, Inc., New York.

SHERIDAN, J., LIN, J-. C. and ROCKWELL, D. 1997. Flow past a cylinder close to a free surface. Journal of Fluid Mechanics, Vol. 330, pp. 1-30.

SMITH, R. B. and GRUBIŠIĆ, V., 1993 "Aerial Observations of Hawaii's Wake", Journal of Atmospheric Sciences, Vol. 50, pp. 3728-3750.

SOFIALIDIS, D. and PRINOS, P., 1999. Numerical study of momentum exchange in compound open channel flow. Journal of Hydraulic Engineering, Vol. 125, No. 2.

STEFFLER, P. M., RAJARATNAM, N. and PETERSON, A. W., 985. LDA measurements in open channel. Journal of Hydraulic Engineering, Vol. 111, No. 1, pp. 119-130.

TACHIE, M. F. and BALACHANDAR, R., 2001. Shallow wakes generated on smooth and rough surfaces. Experiments in Fluids, Vol. 30, pp. 467-474.

TOWNSEND, A. A., 1956. The structure of turbulent shear flow. Cambridge University Press, New York.

TROII, K. and CHENG, Y. F., 1998. Flow transport phenomena over diamond-shaped cylinders. Proceedings of FEDSM'98: 1998 ASME Fluids Engineering Division Summer Meeting, June 21-25.

TSI Inc. Particle Image Velocimetry (PIV): Theory and Operation. Manual book.

TUKKER, J., 1997. Turbulence structures in shallow free-surface mixing layers. Ph. D. Thesis, Delft University, Laboratory of Fluid Mechanics.

UIJTEWALL, W. S. J. and TUKKER, J., 1998. Development of quasi two-dimensional structures in shallow free-surface mixing layer. Experiments in Fluids, Vol. 24, pp. 192-200.

UIJTEWALL, W. S. J. and BOOJI, R., 2000. Effects of shallowness on the development of free-surface mixing layers", Physics of Fluids, Vol. 12, No. 2, pp: 392-402.

ÜNAL, M. F. and ROCKWELL, D., 1988. On vortex formation from a cylinder. Part 1. The initial instability. Journal of Fluid Mechanics, Vol. 190, pp. 491-512.

VAN, D., 1982. An album of fluid motion. Parabolic Press.

WEI, T. and SMITH, C. R., 1986. Secondary vortices in the wake of circular cylinder. Journal of Fluid Mechanics, Vol. 169, pp. 513-533.

WESTEWEEL, J., 1997. Fundamentals of digital particle image velocimetry. Measurement Science Technology, Vol. 8, pp. 1379-1392.

WILLERT, C. E. and GHARIB, M., 1991. Digital particle image velocimetry. Experiments in Fluids, Vol. 10, pp. 181-193.

WILLIAMSON, C. H. K., 1996. Vortex dynamics on the cylinder wake. Annu. Rev. Fluid Mech. Vol. 28, pp. 477-539.

WOLANSKI, E., IMBERGER, I. and HERON, M. L., 1984. Island Wakes in shallow coastal waters. Journal of Geophysical Research, Vol. 89, No. C6, pp. 10553-10569.

APPENDIX

Vorticity Evaluation

General formula

$$\vec{\omega} = \nabla \times \vec{U} \tag{1}$$

Vorticity equation for two dimensional, incompressible, steady flow

$$\omega_z = \frac{\partial v}{\partial x} - \frac{\partial u}{\partial y} \tag{2}$$

Vorticity value in Equation (2) can be calculated by using one dimensional finite differences such as forward, backward or central or Stokes theorem equation used in NFILVB software reduces to a line integral of dot product between the local velocity $\vec{U}$ and the incremental path line element vector $d\vec{l}$.

Stokes Theorem,

$$\iint (\nabla \times \vec{U}) \cdot d\vec{A} = \oint \vec{U} d\vec{l} = \Gamma \tag{3}$$

Where $\vec{l}$ describes the path of integration around a surface A. Stokes theorem can also be applied to the (x,y) grided PIV velocity data

$$(\omega_z)_{i,j} = \frac{1}{A} \Gamma_{i,j} \tag{4}$$

where $(\omega_z)_{i,j}$ reflects the average vorticity within the enclosed area. In practice (4) is implemented by choosing a small rectangular contour two mesh points wide and two mesh points high around which circulation is calculated using a standard integration scheme such trapezoidal rule. The local circulation is then divided by the enclosed area to obtain at an average vorticity in this area. The following formula

provides a vorticity estimates at point (i,j) based on circulation estimate around the neighboring eight points for two dimensional, incompressible, steady flow assumption,

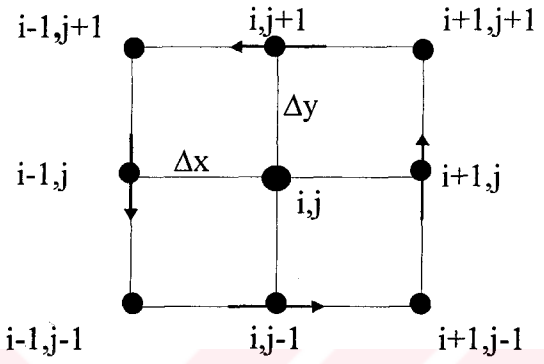

$$(\omega_z)_{i,j} = \frac{\Gamma_{i,j}}{4\Delta x \Delta y} \tag{5}$$

$$\Gamma_{i,j} = \frac{1}{2}\Delta x\left(u_{i-1,j-1} + 2u_{i,j-1} + u_{i+1,j-1}\right) + \frac{1}{2}\Delta y\left(v_{i+1,j-1} + 2v_{i+1,j} + v_{i+1,j+1}\right)$$
$$-\frac{1}{2}\Delta x\left(u_{i+1,j+1} + 2u_{i,j+1} + u_{i-1,j+1}\right) - \frac{1}{2}\Delta y\left(v_{i-1,j+1} + 2v_{i-1,j} + v_{i-1,j-1}\right) \tag{6}$$

CIRRICULUM VITAE

Ali Kahraman was born on January 10, 1972 in Konya, Turkey. In 1989, he graduated from High School, and enrolled at Selçuk University to study mechanical engineering. In 1993, he graduated with a Bachelor of Science degree in mechanical engineering from the Department of Mechanical Engineering. He began his graduate studies at the Department of Mechanical Engineering of Çukurova University. He obtained MSc degree from the same department in January 1997. He started the studies leading to degree of Ph.D in 1997 at the Department of Mechanical Engineering of Çukurova University. He worked as a Research Assistant at the Department of Mechanical Engineering of Dumlupınar University between 1993 and 1996. He worked as a Research Assistant at the Department of Mechanical Engineering of Çukurova University between 1996-2002. He worked as visiting researcher to carried out his part of Ph.D. thesis at the Department of Mechanical Engineering and Mechanics, Lehigh University, Bethlehem, Pennsylvania, USA. He has been working as a Research Assistant at the Department of Mechanical Education of Selçuk University since September 2002. He is married and has a son.